DRIVERS OF PHYTOPLANKTON DYNAMICS, AND CORRESPONDING IMPACTS ON BIOGEOCHEMISTRY, ALONG THE WEST ANTARCTIC PENINSULA

By

MICHAEL S. BROWN

A dissertation submitted to the

School of Graduate Studies

Rutgers, The State University of New Jersey

In partial fulfillment of the requirements

For the degree of

Doctor of Philosophy

Graduate Program in Oceanography

Written under the direction of

Oscar M. Scofield

And approved by

_____

_____

_____

_____

New Brunswick, New Jersey

October, 2020

ABSTRACT OF THE DISSERTATION

Drivers of phytoplankton dynamics, and corresponding impacts on biogeochemistry, along the West Antarctic Peninsula

By MICHAEL S. BROWN

Dissertation Director:

Oscar M. Schofield

The West Antarctic Peninsula (WAP) has experienced rapid warming and melting since the mid-20th century. While there is evidence that these environmental drivers are altering the WAP marine food web, there is uncertainty regarding the mechanisms of these changes, and how they will impact the regional carbon cycle. In this dissertation, I examine the drivers of variability in phytoplankton dynamics along the WAP, with a primary focus on diatoms and cryptophytes (the two major phytoplankton groups), and how this variability impacts regional biogeochemistry.

In Chapter 2 (*Enhanced oceanic CO_2 uptake along the rapidly changing West Antarctic Peninsula*), I use a 25-year dataset to examine the coupling between upper ocean stability, phytoplankton dynamics, and oceanic CO_2 uptake along the WAP. I demonstrate that greater upper ocean stability drives increased phytoplankton biomass, resulting in greater oceanic CO_2 uptake. Diatom assemblages achieve higher biomass and oceanic CO_2 uptake than cryptophyte assemblages. Over the past 25 years, in response to changes in sea ice dynamics, there have been significant positive trends in upper ocean stability, phytoplankton biomass, and oceanic CO_2 uptake along the WAP.

In Chapter 3 (*Low diversity of a key phytoplankton group along the West Antarctic Peninsula*), I use a phylogenetic placement approach with a 5-year dataset of DNA sequences to characterize WAP cryptophyte diversity and its drivers to a high taxonomic resolution. I demonstrate that there are just two major WAP cryptophyte taxa that consistently comprise nearly 100% of the cryptophyte community. Variability in the proportion of these two taxa is associated with changes in oceanographic conditions, including temperature, salinity, nutrients, and phytoplankton dynamics. These variables are all predicted to be altered with continued environmental change along the WAP.

In Chapter 4 (*Meltwater chemistry of a receding West Antarctic Peninsula glacier*), I characterize the chemical composition and discharge dynamics of two WAP glacial meltwater streams. While different in their physical characteristics, I demonstrate that both streams have a similar composition of stable oxygen isotopes of water, which is important for determining regional oceanic freshwater budgets. Additionally, relative to coastal seawater, both streams have high concentrations of trace metals (including iron and copper), and low concentrations of silicate. These high glacial meltwater trace metal concentrations could be important for structuring coastal phytoplankton communities along the WAP.

Acknowledgements

I would like to thank my committee members: Oscar Schofield, Rob Sherrell, Kay Bidle, and Adrian Marchetti. Oscar, thank you for your mentorship, support, and endless enthusiasm. Rob, thank you for your dedication to our trace metals work. Kay, thank you for the personalized genomics primer. Adrian, thank you for all your helpful advice.

I would also like to thank my coauthors for their contributions. Chapter 2: David Munro, Colette Feehan, Colm Sweeney, and Hugh Ducklow; Chapter 3: Jeff Bowman, Yajuan Lin, Colette Feehan, and Nicolas Cassar; and Chapter 4: Colette Feehan, Kaixuan Bu, Vincent Roccanova, Michael Meredith, and Åsa K. Rennermalm.

Much of this work is indebted to the many previous and current members of the Palmer LTER and support crew. Thank you for your dedication in the field and lab. Geospatial support for this work was provided by the Polar Geospatial Center under NSF-OPP awards 1043681 and 1559691.

I would like to thank Rutgers University for the GA/TA funding. Thank you as well to EOAS and the GPO for the academic support and additional financial assistance.

Chapter 2 (*Enhanced oceanic CO_2 uptake along the rapidly changing West Antarctic Peninsula*) exists as a publication in *Nature Climate Change* (Brown et al. 2019).

Thank you for the inspiration: Thomas Earl Petty, Louie Louie, and Green Onions. Bernie Sanders. Thank you Non-Existent, The Blue Lemons, and The Brothers Blue. I'm looking forward to getting back to it.

This work is for all of my friends and family. Mom and Kate, thank you for your endless love and support. Dad, I miss you every day. With all my love for Colette and Thomas.

Table of contents

Abstract of the dissertation ii

Acknowledgements iv

List of tables x

List of figures xi

1. Introduction 1

2. Enhanced oceanic CO_2 uptake along the rapidly changing West Antarctic Peninsula 6

2.1 Abstract 6

2.2 Main text 7

2.3 Figures 17

2.4 Methods 21

2.4.1 Palmer LTER 21

2.4.2 Water column physics and stability 21

2.4.3 Water column discrete sampling 23

2.4.4 Observation and estimation of $pCO_{2,sur}$ and ΔpCO_2 26

2.4.5 Modelling of ΔpCO_2 28

2.4.6 Drivers of $pCO_{2,sur}$ 29

2.4.7 Statistics 29

2.5 Supplementary tables 32

2.6 Supplementary figures 34

3. Low diversity of a key phytoplankton group along the West Antarctic Peninsula 42

3.1 Abstract 42

3.2 Introduction 43

3.3 Methods 46

3.3.1 Palmer LTER core measurements 46

3.3.2 DNA samples 48

3.3.3 Phylogenetic placement 49

3.3.4 Seascape units 50

3.4 Results 51

3.4.1 Oceanographic context 51

3.4.2 Cryptophyte ASVs and taxa 52

3.4.3 Drivers of cryptophyte diversity 53

3.5 Discussion 54

3.6 Figures 59

3.7 Supplementary tables 64

4. Meltwater chemistry of a receding West Antarctic Peninsula glacier 67

4.1 Abstract 67

4.2 Introduction 68

4.3 Methods 70

4.3.1 Sampling sites 70

4.3.2 Sampling procedures....71
4.3.3 Trace metals....73
4.3.4 Macronutrients....74
4.3.5 Oxygen isotopes....74
4.3.6 Continuous stream discharge....74
4.4 Results....77
4.4.1 Stream discharge....77
4.4.2 Oxygen isotopes....78
4.4.3 Trace metals and macronutrients....78
4.5 Discussion....80
4.5.1 Stream variability....80
4.5.2 Chemistry commonalities....81
4.5.3 Coastal seawater impacts....83
4.5.4 Global context....85
4.6 Conclusions....86
4.7 Tables....88
4.8 Figures....92
4.9 Supplementary tables....101
4.10 Supplementary figures....109
5. Conclusions....110
6. References....115
7. Appendix A: Glacial meltwater microcosm experiment....124
7.1 Motivation....124

7.2 Completed methods 124
7.3 Preliminary results 127
7.4 Concluding remarks 128
7.5 Figures.....130

List of tables

Supplementary Table 2.1	WAP time series trends	32
Supplementary Table 2.2	WAP time series averages	33
Supplementary Table 3.1	Cryptophyte ASVs and taxa summary	64
Table 4.1	Summary of sampling events	88
Table 4.2	Stream 1 glacial meltwater	89
Table 4.3	Stream 2 glacial meltwater	89
Table 4.4	Stream 1 coastal seawater	90
Table 4.5	Stream 2 coastal seawater	90
Table 4.6	Stream 1 and 2 additional sampling events	91
Supplementary Table 4.1	Stream 1 and 2 GPS way points	101
Supplementary Table 4.2	Coastal seawater data	102
Supplementary Table 4.3	Glacial meltwater data	104
Supplementary Table 4.4	Glacial meltwater data (additional)	106
Supplementary Table 4.5	Station B and E data	108

List of figures

Figure 2.1 Map of the study area....17

Figure 2.2 ΔpCO_2 and chl-*a* relationship....18

Figure 2.3 ΔpCO_2, chl-*a*, MLD, and assemblage relationship....19

Figure 2.4 Time series of MLD, chl-*a*, and ΔpCO_2....20

Supplementary Figure 2.1 MLD climatology....34

Supplementary Figure 2.2 Assemblage locations....35

Supplementary Figure 2.3 Differences in assemblage chl-*a* and ΔpCO_2....36

Supplementary Figure 2.4 Differences in assemblage physical properties....37

Supplementary Figure 2.5 Differences in assemblage chemical properties....38

Supplementary Figure 2.6 Driver analysis for $pCO_{2,sur}$....39

Supplementary Figure 2.7 Matchup analysis for $pCO_{2,sur}$....41

Figure 3.1 Map of the study area....59

Figure 3.2 Seascape units – all samples....60

Figure 3.3 Cryptophyte taxa % vs. sample #....61

Figure 3.4 Cryptophyte taxa % vs. cryptophyte %....61

Figure 3.5 Seascape units – cryptophyte groups....62

Figure 3.6 Cryptophyte groups pigment ratios....63

Figure 4.1 Map of the study area....92

Figure 4.2 Streams discrete discharge....93

Figure 4.3 Stream 2 continuous discharge....94

Figure 4.4 Streams diurnal discharge cycle.....95

Figure 4.5 Streams glacial meltwater and glacial ice $\delta^{18}O$ 96

Figure 4.6 Streams glacial meltwater coastal seawater elements.....97

Figure 4.7 Streams glacial meltwater elements time series.....98

Figure 4.8 Streams coastal seawater elements time series 99

Figure 4.9 Streams glacial meltwater and discharge correlations 100

Supplementary Figure 4.1 Stream 2 height and discharge regression.....109

Figure 7.1 Meltwater microcosm experimental design 130

Figure 7.2 Meltwater microcosm experimental setup 131

Figure 7.3 Meltwater microcosm experiment chl-*a* 131

Figure 7.4 Meltwater microcosm experiment macronutrients 132

1 Introduction

The West Antarctic Peninsula (WAP) marine ecosystem spans 1300 km roughly north-south from King George Island (62°S) to the Bellingshausen Sea (70°S), and extends 200 km roughly east-west from the coast to the continental slope (Ducklow et al. 2013). This region is experiencing rapid environmental change (Schofield et al. 2010). In particular, over the past 50 years, winter surface atmospheric temperatures have increased in the WAP by 6°C, five times the global average (Vaughn et al. 2003, Turner et al. 2014). The ocean in this region has also warmed, with a 1°C increase in surface ocean temperature (Meredith and King 2005), as well as substantial warming of the deeper ocean (Martinson et al. 2008). Additionally, many of the region's glaciers are in retreat (Cook et al. 2016). Furthermore, there has been a decline in the WAP annual mean sea ice extent as a result of a ~90 day decrease in winter sea ice duration, due to an earlier advance and later retreat of sea ice (Stammerjohn et al. 2008a,b). In the northern WAP, perennial sea ice no longer exists (Ducklow et al. 2013).

These environmental changes are associated with alterations in regional atmospheric and oceanic circulation patterns, and are amplified by positive feedback loops. In the Southern Hemisphere, the two climate modes that dominate atmospheric variability are the Southern Annular Mode (SAM) and El Niño-Southern Oscillation (ENSO) (Stammerjohn et al. 2008b). During a positive-phase SAM (i.e. +SAM), low and high atmospheric pressure anomalies are observed over Antarctica and the mid-latitudes, respectively (Marshall 2003), with the opposite scenario observed during a negative-

phase SAM (i.e. -SAM). Additionally, during +SAM, the mid-latitude jet stream strengthens and moves toward the pole (Thompson et al. 2011), intensifying the surface westerlies at ~55°S (Hall and Visbeck 2002), and the Amundsen Sea Low (ASL) deepens, bringing warm, northerly winds across the WAP (Maksym et al. 2012). A dominant feature of the high-latitude ENSO teleconnection is the strengthening of the polar front jet, formation of the ASL, and more storms and warmer conditions on the WAP during La Niña, with the opposite scenario observed during El Niño (Yuan 2004). Finally, the impacts of SAM can be compounded by those of ENSO. For example, during a coincident +SAM/La Niña, the ASL is at its deepest, and strong, warm, northerly winds blow across the WAP (Maksym et al. 2012).

Over the past few decades, SAM has been trending positive (Marshall 2003), which has contributed to the increased atmospheric temperatures in the WAP (Thompson and Solomon 2002). Additionally, this trend in +SAM, combined with an increase in co-variability between SAM and ENSO (e.g. coincident +SAM and La Niña) (Fogt and Bromwich, 2006) has driven the decrease in WAP winter sea ice duration, as the strong, warm, northerly winds result in a later (earlier) sea ice advance (retreat), respectively (Stammerjohn et al. 2008a,b). Furthermore, these increased winds and associated storms alter regional ocean circulation by mixing and upwelling more relatively warm (4°C) Upper Circumpolar Deep Water (UCDW) onto the WAP continental shelf (Martinson 2012). These atmosphere-ocean-ice effects are amplified by positive feedback loops (Schofield et al. 2010).

The Palmer Long-Term Ecological Research program (LTER) began in the early 1990s, with the underlying hypothesis that sea ice dynamics structure the WAP marine

ecosystem (Ducklow et al. 2007). Concurrent with the environmental changes discussed above have been substantial alterations to the WAP marine food web, from primary producers to apex predators. Specifically, it has been observed that the average chlorophyll-*a* concentration in the region has decreased (Montes-Hugo et al. 2009). This change has not been uniform across the WAP, with the decrease in phytoplankton biomass, as well as a shift to smaller cells, occurring primarily in the north, and associated with a decrease in sea ice and increase in clouds, wind speed, and mixed-layer depth. In the south, phytoplankton biomass has actually increased, associated with a decrease in sea ice that has alleviated light limitation (Montes-Hugo et al. 2009). Regarding primary consumers, there is evidence for a decline in Antarctic krill over the past few decades (Loeb et al. 1997, Atkinson et al. 2004). Krill are dependent on sea ice for their reproduction and recruitment, and thus it has been hypothesized that the decline in krill may be due to the decline in sea ice duration (Loeb et al. 1997, Ducklow et al. 2013). Perhaps the most striking change to the WAP marine ecosystem has been the shift observed in penguin composition, as ice-dependent Adélie populations have decreased by 90%, while ice-intolerant Chinstrap and Gentoo populations have increased (Ducklow et al. 2007).

The classic view of the WAP marine ecosystem is that it consists of a short food chain, with larger (> 20 μm, i.e. microplankton) diatoms supporting krill, which are then consumed by apex predators such as penguins and whales (Hart 1942). However, it has also become recognized that smaller nanoplankton (< 20 μm) and picoplankton (< 2 μm) contribute substantially to phytoplankton communities, with cryptophytes being the most dominant nanoplankton. Together, diatoms and cryptophytes are the two major

phytoplankton groups along the WAP (Ducklow et al. 2007, and references therein). At Palmer Station, the typical phytoplankton seasonal progression consists of a spring diatom bloom transitioning to an increased proportion of cryptophytes (Moline and Prezelin 1996, Moline et al. 2004, Schofield et al. 2017). Additionally, a 4 to 6 year peak in summer phytoplankton biomass has been observed at Palmer Station, with anomalously high years dominated by diatoms, and low years characterized by a higher proportion of cryptophytes (Saba et al. 2014). Finally, it has also been observed that cryptophytes along the WAP can be associated with lower salinities, driven by the input of glacial meltwater (Moline and Prezelin 1996, Moline et al. 2004, Mendes et al. 2013, Schofield et al. 2017).

While there is evidence that the rapid environmental change along the WAP has impacted the regional marine food web, in particular primary producers, uncertainty remains regarding the mechanisms of change. For example, one hypothesis to explain the association between cryptophytes and lower salinities is that there is a glacial meltwater constituent that favors them (Schofield et al. 2017). However, little is known about the chemical composition of glacial meltwater along the WAP (Hodson et al. 2010). Regardless of the driver, given predictions of continued warming and melting, it has been hypothesized that cryptophytes will increase in abundance along the WAP (Moline and Prezelin 1996, Moline et al. 2004, Schofield et al. 2017). This shift in phytoplankton composition would represent a change in the size distribution from larger to smaller cells, which could have profound impacts on the WAP marine food web, as krill are unable to efficiently graze cryptophytes given their small size (Haberman et al. 2003). This shift could also impact regional biogeochemistry, including oceanic CO_2 uptake. The WAP is

a productive region of the Southern Ocean, which plays a large role in the global carbon cycle (Takahashi et al. 2012). However, it is not clear how the Southern Ocean CO_2 sink will respond to continued environmental change (McKinley et al. 2017, Gruber et al. 2019). Complicating matters is the fact that relative to diatoms, little is known about the diversity and ecology of WAP cryptophytes (Schofield et al. 2017).

The focus of this dissertation is to identify drivers of changes in phytoplankton dynamics (abundance and community composition) along the WAP, especially between diatoms and cryptophytes, and to assess the impacts of these changes on regional biogeochemistry. The structure of the dissertation is as follows: In Chapter 2 (*Enhanced oceanic CO_2 uptake along the rapidly changing West Antarctic Peninsula*), I use a 25-year dataset to determine the relationship between upper ocean stability, phytoplankton dynamics, and oceanic CO_2 uptake along the WAP, and assess the presence of long-term trends in these variables. In Chapter 3 (*Low diversity of a key phytoplankton group along the West Antarctic Peninsula*), I use a phylogenetic placement approach with a 5-year dataset of DNA sequences to assess the diversity of WAP cryptophytes to a high taxonomic resolution, and determine the physicochemical drivers of their diversity. In Chapter 4 (*Meltwater chemistry of a receding West Antarctic Peninsula glacier*), I characterize the chemical composition (trace metals, macronutrients, and stable oxygen isotopes in water) and discharge dynamics of two WAP glacial meltwater streams. Finally, in Chapter 5 (*Conclusions*) I summarize the main findings of the dissertation and discuss potential future related work.

2 Enhanced oceanic CO_2 uptake along the rapidly changing West Antarctic Peninsula

2.1 Abstract

The global ocean is an important sink for anthropogenic CO_2 (Sabine et al. 2004). Nearly half of the oceanic CO_2 uptake occurs in the Southern Ocean (Takahashi et al. 2012). Although the role of the Southern Ocean CO_2 sink in the global carbon cycle is recognized, there are uncertainties regarding its contemporary trend (McKinley et al. 2017, Gruber et al. 2019), with a need for improved mechanistic understanding, especially in productive Antarctic coastal regions experiencing substantial changes in temperature and sea ice (Schofield et al. 2010). Here, we demonstrate strong coupling between summer upper ocean stability, phytoplankton dynamics, and oceanic CO_2 uptake along the rapidly changing West Antarctic Peninsula (WAP) using a 25-year dataset (1993 to 2017). Greater upper ocean stability drives enhanced biological production and biological dissolved inorganic carbon (DIC) drawdown, resulting in greater oceanic CO_2 uptake. Diatoms achieve higher biomass, oceanic CO_2 uptake, and uptake efficiency than other phytoplankton. Over the past quarter-century, changes in sea ice dynamics have driven an increase in upper ocean stability, phytoplankton biomass, and biological DIC drawdown, resulting in nearly a 5-fold increase in summer oceanic CO_2 uptake. We hypothesize that continued warming and declines in sea ice will lead to a decrease in biological DIC drawdown, negatively impacting summer oceanic CO_2 uptake. These

results from the WAP provide a framework to understand how oceanic CO_2 uptake in other Antarctic coastal regions may be altered due to climate change.

2.2 Main text

The global ocean is an important CO_2 sink given its ability to absorb and sequester atmospheric CO_2. The air-sea CO_2 flux is proportional to the difference between the partial pressure of CO_2 in the surface ocean ($pCO_{2,sur}$) and atmosphere ($pCO_{2,atm}$), i.e. ΔpCO_2, where a negative (positive) ΔpCO_2 indicates a flux of CO_2 to the ocean (atmosphere) (Takahashi et al. 2002). Typically, $pCO_{2,sur}$ is more variable than $pCO_{2,atm}$, and thus ΔpCO_2 is primarily controlled by $pCO_{2,sur}$ (Takahashi et al. 2002). Variability in $pCO_{2,sur}$ is controlled by temperature, salinity, DIC, and total alkalinity (TA), with DIC and TA impacted by biological production, anthropogenic CO_2, mixing, and circulation (McKinley et al. 2017). The air-sea CO_2 flux is also dependent on the air-sea CO_2 transfer velocity, which is parameterized with wind speed (Takahashi et al. 2002). Given that over our study period there is no long-term trend in wind speed during summer along the WAP (Schofield et al. 2018), and due to uncertainty in both wind speed estimates and the transfer velocity parameterization, here we use ΔpCO_2 to assess variability in oceanic CO_2 uptake, consistent with previous studies (Fay et al. 2014, Lovenduski et al. 2015, Munro et al. 2015).

The WAP marine ecosystem (Figure 2.1) is undergoing substantial physical changes (Schofield et al. 2010). Atmospheric temperatures are rapidly warming, including a 7 ºC increase in winter surface temperatures since 1950 (5x the global average) (Turner et al. 2014). Additionally, there have been long-term increases in

oceanic temperatures (Martinson et al. 2008, Meredith and King 2005), a majority of marine glaciers are in retreat (Cook et al. 2005), and since 1979 the sea ice season has shortened by 3 months (Stammerjohn et al. 2008a). These changes are associated with strengthening winds over the Southern Ocean (Thompson and Solomon 2002), driven by large-scale climate variability, including a positive trend in the Southern Annular Mode (SAM) (Marshall 2003), and co-variability between SAM and the El Niño-Southern Oscillation (Stammerjohn et al. 2008b). Due to the north-south orientation of the WAP, there are meridional differences in warming, glacial retreat, and sea ice decline (Ducklow et al. 2013). Along the northern WAP, maritime conditions have progressed southward, where warming and strong winds have led to a substantial long-term decrease in sea ice, resulting in decreased upper ocean stability (Montes-Hugo et al. 2009). Polar conditions persist along the mid/southern WAP (our focus here), although warming and wind-driven advection has led to increased inter-annual variability and a smaller long-term decrease in sea ice (Stammerjohn et al. 2008a, Meredith et al. 2017, Schofield et al. 2018). Given that Antarctic marine organisms are dependent on sea ice dynamics, these physical changes along the WAP have resulted in alterations to the marine food web across all trophic levels (Schofield et al. 2010).

The WAP marine ecosystem is highly productive and characterized by large coastal phytoplankton blooms during spring and summer (Ducklow et al. 2013). Given that macronutrients are abundant (Kim et al. 2016), it has been hypothesized that biological production along the WAP is primarily controlled by light availability, which is a function of upper ocean stability (Vernet et al. 2008, Saba et al. 2014, Carvalho et al. 2016, Schofield et al. 2018). However, micronutrients like iron may be limiting on the

shelf and slope (Annett et al. 2017, Sherrell et al. 2018). It has also been demonstrated that biological production can drive variability in oceanic CO_2 uptake along the WAP (Carrillo et al. 2004, Tortell et al. 2014, Hauri et al. 2015, Eveleth et al. 2017, Legge et al. 2017, Ito et al. 2018). These previous studies have been limited in spatial-temporal extent, and/or with minimal focus on the role of phytoplankton community composition. Here, we investigate the coupling between upper ocean stability, phytoplankton dynamics (biomass and composition), and oceanic CO_2 uptake during summer along the mid/southern WAP for a quarter-century (1993 to 2017), using data collected by the Palmer Long-Term Ecological Research (LTER) and Drake Passage Time-Series (DPT) programs.

An inverse relationship between chlorophyll-*a* (chl-*a*) and ΔpCO_2 indicates the critical role of biological production in driving oceanic CO_2 uptake. Surface averages of chl-*a* via fluorescence and ΔpCO_2 were calculated at the Palmer LTER regional sampling grid stations (Figure 2.1b; 2.4: Methods). In general, ΔpCO_2 is negative (Figure 2.2a). There is a significant negative correlation between chl-*a* and ΔpCO_2 (Spearman's rho, r_s = -0.62, $p < 0.001$; Figure 2.2a). Climatological chl-*a* (ΔpCO_2) shows a cross-shore gradient, with higher (lower) values towards the coast (Figure 2.2b-c). There is a significant negative correlation between yearly sub-regional (slope, shelf, and coast sub-regions) chl-*a* and ΔpCO_2 (r_s = -0.53, p = 0.008; r_s = -0.60, p = 0.002; r_s = -0.64, $p <$ 0.001, respectively; Figure 2.2d). Summer surface warming (freshening) can also increase (decrease) ΔpCO_2, although these effects typically offset each other, and cannot account for the large variability observed in ΔpCO_2 (Figure 2.2a) (Eveleth et al. 2017). These results demonstrate that during summer along the mid/southern WAP, the region is

a strong sink for CO_2, and biological production is a primary driver of oceanic CO_2 uptake.

To assess the extent that upper ocean stability is a primary control on biological production, mixed-layer depth (MLD) was determined from CTD (conductivity-temperature-depth instrument) casts and surface averages of chl-*a* via high-performance liquid chromatography (HPLC) were calculated at the Palmer LTER regional sampling grid stations (Figure 2.1b; 2.4: Methods). Along the WAP, MLD is controlled by wind, sea ice, and meltwater dynamics, which are driven by large-scale climate variability. During -SAM/El Niño conditions, cold and weak southerly winds blow across the region, resulting in high sea ice concentrations that reduce wind-mixing in winter and supply meltwater in spring/summer, which along with glacial meltwater, stabilizes the upper ocean, supporting large phytoplankton blooms (Stammerjohn et al. 2008a,b, Vernet at al. 2008, Montes-Hugo et al. 2009, Ducklow et al. 2013, Saba et al. 2014, Carvalho et al. 2016, Meredith et al. 2017, Schofield et al. 2018). The opposite occurs during +SAM/La Niña conditions. Climatological MLD shows a meridional and cross-shore gradient, with deeper MLDs further north and offshore (Supplementary Figure 2.1). Higher chl-*a* concentrations are primarily associated with shallower MLDs (Figure 2.3), where phytoplankton cells are retained in the upper ocean, reducing light limitation. This supports the hypothesis that during summer along the mid/southern WAP, upper ocean stability is a primary control on biological production. Lower ΔpCO_2 values are primarily associated with higher chl-*a* concentrations at shallower MLDs (Figure 2.3). The positive monotonic relationship between ΔpCO_2 and MLD (Figure 2.3) demonstrates that MLD can also drive variability in ΔpCO_2 independent of biological production. Modeling

ΔpCO_2 as a function of MLD with constant biological production (2.4: Methods) indicates that shallower MLDs drive lower ΔpCO_2 values due to higher biological volumetric DIC drawdown (Figure 2.3). These results demonstrate that during summer along the mid/southern WAP, there is strong coupling between upper ocean physics and biogeochemistry, where greater upper ocean stability drives enhanced biological DIC drawdown (through both enhanced biological production and biological volumetric DIC drawdown), resulting in greater oceanic CO_2 uptake.

The importance of phytoplankton community composition, determined with CHEMTAX using accessory pigments via HPLC (2.4: Methods), on phytoplankton biomass and oceanic CO_2 uptake was also assessed. The primary regional phytoplankton groups are diatoms (typically large: > 20 μm) and cryptophytes (small: < 20 μm), although small dinoflagellates and unidentified phytoflagellates (i.e. "mixed flagellates") can also contribute substantially to phytoplankton biomass (Schofield et al. 2017). At shallower MLDs, communities dominated (i.e. ≥ 50% of total chl-*a*) by diatoms (cryptophytes) are associated with lower (higher) ΔpCO_2 values (Figure 2.3). Communities dominated by mixed flagellates occur primarily at deeper MLDs, and are associated with higher ΔpCO_2 values (Figure 2.3). To examine differences in water mass properties (phytoplankton biomass, oceanic CO_2 uptake, etc.) between diatom, cryptophyte, and mixed flagellate assemblages (i.e. ≥ 75% of total chl-*a*; Supplementary Figure 2.2), Kruskal-Wallis tests were performed (2.4: Methods). Diatoms, relative to cryptophytes, relative to mixed flagellates, achieve a significantly higher (lower) chl-*a* (ΔpCO_2) (Supplementary Figure 2.3). Diatoms and cryptophytes occur at a similarly shallow MLD relative to mixed flagellates (Supplementary Figure 2.4a). This allows for a

direct comparison of the biogeochemical response of just diatoms and cryptophytes, since MLD influences biological volumetric DIC drawdown independent of biological production (Figure 2.3). Diatoms occur in waters that are significantly lower in temperature than cryptophytes, but similar in salinity (Supplementary Figure 2.4b-c). However, the resulting ΔpCO_2 difference of 5 μatm due to temperature (Takahashi et al. 2002) cannot account for the lower ΔpCO_2 relative to cryptophytes. Diatoms also achieve a significantly lower salinity-normalized DIC, nitrate, and phosphate than cryptophytes (Supplementary Figure 2.5a-c). These results demonstrate that during summer along the mid/southern WAP, diatoms achieve significantly higher biomass, oceanic CO_2 uptake, and uptake efficiency than cryptophytes. The higher uptake efficiency of diatoms could be due to their larger size, greater predation by krill (Haberman et al. 2003), cryptophyte mixotrophy (Stoecker et al. 2017), and/or differences in micronutrient limitation, nutrient uptake ratios, or growth rates.

Temporal trends during summer along the mid/southern WAP in regional and sub-regional (north and south sub-regions; Figure 2.1b) upper ocean stability, phytoplankton dynamics, and oceanic CO_2 uptake were determined with time series of MLD, chl-*a*, phytoplankton group chl-*a*, and ΔpCO_2 (2.4: Methods; Supplementary Table 2.1). From 1993 to 2017, there was a significant decrease in regional MLD (-1.3 m yr^{-1}, $p < 0.001$; Figure 2.4a). This decrease in MLD is associated with a wind-driven increase since 2008 in sea ice (Stammerjohn et al. 2008a, Meredith et al. 2017, Schofield et al. 2018), and declines since 1993 in upper ocean temperature, salinity, and density due to continued sea ice melt, with minimal impact from variability in wind-driven mixing (Schofield et al. 2018). There was also a significant increase in regional chl-*a* via

fluorescence (+0.015 log10[mg m^{-3}] yr^{-1}, p = 0.049; Figure 2.4b) and HPLC (Supplementary Table 2.1). This increase in regional chl-*a* is consistent with the satellite observations of Montes-Hugo et al. (2009), who reported a long-term increase (decrease) in chl-*a* along the mid/southern (northern) WAP. Additionally, sub-regional phytoplankton group chl-*a* trends indicate a large significant increase in diatoms relative to cryptophytes in the south sub-region, and a large significant increase in cryptophytes relative to diatoms in the north sub-region (Supplementary Table 2.1). This meridional variability in sub-regional diatom and cryptophyte trends is also consistent with the satellite observations of Montes-Hugo et al. (2009), who reported a long-term increase (decrease) in diatom proportion along the mid/southern (northern) WAP. The significant regional increase in cryptophytes (Supplementary Table 2.1) also supports the hypothesis that this group will increase in abundance with continued meltwater inputs (Moline et al. 2004, Schofield et al. 2017).

Consistent with the changes in regional MLD and chl-*a* (Figure 2.4a-b), there was a significant decrease in regional ΔpCO_2 (-2.6 µatm yr^{-1}, p = 0.016; Figure 2.4c), representing nearly a 5-fold increase in oceanic CO_2 uptake. Although this ΔpCO_2 trend is similar in magnitude to the atmospheric CO_2 trend (1.9 ppm yr^{-1} at 65°S; Supplementary Figure 2.6), an analysis of the $pCO_{2,sur}$ trend drivers (2.4: Methods; Supplementary Table 2.1-2.2) demonstrates that the decrease in regional ΔpCO_2 is due to offsetting effects on $pCO_{2,sur}$ from an increase in biological DIC drawdown and anthropogenic DIC (Supplementary Fig. 2.6). Furthermore, sub-regional trends indicate that the changes in regional MLD, chl-*a*, and ΔpCO_2 are primarily driven by changes in the south sub-region (Supplementary Table 2.1). Here, the effect on $pCO_{2,sur}$ from a large

increase in biological DIC drawdown is more than twice that of an increase in anthropogenic DIC (Supplementary Fig. 2.6), resulting in a large significant decrease in ΔpCO_2 (-4.6 µatm yr^{-1}, $p = 0.005$; Supplementary Table 2.1), which is more than twice the magnitude of the atmospheric CO_2 trend. The increases in regional and sub-regional biological DIC drawdown are consistent with the increases in chl-*a* (Figure 2.4b; Supplementary Table 2.1), underscoring the critical role of phytoplankton in driving ΔpCO_2. These results demonstrate that from 1993 to 2017 during summer along the mid/southern WAP, changes in sea ice dynamics drove an increase in upper ocean stability, which drove an increase in phytoplankton biomass and biological DIC drawdown, resulting in greater oceanic CO_2 uptake.

The increase in regional phytoplankton biomass (Figure 2.4b) raises the possibility that micronutrients like iron could eventually limit biological production and oceanic CO_2 uptake during summer along the mid/southern WAP. Surface iron shows a cross-shore gradient, with higher concentrations towards the coast, and is supplied by remnant winter water in combination with sea ice melt on the slope and outer shelf, and with meteoric (glacial meltwater and precipitation), sub-glacial, and sedimentary sources towards the coast (Annett et al. 2017, Schofield et al. 2018). It is predicted that SAM will remain positive, with strong winds persisting and temperatures continuing to increase along the WAP, resulting in further glacial retreat and sea ice decline (Turner et al. 2014). In the short-term, it is possible that surface iron could increase under these conditions (Annett et al. 2017), allowing a continued increase in phytoplankton biomass. However, even with no change in biological production, a continued increase in upper ocean

stability could drive a continued increase in oceanic CO_2 uptake through enhanced biological volumetric DIC drawdown (Figure 2.3).

In the long-term, it has been demonstrated that the effects of climate change are progressing southward along the WAP, given the substantial declines in sea ice, upper ocean stability, phytoplankton biomass, and diatom proportion along the northern WAP (Montes-Hugo et al. 2009). Our results demonstrate the progression of these changes into the mid/southern WAP, and their impact on upper ocean physics and biogeochemistry. Here, there have been smaller (larger) increases in upper ocean stability, phytoplankton biomass, and oceanic CO_2 uptake in the north (south) sub-region (Supplementary Table 2.1). The meridional variability in these changes in phytoplankton biomass and oceanic CO_2 uptake are associated with shifts in phytoplankton community composition, as there has been a relatively larger increase in cryptophytes (diatoms) in the north (south) sub-region (Supplementary Table 2.1). In this study, we demonstrate strong coupling between upper ocean physics and biogeochemistry during summer along the mid/southern WAP (Figure 2.2-2.4). As sea ice further declines to critical levels here, a decrease in upper ocean stability could drive a decrease in phytoplankton biomass and biological DIC drawdown, negatively impacting oceanic CO_2 uptake during summer. This could be compounded by a further shift from diatoms to cryptophytes. A decline in sea ice could also lead to a diminished "rectification" of the seasonal CO_2 air-sea flux cycle (Yager et al. 1995), resulting in enhanced outgassing during other seasons, although the ultimate impact of increased air-sea exchange and continued rising atmospheric CO_2 concentrations on net annual oceanic CO_2 uptake is uncertain (Sweeney 2003). Our analysis is possible due to the sustained and consistent spatial-temporal sampling of

coincident physical and biogeochemical oceanographic variables during summer along the mid/southern WAP by the Palmer LTER and DPT programs, which should be expanded to other seasons, and elsewhere around Antarctica. In the coming decades, it is predicted that sea ice will decline around much of the continent (Turner et al. 2014). Therefore, despite a recent increase, the future of the WAP, and other Antarctic coastal regions, may be as a reduced sink for atmospheric CO_2.

2.3 Figures

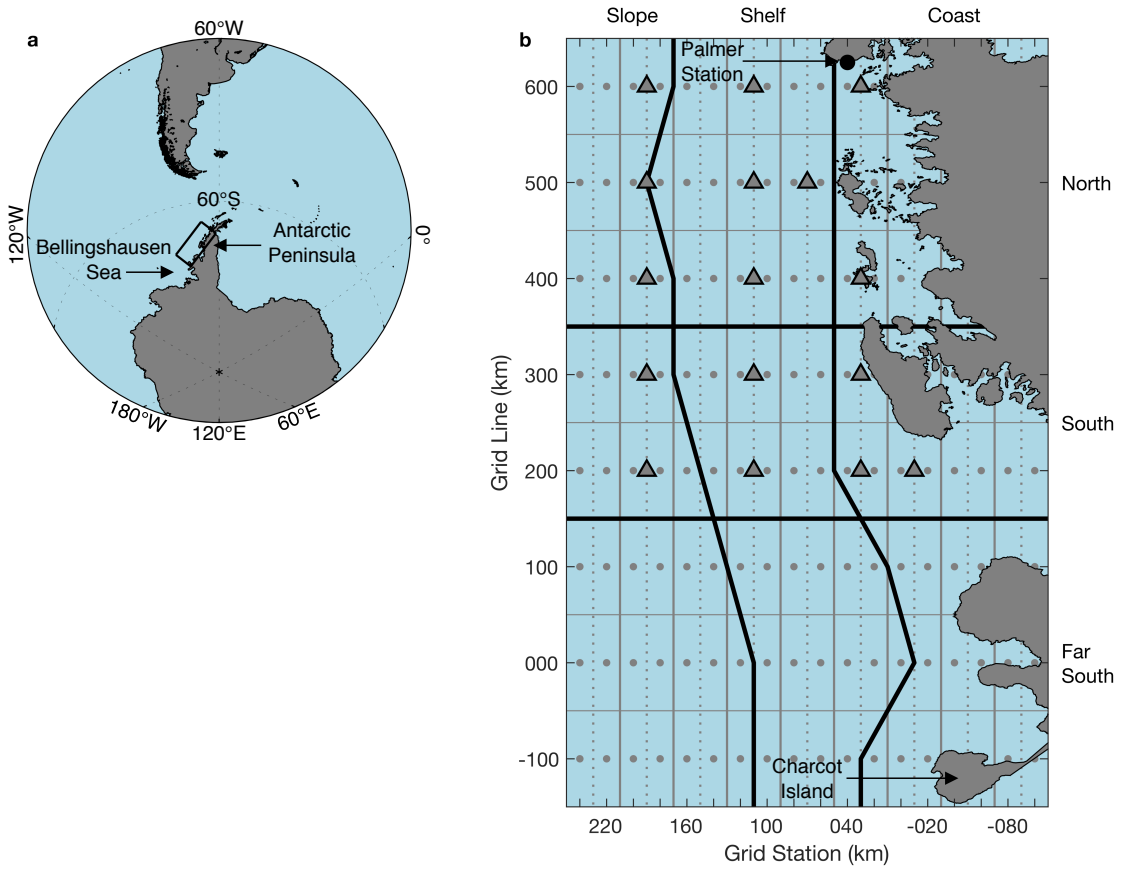

Figure 2.1. Study area. **a-b**, The Southern Ocean and Antarctic continent (**a**), with a blowup of the Palmer LTER regional sampling grid along the mid/southern WAP (**b**). In **b**, the gray dots and gray dotted lines indicate individual sampling stations and their borders, respectively. The gray solid lines indicate groups of two sampling stations. The black solid lines indicate the sub-regions of the Palmer LTER regional sampling grid, including the north to far south and slope to coast. Groups of two sampling stations encompassing stations that are typically visited each year are marked with gray triangles, and were used for the regional and sub-regional time series. The grid lines/stations are relative to a location in the far south/coast.

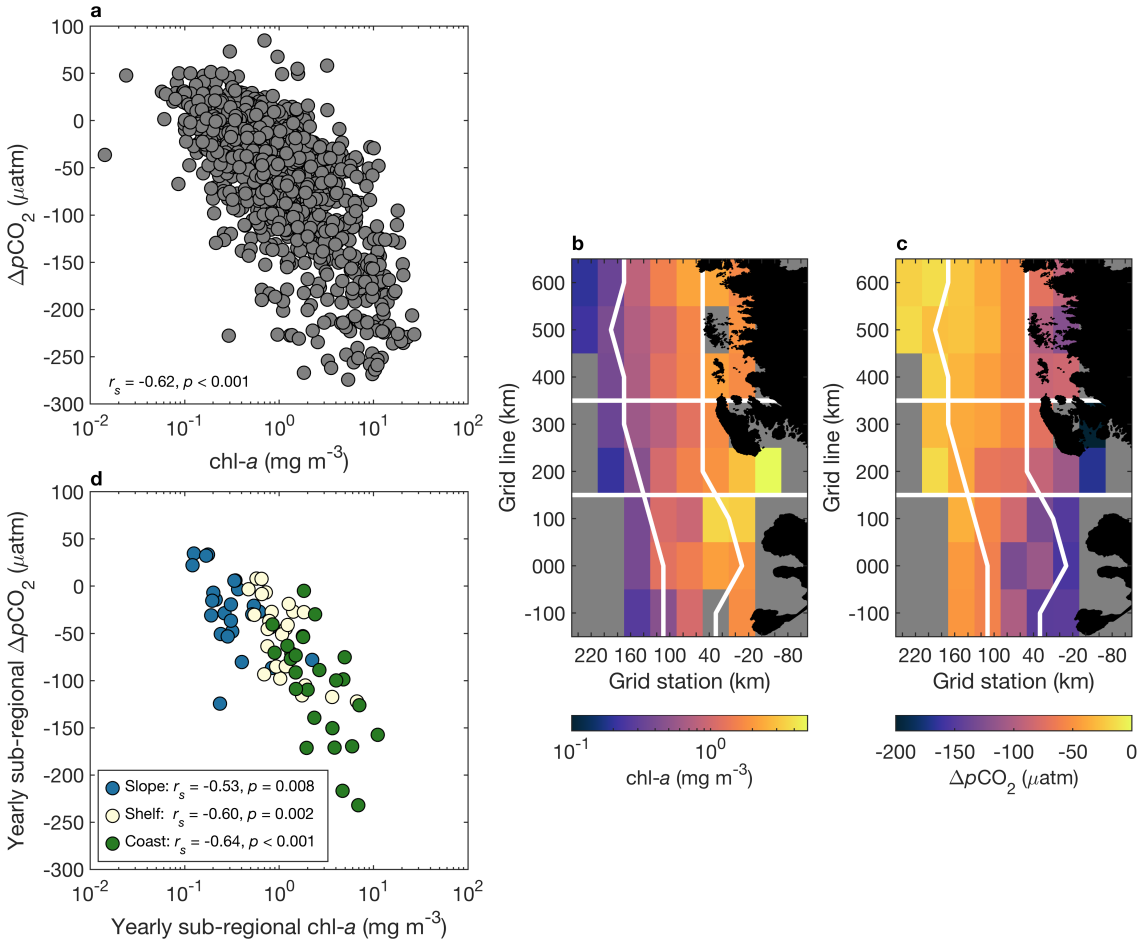

Figure 2.2. Relationship between summer WAP phytoplankton biomass and oceanic CO_2 uptake. **a**, Scatter plot of ΔpCO_2 vs. chl-*a* via fluorescence. **b**-**c**, Climatologies of chl-*a* (**b**) and ΔpCO_2 (**c**). **d**, Scatter plot of yearly sub-regional (Figure 2.1b) ΔpCO_2 vs. chl-*a*. In **a** and **d**, r_s is Spearman's rho, and n = 1151 and 25, respectively.

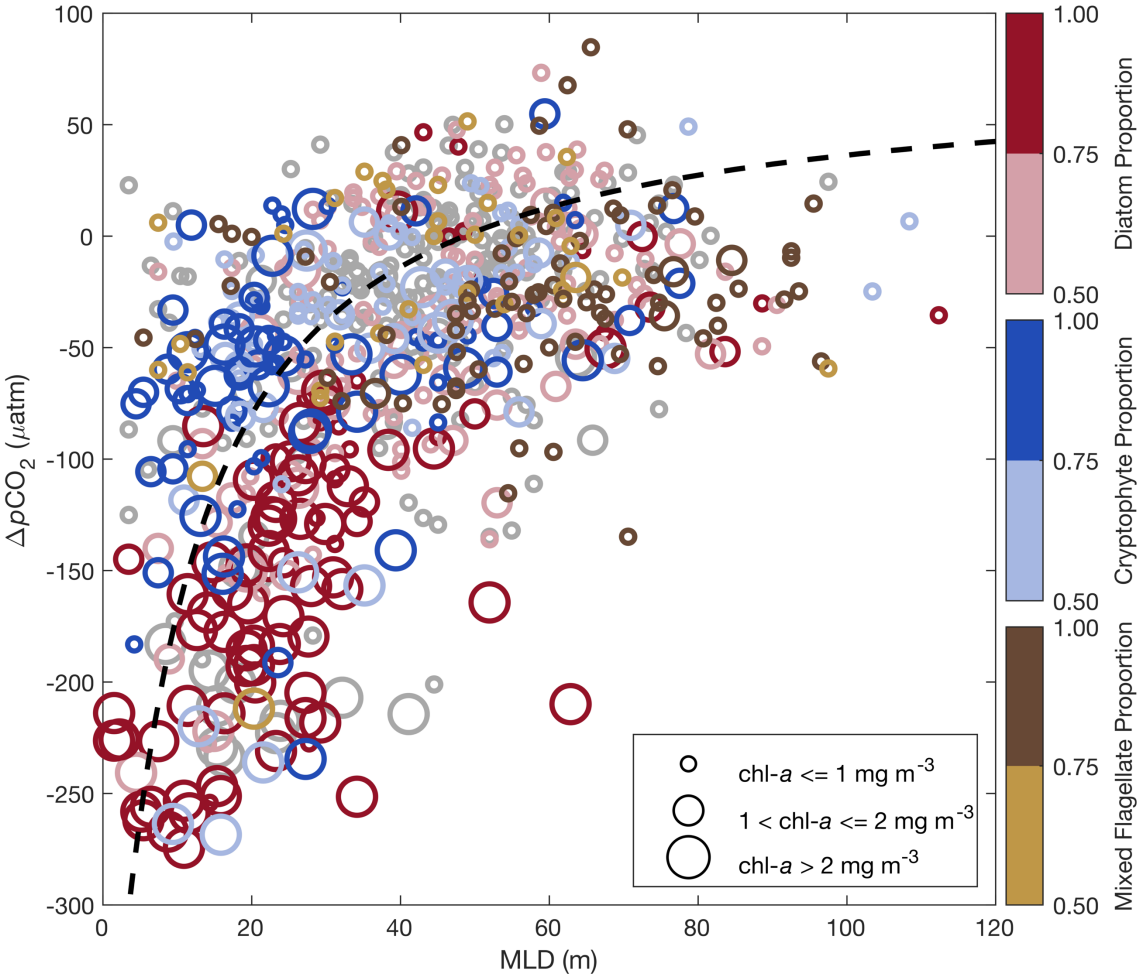

Figure 2.3. Relationship between summer WAP upper ocean stability, phytoplankton dynamics, and oceanic CO_2 uptake. Symbol size indicates chl-*a* via HPLC. Symbol color indicates diatom, cryptophyte, or mixed flagellate proportion (gray indicates neither group dominated, i.e. ≥ 50% of total chl-*a*). The black dashed line indicates ΔpCO_2 modeled as a function of MLD with a constant rate of biological production (2.4: Methods). Here n = 702.

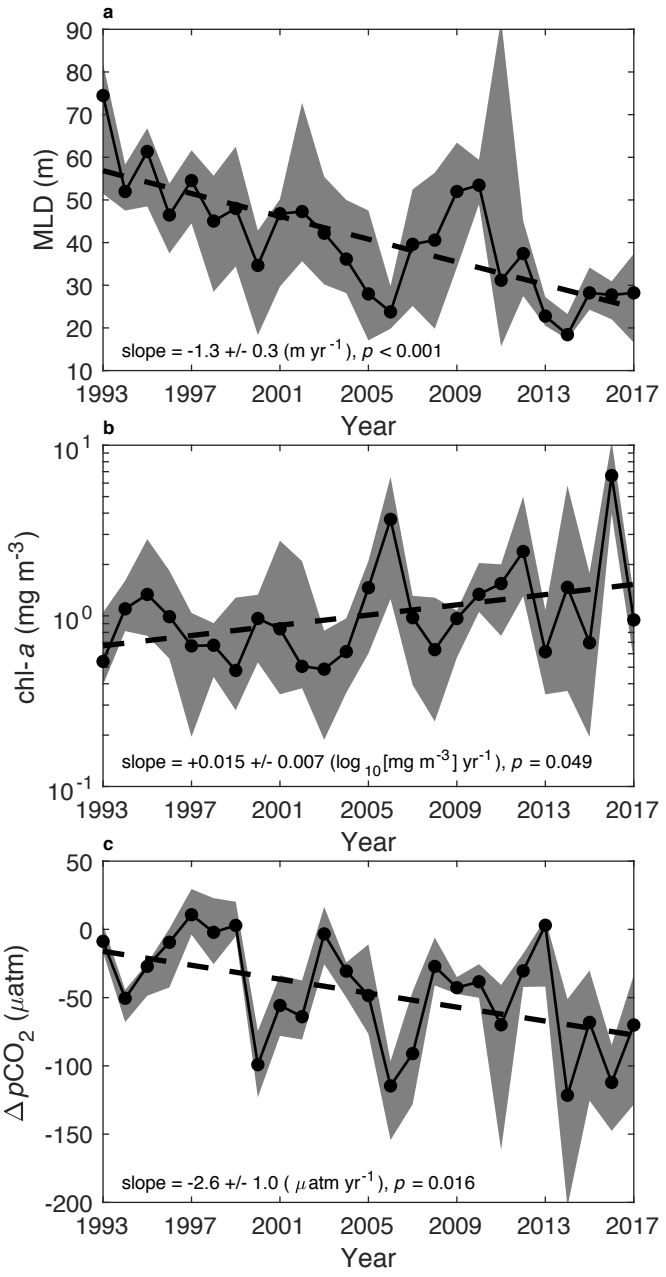

Figure 2.4. Trends in summer WAP regional upper ocean stability, phytoplankton biomass, and oceanic CO_2 uptake. **a-c**, Time series of regional MLD (**a**), chl-*a* via fluorescence (**b**), and ΔpCO_2 (**c**). The black solid lines and circles indicate yearly median values of observations at the Palmer LTER regional sampling grid stations that are typically visited each year (Figure 2.1b; 2.4: Methods). The gray bands indicate the interquartile range. The black dashed lines indicate the linear temporal trend (n = 25).

2.4 Methods

2.4.1 Palmer LTER

Data for this study were collected over 25 years during the Palmer Long-Term Ecological Research (LTER) program annual regional research cruises conducted each austral summer month of January from 1993 to 2017 (1993 to 1997 aboard the MV *Polar Duke*; 1998 to 2017 aboard the ARSV *Laurence M. Gould*) along the mid/southern West Antarctic Peninsula (WAP). The Palmer LTER regional sampling grid spans from Palmer Station in the north to Charcot Island in the south, and from the coast to the slope (Figure 2.1b) (Ducklow et al. 2013). The regional sampling grid consists of grid lines 100 km apart that lie perpendicular to the WAP coastline, with sampling stations located 20 km apart from the coast to the slope (Figure 2.1b) (Waters and Smith 1992). From 1993 to 2008, lines 600 to 200 were primarily sampled, although line 100 was sampled in 2007 and 2008. In 2009, the grid was expanded in the south to include lines 000 to -100, which reduced sampling further north. We divide the Palmer LTER regional sampling grid into nine sub-regions, including the north (lines 600 to 400), south (lines 300 to 200), far south (lines 100 to -100), slope, shelf, and coast (Figure 2.1b) (Martinson et al. 2008, Stammerjohn et al. 2008a).

2.4.2 Water column physics and stability

Water column temperature (T; ºC) and salinity (S; PSU) as a function of pressure (p; db) was measured with a SeaBird 911+ CTD (conductivity-temperature-depth instrument). Data were quality-controlled by removing any observations with values outside of realistic environmental ranges, including T: -2 to 4 ºC and S: 30 to 42 PSU.

Seawater thermodynamic calculations were performed with the Gibbs-SeaWater Oceanographic Toolbox for MATLAB (v3.06) (McDougall and Barker 2011). For each CTD cast, profiles of conservative temperature (T_c; °C) were calculated from T, and profiles of absolute salinity (S_a; PSU) were calculated from S. Using p, T_c, and S_a, profiles of density (ρ; kg m^{-3}), potential density referenced to 0 db (ρ_θ; kg m^{-3}), and buoyancy frequency squared (N^2; s^{-2}) were calculated. To define an ecologically-relevant mixed-layer depth (MLD; m) the approach based on maximum N^2 was used (Carvalho et al. 2017). For each CTD cast, MLD was determined as the depth of maximum N^2. Identification of a MLD assumes the existence of a stratified ocean consisting of a homogeneous upper ocean layer overlaying a relatively more heterogeneous layer. To test the validity of this assumption, for each CTD cast, a quality index (QI; dimensionless; 0 to 1) was calculated based on the ratio of the standard deviation of ρ_θ in the MLD to that over a deeper portion of the water column (Lorbacher et al. 2006). The QI facilitated characterization of MLDs determined with certainty ($QI \geq 0.8$), some uncertainty ($0.5 \leq QI < 0.8$), or not at all ($QI < 0.5$). Only MLDs with a $QI \geq 0.5$ were included in this study (75% of CTD casts).

For each CTD cast, surface averages of T, S, and ρ were calculated by averaging any observations between the surface and 5 m, the approximate depth of the ship's surface seawater flow-through system intake. Water column T and S were also recorded with the dissolved inorganic carbon and total alkalinity observations (see below), using either the corresponding CTD cast or the ship's surface seawater flow-through system. Additionally, continuous observations of surface T and S were made from 2003 to 2017 using the ARSV *Laurence M. Gould* surface seawater flow-through system as part of the

Drake Passage Time-Series (DPT) program. These T and S data were quality-controlled, used to calculate ρ, and used to calculate surface averages of T, S, and ρ in the same manner as the CTD casts. The DPT S data for the years 2003 and 2004 were anomalously high and were excluded. A merged surface T/S/ρ dataset was constructed by combining the CTD and DPT surface data. Unless specifically stated, this dataset was used for all analyses involving surface T/S/ρ.

2.4.3 Water column discrete sampling

Water column samples for phytoplankton pigments and dissolved inorganic variables were drawn from Niskin bottles deployed at depth or from the ship's surface seawater flow-through system at underway stations. Chlorophyll-*a* (chl-*a*; mg m^{-3}) was measured with fluorescence (Parsons et al. 1984). From 1993 to 2008, samples for chl-*a* via fluorescence were size-fractionated. Only the ($x > 0.45$ μm), or if missing, the ($(0.45 < x \leq 20$ μm$) + (x > 20$ μm)) size fractions were considered in this study. From 2009 to 2017, GF/F filters (0.70 μm) were used for data collection. Phytoplankton accessory pigments and chl-*a* (all mg m^{-3}) were measured with high-performance liquid chromatography (HPLC), using GF/F filters for data collection. Phytoplankton chemotaxonomy (group proportion of total chl-*a*; dimensionless; 0 to 1) was determined with CHEMTAX (v1.95) using initial pigment ratios derived for the WAP (Kozlowski et al. 2011). The groups resolved included diatoms, cryptophytes, mixed flagellates (small dinoflagellates and unidentified phytoflagellates), prasinophytes, and type-4 haptophytes (*Phaeocystis* spp.). Multiplication of group proportion by total chl-*a* yielded group chl-*a*. In the Palmer LTER database, prasinophytes and type-4 haptophytes rarely contribute

substantially to surface community biomass (i.e. ≥ 50% of total chl-*a*), and were excluded from further analyses. Phytoplankton chemotaxonomy data were excluded for observations where chl-*a* was zero or missing, or fucoxanthin, alloxanthin, or 19′-butanoyloxyfucoxanthin (the primary diatom, cryptophyte, and mixed flagellate chemotaxonomic pigment, respectively) was missing. This quality-control step resulted in the exclusion of phytoplankton chemotaxonomy data for all observations from the year 2000 due to the absence of alloxanthin. Two parallel HPLC chl-*a* datasets were generated, which included either: 1) all observations (used for time series), or 2) only observations with corresponding accessory pigment data (used for chemotaxonomy). HPLC data was missing for the years 2002, 2010, and 2012 due to instrument or freezer failures, and was not yet reported for 2017.

Dissolved inorganic carbon (DIC; μmol kg^{-1}) was measured by coulometric analysis. Total alkalinity (TA; μEq kg^{-1}) was measured by potentiometric titration. Sample collection, handling, and analysis for DIC and TA was performed according to WOCE-JGOFS protocols (Dickson and Goyet 1994), using certified reference materials provided by A. Dickson (Scripps Institute of Oceanography), with a measurement precision of ± 2 μmol kg^{-1} and ± 5 μEq kg^{-1}, respectively (Hauri et al. 2015). Samples for DIC and TA, from the same sample bottle preserved with 200 μL of saturated $HgCl_2$, were typically analyzed within six months of collection at the University of Hawaii (1993 to 2002), Virginia Institute of Marine Science (2003 to 2007), the Marine Biological Laboratory (2008 to 2013), or Lamont-Doherty Earth Observatory (2014 to 2017). DIC measurements were corrected for the $HgCl_2$ addition with a dilution factor. Any DIC or TA observation pseudoreplicates were averaged. TA data was missing for the years 2003

and 2004. Dissolved inorganic macronutrients, including nitrate, nitrite, phosphate, and silicate (all μmol L^{-1}), were measured by continuous flow analyzers. Depending on the study year, the nitrate/nitrite dataset was reported as either: 1) just nitrate, 2) just nitrate+nitrite, or 3) nitrate, nitrite, and nitrate+nitrite. Given nitrite is typically low relative to nitrate (Kim et al. 2016), a continuous nitrate+nitrite dataset (henceforth nitrate) was constructed using the nitrate+nitrite data, or if missing and nitrate was present, the sum of nitrate and nitrite. Phosphate data was missing for the year 1997, and all macronutrients were missing for 1998.

Observations with ambiguous time, event number, latitude/longitude, or depth metadata were excluded. Data were quality-controlled by excluding any observations with values outside of realistic environmental ranges, including chl-*a*: 0 to 60 mg m^{-3}; DIC: 1800 to 2300 μmol kg^{-1}; TA: 2000 to 2500 μEq kg^{-1}; nitrate: 0 to 50 μmol L^{-1}; phosphate: 0 to 5 μmol L^{-1}; and silicate: 0 to 175 μmol L^{-1}. Replicate observations per depth were averaged. Surface averages of all variables were calculated by averaging observations between 0 to 5 m, the approximate depth of the ship's surface seawater flow-through system intake. Surface averages of phytoplankton group proportion were computed as the ratio of surface group chl-*a* to surface total chl-*a*. Surface averages of salinity-normalized DIC (sDIC; μmol kg^{-1}) and TA (sTA; μEq kg^{-1}) were computed using a reference value of 33.4 PSU (the historic average of all single-station bins). For each surface DIC and TA observation, if either surface T or S were not recorded, they were calculated from any of the merged surface T/S/ρ dataset observations within the nearest single station bin, or if either were missing, the nearest double station bin, weighted by their inverse distance to the DIC and TA observation (Figure 2.1b). Surface averages of

nitrate, phosphate, and silicate were converted to units of μmol kg^{-1} using surface ρ. For each macronutrient observation, surface S and ρ was calculated from any of the merged surface T/S/ρ dataset observations within the nearest single station bin, or if either were missing, the nearest double station bin, weighted by their inverse distance to the macronutrient observation (Figure 2.1b). Surface averages of salinity-normalized nitrate, phosphate, and silicate were calculated as above for sDIC and sTA.

2.4.4 Observation and estimation of $pCO_{2,sur}$ and ΔpCO_2

Continuous observations of surface CO_2 partial pressure ($pCO_{2,sur}$; μatm) were made from 2003 to 2017 using a 30 L shower-type air-water equilibrator and infra-red CO_2 analyzer integrated into the ARSV *Laurence M. Gould* surface seawater flow-through system as part of the DPT program according to Munro et al. 2015. (i.e. $pCO_{2,sur,DPT}$). Data for the year 2016 were not present in the Surface Ocean CO_2 Atlas (v6) dataset (SOCAT) (Bakker et al. 2016), and therefore were excluded. Discrete estimates of surface $pCO_{2,sur}$ were made from 1993 to 2017 using the surface averages of Palmer LTER DIC, TA, T, S, phosphate, and silicate with CO2SYS for MATLAB (v1.1) (van Heuven et al. 2011) using dissociation constants for carbonic acid provided by Lueker et al. (2000) (i.e. $pCO_{2,sur,LTER}$). For each DIC observation missing a paired TA observation, TA was estimated (TA_{est}; μEq kg^{-1}) from S according to: $TA_{est} = (S)(57.01) + 373.86$, as described in Hauri et al. (2015). If either surface T or S were not recorded, they were calculated from the merged surface T/S/ρ dataset as described above. Values for surface phosphate and silicate were calculated in the same fashion, or if missing, from the climatology of the nearest double-station bin (Figure 2.1b).

The relationship between $pCO_{2,sur,LTER}$ and $pCO_{2,sur,DPT}$ was assessed with a match-up analysis. For each $pCO_{2,sur,LTER}$ observation, any $pCO_{2,sur,DPT}$ observations within 1 day and 1 km were averaged (i.e. $pCO_{2,sur,DPT,match}$). Any values of $pCO_{2,sur,LTER}$ or $pCO_{2,sur,DPT,match}$ less (greater) than the 0.5^{th} (99.5^{th}) percentiles of $pCO_{2,sur,DPT,match}$ were removed. A major axis Type II linear regression model was then constructed between $pCO_{2,sur,LTER}$ and $pCO_{2,sur,DPT,match}$ using MATLAB (Supplementary Figure 2.7). This regression model was used to estimate $pCO_{2,sur,DPT}$ from $pCO_{2,sur,LTER}$ (i.e. $pCO_{2,sur,DPT,est}$).

Atmospheric CO_2 partial pressure ($pCO_{2,atm}$; µatm) was determined using atmospheric pressure (mb) and the dry air mole fraction of CO_2 in the atmosphere ($xCO_{2,atm}$; ppm). For the DPT observations, $pCO_{2,atm}$ (i.e. $pCO_{2,atm,DPT}$) used atmospheric pressure from the ARSV *Laurence M. Gould*. For the LTER observations, $pCO_{2,atm}$ (i.e. $pCO_{2,atm,LTER}$) used atmospheric pressure from Palmer Station. For both DPT and LTER observations, xCO_2 was determined at the ship location using the NOAA Earth System Research Laboratory Greenhouse Gas Marine Boundary Layer Reference (Dlugokencky et al. 2017). The ocean-atmosphere CO_2 partial pressure difference was determined by subtracting $pCO_{2,atm}$ from $pCO_{2,sur}$ (ΔpCO_2; µatm). For the DPT observations, ΔpCO_2 (i.e. $\Delta pCO_{2,DPT}$) was determined by subtracting $pCO_{2,atm,DPT}$ from $pCO_{2,sur,DPT}$. For the LTER observations, ΔpCO_2 (i.e. $\Delta pCO_{2,DPT,est}$) was determined by subtracting $pCO_{2,atm,LTER}$ from $pCO_{2,sur,DPT,est}$. The 1993 to 2017 $pCO_{2,sur}$ and ΔpCO_2 datasets used for this study were constructed by merging $pCO_{2,sur,DPT,est}$ and $\Delta pCO_{2,DPT,est}$ for 1993 to 2002 and 2016 with $pCO_{2,sur,DPT}$ and $\Delta pCO_{2,DPT}$ for 2003 to 2015 and 2017.

2.4.5 Modeling of ΔpCO_2

The relationship between ΔpCO_2 and MLD given a constant rate of biological production was modeled (Figure 2.3). A winter water DIC (DIC_{ww}) value of 2180 μmol kg^{-1} was determined based on the analysis of Hauri et al. (2015). A seasonal-integrated (Nov. through Jan.) net community production (NCP_{ndj}) value of 1.3 mol C m^{-2}, integrated to the MLD, was determined by estimating an average seasonal daily NCP value of 30 mmol O_2 m^{-2} day^{-1} from Li et al. (2016), converting to units of C using a photosynthetic quotient of 1.4, and assuming 60 days of NCP prior to observation by the Palmer LTER annual regional research cruise during summer. A summer surface D (D_{su}) value of 1027 kg m^{-3} was determined with the historic average of all single-station bins (Figure 2.1b). For each MLD spanning 1 to 120 m, the corresponding seasonal DIC drawdown (DIC_{dd}; μmol kg^{-1}) was computed according to: $DIC_{dd} = [(NCP_{ndj})(10^6)] / [(D_{su})(MLD)]$, and summer surface DIC was computed by subtracting DIC_{dd} from DIC_{ww}. Next, summer surface TA, T, S, phosphate, and silicate values of 2283 μEq kg^{-1}, 1 °C, 33.4 PSU, 1 μmol kg^{-1}, and 53 μmol kg^{-1}, respectively, were determined with the historic average of all single-station bins (Figure 2.1b). For each MLD, summer $pCO_{2,sur}$ was calculated using the summer surface DIC, TA, T, S, phosphate, and silicate values with CO2SYS for MATLAB (v1.1) (van Heuven et al. 2011) using dissociation constants for carbonic acid provided by Lueker et al. (2000), and summer ΔpCO_2 was calculated by subtracting a $pCO_{2,atm}$ value of 365 μatm (the 1993 to 2017 average) from summer $pCO_{2,sur}$.

2.4.6 Drivers of $pCO_{2,sur}$

Following the approach of Lenton et al. (2012) and Munro et al. (2015), growth rates of $pCO_{2,sur}$ drivers, including surface T, S, DIC, and TA, were calculated and converted into units of $pCO_{2,sur}$ using the approximations of Takahashi et al. (1993) and Takahashi et al. (2014) (Supplementary Table 2.1-2.2 & Figure 2.6). Revelle factors of 15 and -15 for DIC and TA, respectively, were used based on approximations presented by Sarmiento and Gruber (2006). Additionally, following the approach of Lovenduski et al. (2007), growth rates of sDIC and sTA were calculated and converted into units of $pCO_{2,sur}$ to separate the indirect influence of a long-term change in S through DIC and TA on $pCO_{2,sur}$. The growth rate in $pCO_{2,sur}$ due to sDIC was further divided into components due to long-term changes in oceanic uptake of anthropogenic CO_2 ($sDIC_{ant}$) and biological DIC drawdown ($sDIC_{bio}$). An estimate of 0.79 ± 0.16 μmol kg^{-1} yr^{-1} was used for $sDIC_{ant}$, based on the anthropogenic DIC increase of 12 to 18 μmol kg^{-1} over 19 years in Antarctic Surface Water reported by Williams et al. (2015), who used repeat hydrography observations from 1992 to 2011 along line S04P (see also their Figure 5c). Time series trends and averages used in this analysis are presented in Supplementary Table 2.1-2.2.

2.4.7 Statistics

Surface data were binned to different spatial scales depending on the analysis. For each year, data were spatially-averaged into 100×20 km (along-shore×cross-shore) bins encompassing a single Palmer LTER regional sampling grid station, i.e. single-station bins (Figure 2.1b). This facilitated the direct comparison of different variables (Figure

2.2a, 2.3; Supplementary Figure 2.3-2.5). Single-station bins of phytoplankton group proportion were computed as the ratio of average group chl-*a* to average total chl-*a*. The single-station chl-*a* via fluorescence and HPLC data were $\log_{10}$-transformed for normality. To account for rare zero values, a small offset (~10% of the minimum non-zero value) was first added to the chl-*a* via HPLC data. Henceforth, unless noted, analyses were performed on the $\log_{10}$-transformed (i.e. not linear) chl-*a* via fluorescence and HPLC data. Due to a large number of zero values, the single-station group chl-*a* data were not $\log_{10}$-transformed (zero values of group proportion yielded zero values of group chl-*a*). Given that each station is not visited every year, for each year, the single-station bins were spatially averaged into 100×40 km (along-shore×cross-shore) bins encompassing two Palmer LTER regional sampling grid stations, i.e. double-station bins (Figure 2.1b). For the chl-*a* via fluorescence, ΔpCO_2, and MLD climatologies (Figure 2.2b-c; Supplementary Figure 2.1), only double-station bins with observations for at least one third of the time series were included (9 and 3 years for the north/south and far south sub-regions, respectively). To compare yearly sub-regional (slope, shelf, and coast sub-regions) chl-*a* via fluorescence and ΔpCO_2 (Figure 2.2d), for each year, the corresponding single-station bins were spatially-averaged.

To construct regional and sub-regional (north and south sub-regions) time series (Figure 2.4; Supplementary Table 2.1-2.2 & Figure 2.6), the 16 double-station bins encompassing the Palmer LTER regional sampling grid stations used by Schofield et al. (2018) that are typically visited each year were used (Figure 2.1b). Regional time series used all 16 bins, and sub-regional time series used the corresponding 9 or 7 (north or south sub-region) bins. For each year, the median, and 25th and 75th percentiles of the

bins were calculated. The median was used to reduce skew in the regional and sub-regional estimates due to any extreme values and strong cross-shore patterns.

To examine the relationship between chl-*a* via fluorescence and ΔpCO_2 (Figure 2.2a,d), two-sided Spearman rhos were calculated using MATLAB. To determine temporal trends and averages in regional and sub-regional time series, Type I linear regression models were constructed between variables and study year using MATLAB (Figure 2.4; Supplementary Table 2.1-2.2 & Figure 2.6). To examine differences in chl-*a* via HPLC, ΔpCO_2, MLD, T, S, sDIC, and salinity-normalized nitrate and phosphate between diatom, cryptophyte, and mixed flagellate assemblages (Supplementary Figure 2.3-2.5), Kruskal-Wallis tests and post hoc pairwise multiple comparisons with a Bonferroni adjustment were performed using Statistica. This is a nonparametric test. Diatom, cryptophyte, and mixed flagellate assemblages were functionally defined as observations with group chl-*a* $\geq$ 75% of total chl-*a*. The locations of diatom, cryptophyte, and mixed flagellate assemblages observed from 1993 to 2017 are shown in Supplementary Figure 2.2. All three groups are observed on the slope, shelf, and coast. However, diatoms occur more frequently than the other groups on the slope and in the far south, as they often bloom along the ice edge and earlier in the season (summer conditions occur later further south) (Schofield et al. 2017).

2.5 Supplementary tables

Supplementary Table 2.1. Summer WAP regional and sub-regional time series trends. Presented are regional and sub-regional (north and south sub-regions; Figure 2.1b) time series trends during summer along the mid/southern WAP from 1993 to 2017 (2.4: Methods). Here, chl-a_F is chl-*a* via fluorescence, chl-a_H is chl-*a* via HPLC, and chl-a_D, chl-a_C, and chl-a_M are phytoplankton group chl-*a* for diatoms, cryptophytes, and mixed flagellates, respectively. For each variable, the time series slope (± standard error), *p*-value, and *n* is indicated, respectively. Trends are colored red (+) or blue (-) when moderately significant ($p < 0.10$), and bolded when significant ($p < 0.05$). The dashed horizontal line separates variables used for the $pCO_{2,sur}$ driver analysis.

	North sub-region	South sub-region	Regional
MLD (m yr^{-1})	-0.941 (± 0.469), 0.057, 25	**-1.437 (± 0.253), <0.001, 25**	**-1.336 (± 0.255), <0.001, 25**
chl-a_F (log10[mg m^{-3}] yr^{-1})	+0.011 (± 0.007), 0.110, 25	**+0.020 (± 0.009), 0.039, 25**	**+0.015 (± 0.007), 0.049, 25**
chl-a_H (log10[mg m^{-3}] yr^{-1})	+0.012 (± 0.009), 0.164, 21	**+0.032 (± 0.010), 0.004, 21**	**+0.021 (± 0.008), 0.012, 21**
chl-a_D (mg m^{-3} yr^{-1})	+0.005 (± 0.010), 0.635, 20	**+0.076 (± 0.033), 0.035, 20**	+0.014 (± 0.012), 0.259, 20
chl-a_C (mg m^{-3} yr^{-1})	**+0.024 (± 0.010), 0.028, 20**	**+0.024 (± 0.010), 0.033, 20**	**+0.018 (± 0.006), 0.011, 20**
chl-a_M (mg m^{-3} yr^{-1})	**-0.008 (± 0.004), 0.041, 20**	-0.004 (± 0.006), 0.544, 20	-0.005 (± 0.005), 0.300, 20
ΔpCO_2 (µatm yr^{-1})	-1.547 (± 0.812), 0.069, 25	**-4.606 (± 1.487), 0.005, 25**	**-2.556 (± 0.984), 0.016, 25**
$pCO_{2,sur}$ (µatm yr^{-1})	+0.283 (± 0.809), 0.730, 25	-2.846 (± 1.493), 0.069, 25	-0.757 (± 0.989), 0.452, 25
DIC (µmol kg^{-1} yr^{-1})	-0.162 (± 0.494), 0.746, 25	**-1.987 (± 0.755), 0.015, 25**	-0.767 (± 0.515), 0.150, 25
TA (µEq kg^{-1} yr^{-1})	-0.533 (± 0.432), 0.229, 25	**-1.136 (± 0.511), 0.036, 25**	-0.851 (± 0.417), 0.053, 25
sDIC (µmol kg^{-1} yr^{-1})	+0.297 (± 0.259), 0.263, 25	-0.860 (± 0.623), 0.181, 25	+0.043 (± 0.317), 0.893, 25
sTA (µEq kg^{-1} yr^{-1})	-0.207 (± 0.214), 0.342, 25	+0.163 (± 0.264), 0.544, 25	-0.085 (± 0.217), 0.700, 25
T (ºC yr^{-1})	-0.012 (± 0.016), 0.440, 25	-0.028 (± 0.019), 0.152, 25	-0.017 (± 0.016), 0.310, 25
S (PSU yr^{-1}`)	-0.008 (± 0.007), 0.259, 25	**-0.021 (± 0.008), 0.016, 25**	-0.013 (± 0.007), 0.070, 25

Supplementary Table 2.2. Summer WAP regional and sub-regional time series averages. Presented are regional and sub-regional (north and south sub-regions; Figure 2.1b) time series averages during summer along the mid/southern WAP from 1993 to 2017 for variables used in the $pCO_{2,sur}$ driver analysis (2.4: Methods). For each variable, the time series average (± standard error) and *n* is indicated, respectively.

	North sub-region	**South sub-region**	**Regional**
$\boldsymbol{pCO_{2,sur}}$ (µatm)	324.107 (± 5.727), 25	300.188 (± 11.343), 25	316.118 (± 7.067), 25
DIC (µmol kg^{-1})	2132.00 (± 3.495), 25	2112.90 (± 6.078), 25	2125.70 (± 3.807), 25
TA (µEq kg^{-1})	2290.30 (± 3.146), 25	2283.00 (± 3.975), 25	2288.10 (± 3.199), 25
sDIC (µmol kg^{-1})	2118.20 (± 1.879), 25	2105.70 (± 4.576), 25	2115.00 (± 2.238), 25
sTA (µEq kg^{-1})	2275.90 (± 1.538), 25	2276.40 (± 1.878), 25	2275.90 (± 1.535), 25
T (ºC)	1.077 (± 0.111), 25	0.951 (± 0.139), 25	1.008 (± 0.118), 25
S (PSU)	33.634 (± 0.047), 25	33.483 (± 0.063), 25	33.585 (± 0.051), 25

2.6 Supplementary figures

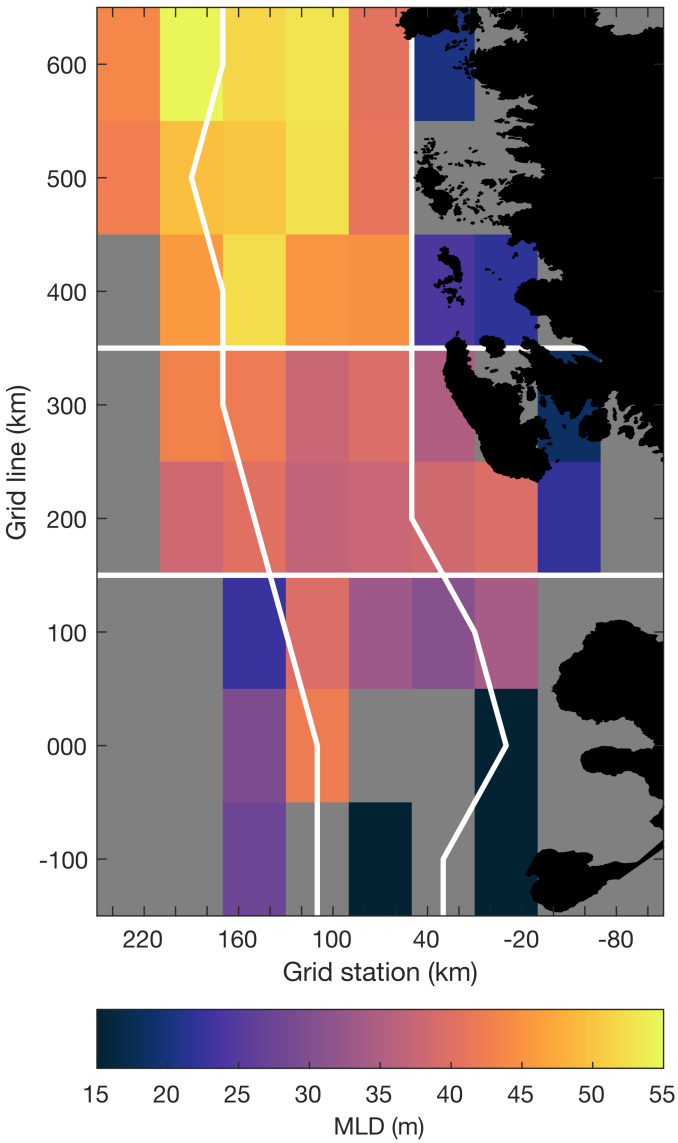

Supplementary Figure 2.1. Summer WAP upper ocean stability. MLD climatology.

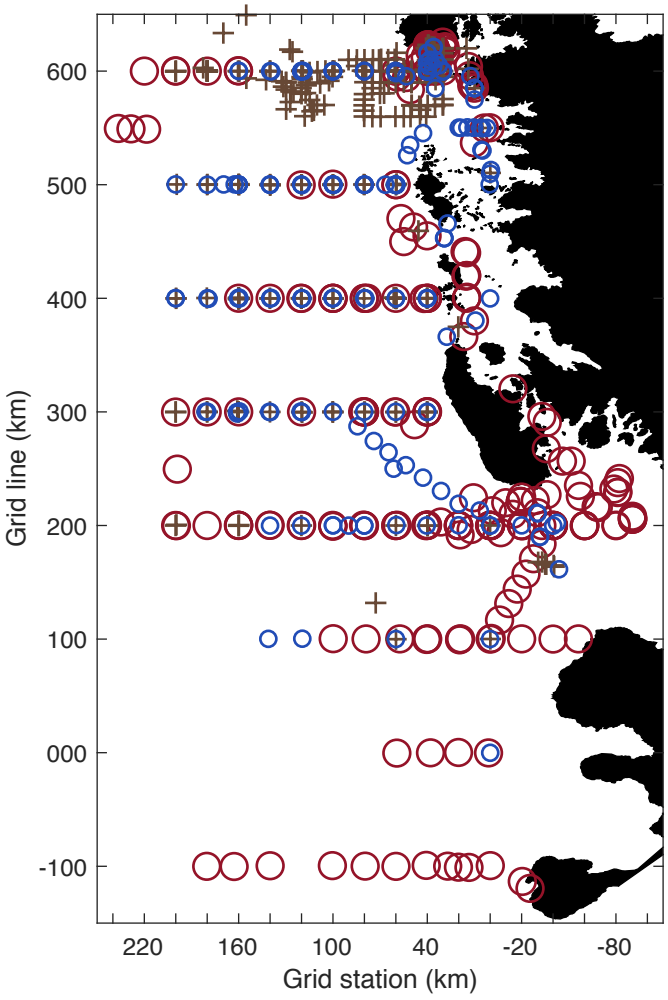

Supplementary Figure 2.2. Summer WAP phytoplankton assemblages. Locations of surface diatom (red circles), cryptophyte (blue circles), and mixed flagellate (brown pluses) assemblages (i.e. ≥ 75% of total chl-*a*) from 1993 to 2017.

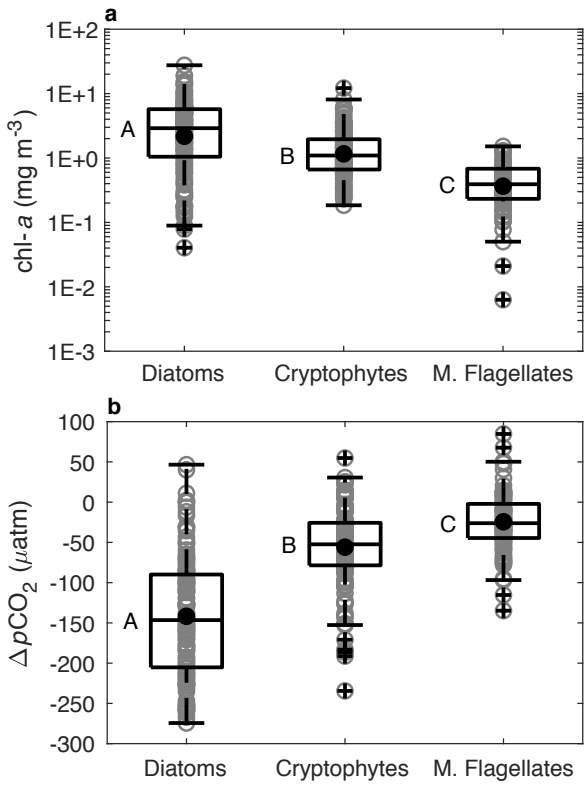

Supplementary Figure 2.3. Differences in biomass and oceanic CO_2 uptake between summer WAP phytoplankton assemblages. **a-b**, Box plots of chl-*a* via HPLC (**a**) and ΔpCO_2 (**b**) for diatom, cryptophyte, and mixed flagellate assemblages (i.e. ≥ 75% of total chl-*a*). The horizontal lines of the boxes indicate the median and 25th and 75th percentiles, and black circles indicate the mean. The gray circles indicate individual values. The whiskers extend to values not considered as outliers, with outliers indicated by black pluses. The presence of a difference among groups was determined with Kruskal-Wallis tests (2.4: Methods) (**a**: $H_2 = 132$, $p < 0.001$; **b**: $H_2 = 150$, $p < 0.001$). The capital letters indicate statistical groupings at $\alpha = 0.05$ based on post hoc pairwise multiple comparisons with a Bonferroni adjustment. In **a-b**, n = 144, 136, and 107 (**a**); and 129, 126, and 102 (**b**) for diatoms, cryptophytes, and mixed flagellates, respectively.

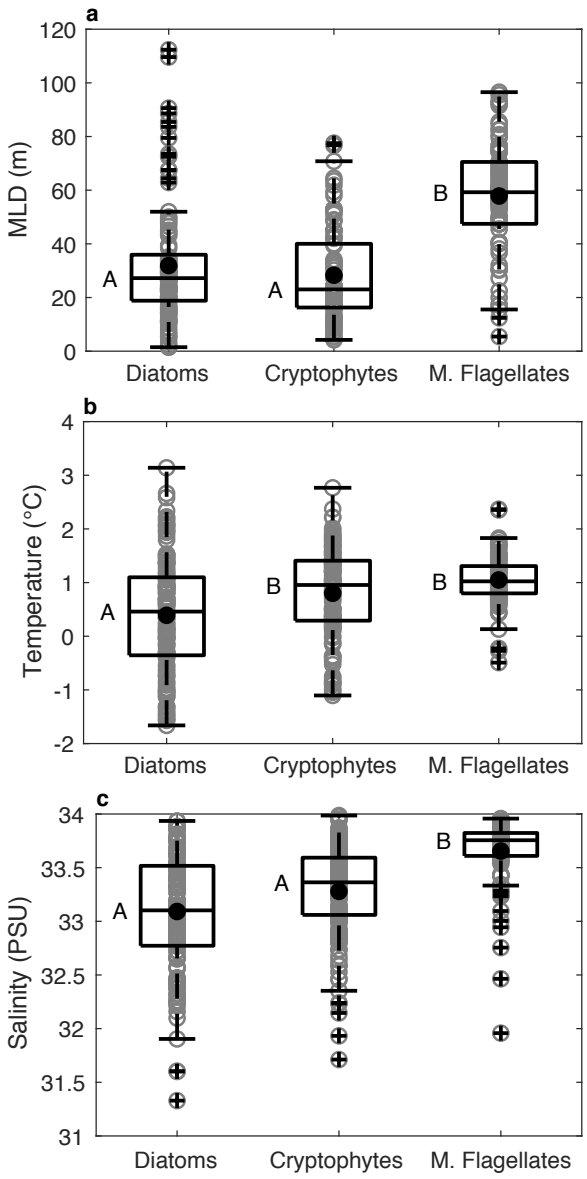

Supplementary Figure 2.4. Differences in physical water mass properties between summer WAP phytoplankton assemblages. **a-c**, Box plots of MLD (**a**) T (**b**) and S (**c**) for diatom, cryptophyte, and mixed flagellate assemblages (i.e. ≥ 75% of total chl-*a*). The horizontal lines of the boxes indicate the median and 25th and 75th percentiles, and black circles indicate the mean. The gray circles indicate individual values. The whiskers extend to values not considered as outliers, with outliers indicated by black pluses. The presence of a difference among groups was determined with Kruskal-Wallis tests (2.4: Methods) (**a**: $H_2 = 75.2$, $p < 0.001$; **b**: $H_2 = 31.0$, $p < 0.001$; **c**: $H_2 = 95.0$, $p < 0.001$). The capital letters indicate statistical groupings at $\alpha = 0.05$ based on post hoc pairwise multiple comparisons with a Bonferroni adjustment. In **a-c**, n = 101, 86, and 82 (**a**); 143, 136, and 105 (**b**); and 143, 136, and 105 (**c**) for diatoms, cryptophytes, and mixed flagellates, respectively.

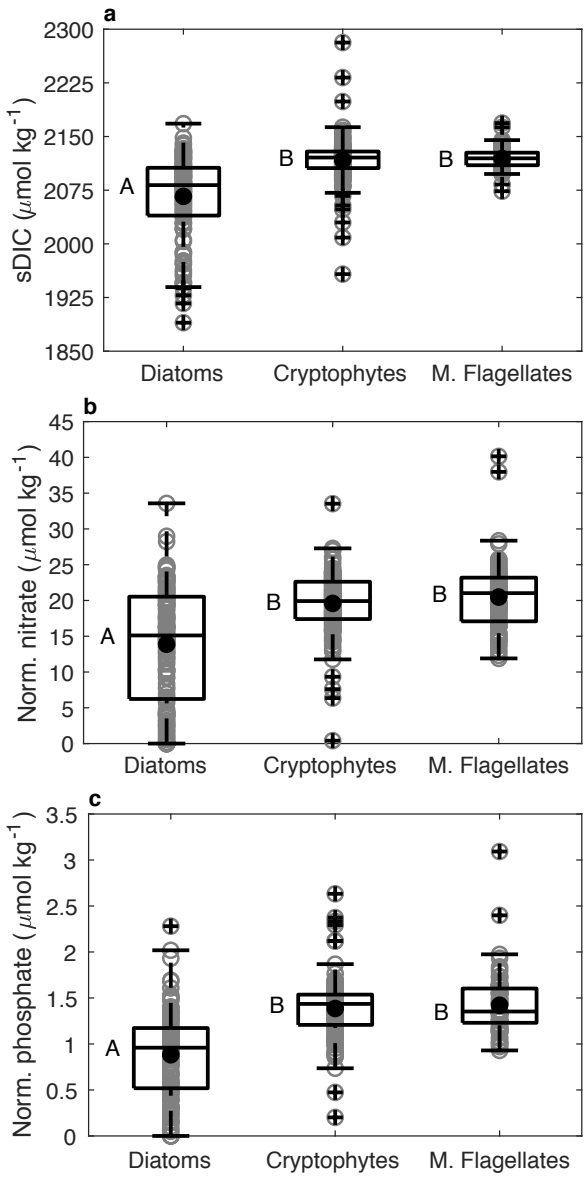

Supplementary Figure 2.5. Differences in dissolved inorganic water mass properties between summer WAP phytoplankton assemblages. **a-c**, Box plots of sDIC (**a**), salinity-normalized nitrate (**b**), and salinity-normalized phosphate (**c**) for diatom, cryptophyte, and mixed flagellate assemblages (i.e. ≥ 75% of total chl-*a*). The horizontal lines of the boxes indicate the median and 25th and 75th percentiles, and black circles indicate the mean. The gray circles indicate individual values. The whiskers extend to values not considered as outliers, with outliers indicated by black pluses. The presence of a difference among groups was determined with Kruskal-Wallis tests (2.4: Methods) (**a**: $H_2 = 95.3$, $p < 0.001$; **b**: $H_2 = 47.9$, $p < 0.001$; **c**: $H_2 = 110$, $p < 0.001$). The capital letters indicate statistical groupings at $\alpha = 0.05$ based on post hoc pairwise multiple comparisons with a Bonferroni adjustment. In **a-c**, n = 119, 131, and 104 (**a**); 137, 126, and 92 (**b**); and 128, 128, and 92 (**c**) for diatoms, cryptophytes, and mixed flagellates, respectively.

Supplementary Figure 2.6. Driver analysis of summer WAP $pCO_{2,sur}$ trend (**next page**). **a-c**, Growth rates from 1993 to 2017 during summer along the mid/southern WAP in $xCO_{2,atm}$ (ppm yr^{-1}) and $pCO_{2,sur}$ (μatm yr^{-1}), and contributions to $pCO_{2,sur}$ based on trends in T, S, DIC, and TA (all μatm yr^{-1}) are presented for the north sub-region (**a**), south sub-region (**b**), and Palmer LTER regional sampling grid (**c**) (Figure 2.1b; 2.4: Methods). The sum of these four $pCO_{2,sur}$ drivers agrees with the $pCO_{2,sur}$ growth rate within their standard error. The $pCO_{2,sur}$ driver analysis indicates that decreases in regional and sub-regional T and S had minimal impacts on the $pCO_{2,sur}$ trend. Additionally, decreases in regional and sub-regional DIC and TA had offsetting impacts on the $pCO_{2,sur}$ trend, due in part to the offsetting influence on $pCO_{2,sur}$ of long-term freshening (i.e. dilution) of these two drivers. Growth rates in $pCO_{2,sur}$ due to sDIC and sTA (both μatm yr^{-1}) are also presented. The growth rate in $pCO_{2,sur}$ due to sDIC was further divided into components due to long-term changes in both biological DIC drawdown and anthropogenic DIC ($sDIC_{bio}$ and $sDIC_{ant}$, respectively; both μatm yr^{-1}). This analysis demonstrates that the trends in regional and sub-regional $pCO_{2,sur}$ (and thus ΔpCO_2) are due to a balance between long-term increases in both biological DIC drawdown and anthropogenic DIC.

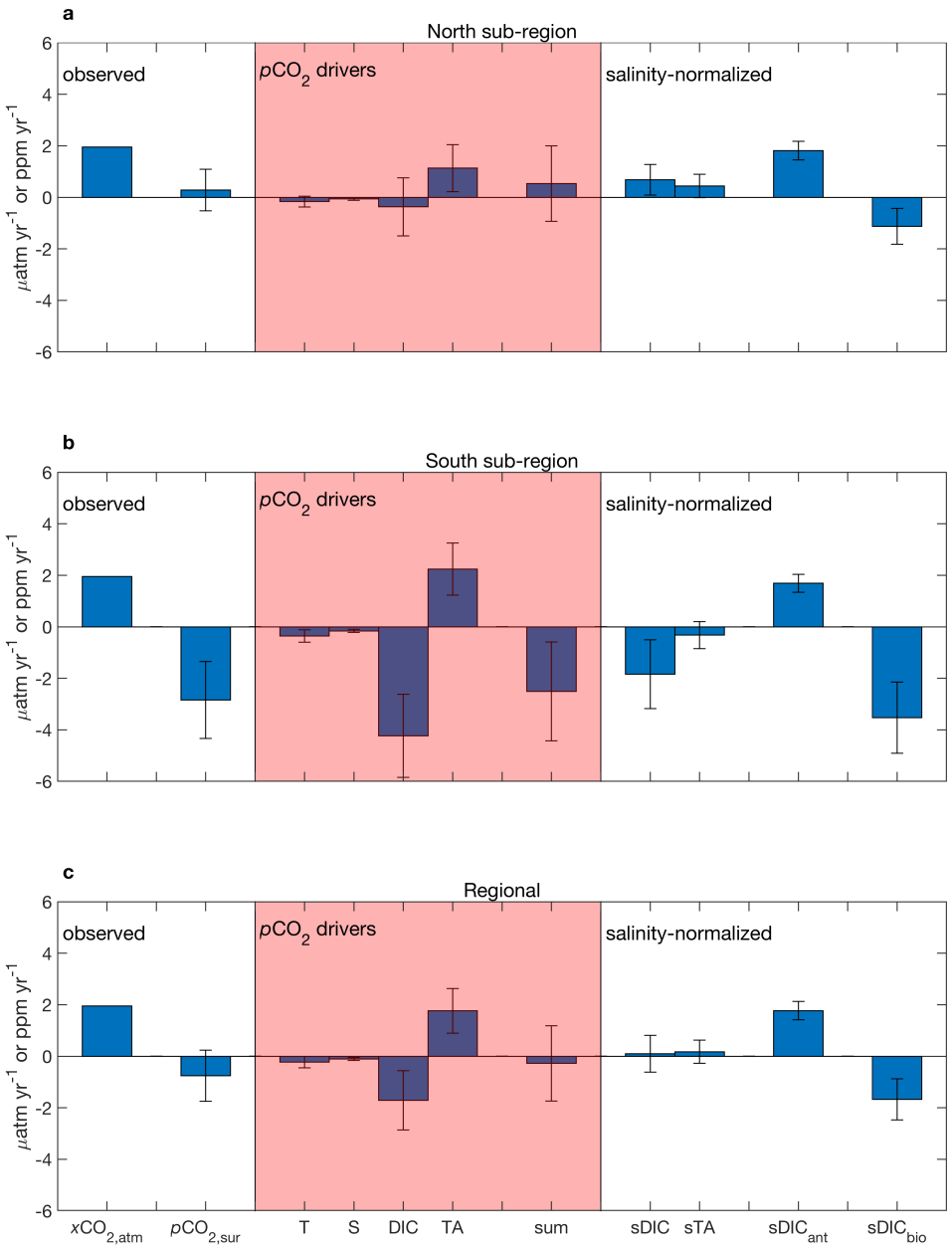
a
North sub-region
observed
pCO2 drivers
salinity-normalized
μatm yr-1 or ppm yr-1
6
4
2
0
-2
-4
-6
b
South sub-region
observed
pCO2 drivers
salinity-normalized
μatm yr-1 or ppm yr-1
c
Regional
observed
pCO2 drivers
salinity-normalized
μatm yr-1 or ppm yr-1
xCO2,atm
pCO2,sur
T
S
DIC
TA
sum
sDIC
sTA
sDICant
sDICbio

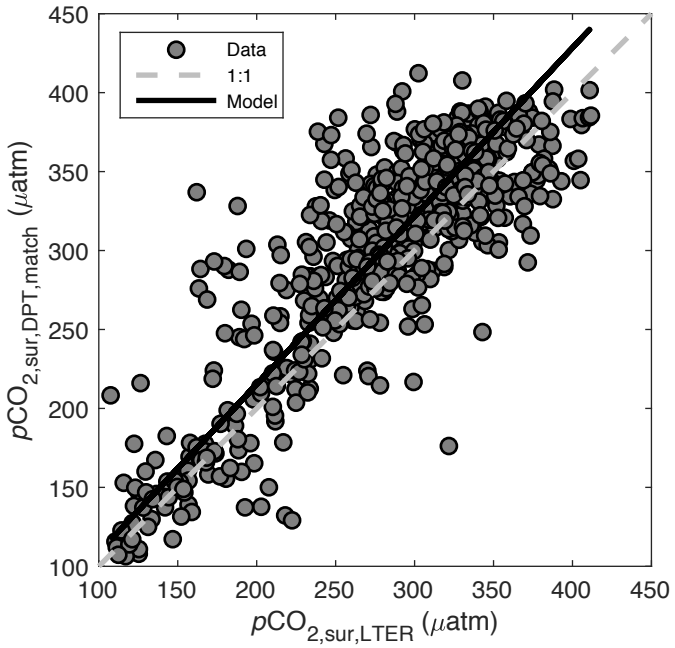

Supplementary Figure 2.7. Relationship between summer WAP $pCO_{2,sur,LTER}$ and $pCO_{2,sur,DPT,match}$. $pCO_{2,sur,LTER}$ was estimated from carbonate system measurements from 1993 to 2017. $pCO_{2,sur,DPT}$ was measured with a flow-through system onboard the ARSV *Laurence M. Gould* from 2003 to 2017 (although the 2016 data was excluded), and matched-up with $pCO_{2,sur,LTER}$ to generate $pCO_{2,sur,DPT,match}$. The black solid line indicates the major axis Type II linear regression model constructed between $pCO_{2,sur,LTER}$ and $pCO_{2,sur,DPT,match}$, and is formulated as: $y = x(1.07 \pm 0.03) + (2.08 \pm 7.61)$, $r = 0.85$, $n = 640$. This model was used to estimate $pCO_{2,sur,DPT}$ (i.e. $pCO_{2,sur,DPT,est}$) from $pCO_{2,sur,LTER}$. The 1993 to 2017 $pCO_{2,sur}$ dataset used for this study was constructed by merging $pCO_{2,sur,DPT,est}$ for 1993 to 2002 and 2016 with $pCO_{2,sur,DPT}$ for 2003 to 2015 and 2017.

3 Low diversity of a key phytoplankton group along the West Antarctic Peninsula

3.1 Abstract

The West Antarctic Peninsula (WAP) is experiencing rapid warming and melting that is impacting the regional marine food web. The primary WAP phytoplankton groups are diatoms and cryptophytes. Relative to diatoms, there has been little focus on WAP cryptophytes, and thus our understanding of their diversity and ecology is limited, especially at the species level. This gap is important, as diatoms and cryptophytes play distinct roles in the regional marine food web and biogeochemistry. In this study, we use a phylogenetic placement approach with 18S rRNA gene amplicon sequence variants to assess WAP cryptophyte diversity and its drivers at a high taxonomic resolution. Data were collected over five years (2012 to 2016) during the regional research cruises of the Palmer Long-Term Ecological Research program. Our results indicate that there are two major WAP cryptophyte taxa, consisting of distinct *Geminigera* spp., which together always comprise nearly 100% of the cryptophyte community. The primary taxon dominates the cryptophyte community across all samples/years, which span a broad range of oceanographic conditions. A shift in cryptophyte community composition between a lower (higher) primary (secondary) taxon percentage is associated with distinct oceanographic conditions, including lower (higher) temperature, salinity, nutrients, and cryptophyte percentage (phytoplankton biomass and diatom percentage). These results emphasize the need for a full characterization of the ecology of these two taxa, as it is

predicted that cryptophytes will increase along the WAP given projections of continued regional environmental change.

3.2 Introduction

Polar oceans play a disproportionately large role in global climate and biogeochemistry (Gruber et al. 2019). Many polar ecosystems are undergoing substantial environmental change (Meredith et al. 2019), including the West Antarctic Peninsula (WAP; Figure 3.1), which is exhibiting some of the most rapid change on the planet (Schofield et al. 2010; Ducklow et al. 2013). Since the mid-twentieth century, the WAP has warmed considerably, including strong positive trends in oceanic temperatures (Meredith and King 2005; Martinson et al. 2008), and one of the largest increases in winter atmospheric temperatures globally (Vaughan et al. 2003). Additionally, there has been widespread glacial retreat in the region (Cook et al. 2016), and the sea ice season has shortened by three months (Stammerjohn et al. 2008a). These changes to the WAP are associated with changes in atmospheric circulation, in particular a deepening of the Amundsen Sea Low driven by a positive trend in the Southern Annular Mode (SAM) (Marshall 2003), which has resulted in stronger and warmer winds blowing from the north/northwest across the region (Raphael et al. 2016). Since Antarctic marine life is dependent on sea ice dynamics, these physical changes to the WAP have impacted the marine food web across all trophic levels (Schofield et al. 2010; Ducklow et al. 2013), including the abundance and composition of regional phytoplankton communities (Moline et al. 2004; Montes-Hugo et al. 2009; Sailley et al. 2013; Brown et al. 2019).

The coastal waters of the WAP are associated with large phytoplankton blooms during spring and summer (Smith et al. 2008). These blooms are fueled by an abundant supply of macronutrients (Kim et al. 2016). Therefore, primary production in the region is generally thought to be controlled by light availability regulated by the mixed-layer depth, which in turn is driven by wind, sea ice, and meltwater dynamics (Vernet et al. 2008; Saba et al. 2014; Brown et al. 2019). Historically, the dominant WAP phytoplankton group has been considered to be diatoms, which are typically large and classified as microplankton, i.e. > 20 μm (Hart 1942). However, over the past few decades it has been recognized that smaller phytoplankton classified as nanoplankton, i.e. < 20 μm, are also important components of the regional phytoplankton community (Hewes et al. 1990; Buma et al. 1991). The dominant WAP nanoplankton group is considered to be cryptophytes (Garibotti et al. 2003; Schofield et al. 2017).

It has been observed that in coastal regions of the WAP, the presence of cryptophytes is associated with lower salinities (Moline et al. 2004; Mendes et al. 2013; Schofield et al. 2017), and years characterized by positive SAM, less sea ice, deeper MLDs, and lower overall phytoplankton biomass (Saba et al. 2014). This has resulted in the prediction that the relative abundance of cryptophytes along the WAP will increase as the region continues to warm and melt (Henley et al. 2019). Indeed, there is evidence that this transition is already occurring (Moline et al. 2004; Montes-Hugo et al. 2009; Sailley et al. 2013; Brown et al. 2019). A shift in regional phytoplankton community composition from diatoms to cryptophytes could impact the WAP marine food web and biogeochemistry. Specifically, given their smaller size, cryptophytes are not as efficiently grazed by krill as diatoms (Haberman et al. 2003), which has implications for higher

trophic levels like penguins and whales (Saba et al. 2014). Additionally, cryptophytes achieve lower oceanic uptake of atmospheric carbon dioxide relative to diatoms (Brown et al. 2019).

Although the importance of cryptophytes to WAP phytoplankton communities is known, they have been the focus of minimal research in the region relative to diatoms (Schofield et al. 2017). In particular, fundamental ecological questions still remain about WAP cryptophytes, including the identity of their major taxa and the drivers of their diversity. Additionally, although some studies have used microscopy to assess phytoplankton dynamics at the genus/species level (Mascioni et al. 2019 and references therein), most work in the region, including that of the Palmer Long-Term Ecological Research (LTER) program, has primarily focused on the use of pigment-based approaches, which only allow classification to lower taxonomic resolutions (e.g. diatoms vs. cryptophytes). However, recent studies from the WAP have demonstrated the importance of classifying phytoplankton at higher taxonomic resolutions when assessing their ecological and biogeochemical impacts (Luo et al. 2016; Lin et al. 2017; Rozema et al. 2017). As a result, the incorporation of routine molecular and quantitative imaging techniques for characterizing WAP phytoplankton dynamics has been identified as a high priority for regional monitoring programs (Henley et al. 2019). In this study, we assess WAP cryptophyte diversity and its drivers at a high taxonomic resolution, using a phylogenetic placement approach with a 5-year dataset of 18S rRNA gene sequences collected during the Palmer LTER regional research cruises.

3.3 Methods

3.3.1 Palmer LTER core measurements

Data for this study were collected over five years (2012 to 2016) during the Palmer LTER regional research cruises along the WAP, which were conducted aboard the ASRV *Laurence M. Gould* each austral summer month of January during the peak of the summer growth season. The Palmer LTER regional grid spans north to south along the WAP, and east to west from the coast to the continental slope (Figure 3.1b). The grid consists of sampling lines 100 km apart that are oriented perpendicular to the WAP coastline, with sampling stations located every 20 km. The grid is typically split into nine sub-regions, which span a broad along-shore (the north, south, and far south sub-regions), and cross-shore (the coast, shelf, and slope sub-regions) area of the WAP (Martinson et al. 2008).

Continuous underway measurements of surface (~5 m) temperature and salinity from the ship's surface seawater flow-through system were obtained from data files provided by the Marine Geoscience Data System formatted according to the Joint Global Ocean Flux Study specifications. Discrete seawater samples for macronutrients (phosphate, nitrate+nitrite, and silicate) and phytoplankton pigments, including chlorophyll-*a* (chl-*a*; a primary plant pigment used as a biomass index) and accessory pigments, specifically fucoxanthin and alloxanthin (fuco and allo, respectively; the primary diatom and cryptophyte chemotaxonomic pigments), were collected from Niskin bottles deployed at depth, or from the ship's surface seawater flow-through system. Samples for macronutrients were filtered through combusted 47 mm diameter Whatman GF/F glass fiber filters into new plastic 15 mL centrifuge tubes, frozen and stored at -20

°C, then measured by continuous flow analyzers according to Lorenzoni and Benway (2013) at the Lamont-Doherty Earth Observatory. Samples for phytoplankton pigments were filtered onto 25 mm diameter Whatman GF/F glass fiber filters and wrapped in foil. Filters for chl-*a* via fluorescence were frozen and stored at -80 °C, then measured according to Parsons et al. (1984) at either Palmer Station (2012 to 2015) or Rutgers University (2016). Filters for chl-*a* and accessory pigments via HPLC were flash frozen in liquid nitrogen, stored at -80 °C, then measured according to Kozlowski et al. (2011) at Rutgers University. Due to a freezer failure, HPLC data are not available for 2012.

Data were quality-controlled by excluding observations with values outside of realistic environmental ranges according to Brown et al. (2019), including temperature: -2 to 4 °C; salinity: 30 to 42; phosphate: 0 to 5 μmol L^{-1}; nitrate+nitrite: 0 to 50 μmol L^{-1}; silicate: 0 to 175 μmol L^{-1}; chl-*a*: 0 to 60 mg m^{-3}. For each sampling event, replicate macronutrient and phytoplankton pigment observations per depth were averaged, and surface averages were calculated by averaging any observations between 0 and 5 m. For each DNA sample (see below), corresponding surface values of temperature, salinity, macronutrients, and phytoplankton pigments were constructed by 1) averaging any surface temperature and salinity observations within 1 hour, and 2) averaging any surface averages of macronutrients and phytoplankton pigments within 1 day and 10 km, or if missing, 20 km (the half and full distance between sampling stations, respectively; Figure 3.1b).

3.3.2 DNA samples

Discrete seawater samples for DNA sequencing were collected from the ship's surface seawater flow-through system and were filtered onto 47 mm diameter Supor filters (0.45 μm pore size for years 2012 and 2013; 0.20 μm pore size for years 2014 to 2016). The filters had 1 mL of RNAlater added and were frozen and stored at -80 °C. Back in the lab, each filter was split in half (one half for the DNA analyses discussed here; one half for unrelated RNA analyses). DNA from the filters was then extracted and purified using Qiagen DNeasy Plant Mini kits after cell lysis by bead beating with 0.1 mm Zr beads in the AP1 lysis buffer. Small subunit 18S rRNA genes were amplified by PCR (annealing temperature of 60°C) using the V4 primer set *EukF* (5′-CCAGCASCYGCGGTAATTCC-3′) and *EukR* (5′-ACTTTCGTTCTTGAT-3′), which was modified from Stoek et al. (2010) for improved haptophyte coverage. Amplicon libraries were sequenced at the Duke University Institute for Genome Sciences and Policy using the Illumina MiSeq 300PE platform. For each amplicon library, assembly of paired-end reads was performed with *VSEARCH v2.3.4* (Rognes et al. 2016). Quality filtering and chimera checking of assembled reads was performed with *DADA2 v1.10.1* (Callahan et al. 2016). In total, 119 DNA samples were collected, but two were excluded due to low read counts (< 100), and two were excluded due to ambiguous time/location metadata, yielding 115 samples. Amplicon sequence variants (ASVs) (Callahan et al. 2017) were generated with *DADA2*, and ASVs were assigned taxonomy using the *assignTaxonomy* function (with a minimum boot strap confidence level of 50) and a *DADA2*-formatted Silva r132 reference database (Callahan 2018). Only cryptophyte

ASVs, defined as those classified as *Cryptomonadales* at the phylum level in this reference database, were included in our study.

3.3.3 Phylogenetic placement

The cryptophyte ASVs were further classified with a phylogenetic placement approach (Barbera et al. 2018). This method consists of placing query sequences onto a fixed reference tree using a likelihood-based algorithm (Barbera et al. 2018), which offers some advantages over other classification methods (Matsen et al. 2010). Here, we used all sequences classified as *Cryptophyceae* (the next highest relevant taxonomic level after *Eukaryota*) in the Silva r132 reference database (Quast et al. 2013), accessed on June 12, 2019, to generate the reference tree. At the time of analysis, 2723 *Cryptophyceae* sequences were available in the Silva r132 reference database. Reference sequences were aligned with *Infernal* against the RFAM covariance model for 18S rRNA (Nawrocki and Eddy 2013), and were de-duplicated with *seqmagick* (https://fhcrc.github.io/seqmagick/), leaving 2615 unique reference sequences. These reference sequences were used to build the reference tree with *RAxML v8* (Stamatakis 2014) using the GTRGAMMA model. Phylogenetic placement of the cryptophyte ASVs on the reference tree was performed with *EPA-ng* (Barbera et al. 2018). Edge distance between placement locations (EDPL) was calculated with *GUPPY* (Matsen et al. 2010). The output of the phylogenetic placement consisted of the reference tree edge to which each cryptophyte ASV was placed, and an assessment of the placement uncertainty, including EDPL and percent identity (%ID) values, where lower EDPL and higher %ID indicates lower uncertainty.

Reference tree edges (points of placement) are either terminal or internal edges. Terminal edges are defined by a unique full-length 18S rRNA gene, while internal edges represent clades. Placement to an internal edge indicates that there was insufficient phylogenetic information available for placement at a terminal edge. In that case, the taxonomy of the query sequence is considered to be the lowest consensus ranking for all reference sequences belonging to the clade. Cryptophyte taxa were defined as reference tree edges to which cryptophyte ASVs were placed. For each DNA sample, 1) the read count of each cryptophyte taxon was calculated as the sum of the read counts of its corresponding cryptophyte ASVs, 2) the percentage of the cryptophyte community of each cryptophyte ASV and taxon (i.e. "ASV or taxon percentage") was calculated by dividing each cryptophyte ASV or taxon read count by the number of crytophyte reads, and multiplying by 100, and 3) the cryptophyte percentage of the overall eukaryotic community (i.e. "cryptophyte percentage") was calculated by dividing the number of cryptophyte reads by the number of 18S reads, and multiplying by 100. The cryptophyte ASVs, taxa, and average ASV and taxon percentages are summarized in Supplementary Table 3.1.

3.3.4 Seascape units

The corresponding physicochemical oceanographic conditions of the DNA samples were contextualized using the seascape units (SUs) defined by Bowman et al. (2018). Briefly, Bowman et al. (2018) trained a self-organizing map (SOM) on a multi-decadal dataset of temperature, salinity, macronutrients, and chl-*a* collected by the Palmer LTER program along the WAP. The SOM units were further segmented using k-

means clustering to generate eight clusters, i.e. SUs, each defining a distinct parameter space (see Table 1 of Bowman et al. (2018) for a description of the physicochemical attributes of the SUs). The output of this segmentation is a classification model that can be used to predict the SUs of new data. While additional oceanographic variables may also be relevant, the SUs represent an efficient and comprehensive means to simultaneously characterize both physical and ecological oceanographic conditions. Here, we determined the SU of each DNA sample using the corresponding surface values of temperature, salinity, macronutrients, and chl-*a* via fluorescence with the *map* function in the R package *kohonen* (Wehrens and Kruisselbrink 2018).

3.4 Results

3.4.1 Oceanographic context

During each of the five study years (2012 to 2016), DNA samples were collected over a broad along- and cross-shore area that was representative of the spatial extent of the respective Palmer LTER regional research cruise along the WAP (Figure 3.1b). In all years, the north and south sub-regions were sampled, and with the exception of 2016 (due to high sea ice concentrations), the far south sub-region was as well. Additionally, in all years, the coast, shelf, and slope sub-regions were sampled. In total, six of the eight SUs defined by Bowman et al. (2018) were associated with the DNA samples, including SU1, SU2, SU3, SU5, SU6, and SU8 (Figure 3.2). The primary SUs represented were SU1, SU6, and SU8, which accounted for 29%, 35%, and 29% of the samples, respectively. These SUs are frequently observed in the WAP surface ocean (Bowman et al. 2018). The

less represented SUs (SU2, SU3, and SU5), and those not represented at all (SU4 and SU7), are not frequently observed in the WAP upper surface ocean.

3.4.2 Cryptophyte ASVs and taxa

In total, 94 cryptophyte ASVs were identified in the 18S rRNA gene amplicon libraries (Supplementary Table 3.1). However, only two ASVs (henceforth ASV1 and ASV2) contributed substantially to the cryptophyte community, together always comprising > 90% of the cryptophyte reads (except for one sample). Specifically, ASV1 was the primary ASV (ASV percentage always > 70%; average ASV percentage of 91%), followed by ASV2 (average ASV percentage of 4%). All the other ASVs (ASV3 to ASV94) did not reach an average ASV percentage of 1%. Phylogenetic placement of the cryptophyte ASVs onto the reference tree yielded 25 distinct points of placement, i.e. cryptophyte taxa (Figure 3.3; Supplementary Table 3.1). However, only two taxa (henceforth TAX1 and TAX2) contributed substantially to the cryptophyte community, together always comprising > 98% of the cryptophyte reads. Specifically, TAX1 was the primary taxon (taxon percentage always > 70%; average taxon percentage of 96%), followed by TAX2 (average taxon percentage of 4%). All the other taxa did not reach an average taxon percentage of 1%. TAX1 consisted of 58 ASVs, including ASV1. This taxon corresponded to an internal node of the reference tree (Edge #5196), which was comprised of both an uncultured *Geminigera* species from the South Atlantic (FJ032651) and a *G. cryophila* strain from Ace Lake, Antarctica (HQ111513). TAX2 consisted of just ASV2. This taxon corresponded to a terminal node of the reference tree (Edge #5226), which was a *G. cryophila* strain from an unspecified location (AB058366).

Notably, strain AB058366 was identical after alignment to the NCMA *G. cryophila* strain from McMurdo Sound, Antarctica (CCMP2564), which was not included in the Silva r132 reference database (Quast et al. 2013). Placements to both Edge #5196 and #5226 were of high confidence, as indicated by both low EDPLs and high %IDs (Edge #5196: EDPL = $3x10^{-3}$, %ID = 93 to 98%; Edge #5226: EDPL = $2x10^{-4}$, %ID = 100%).

3.4.3 Drivers of cryptophyte diversity

There was a clear inverse relationship between the cryptophyte community percentage of TAX1 and TAX2, the two major cryptophyte taxa (Figure 3.3). Specifically, while TAX1 was consistently dominant (always > 70% of the cryptophyte community), a decrease in the percentage of TAX1 coincided with an increase in the percentage of TAX2. This shift in cryptophyte community composition was most substantial when cryptophytes were a small percentage (< 10%) of the overall eukaryotic community (Figure 3.4). To identify additional physicochemical oceanographic conditions associated with the shift between TAX1 and TAX2, the DNA samples were separated into two groups (henceforth GRP1 and GRP2), which were based on the TAX1 percentage of the cryptophyte community. Specifically, GRP1 was defined as where TAX1 > 95%, and GRP2 was defined as where TAX1 < 95% (see the black horizontal dashed line in Figure 3.4).

To assess differences in the SU composition associated with GRP1 and GRP2, a chi-square test was performed. A single bin was used for the SUs that were less represented (SU2, SU3, and SU5), or not represented at all (SU4 and SU7). There was a significant difference in the SU relative frequencies of GRP1 and GRP2 ($\chi^2 = 11.5$, $p =$

0.009, df = 3; Figure 3.5). Specifically, while both GRP1 and GRP2 primarily occurred in conditions characterized as SU1, SU6, and SU8 (93% and 96% of samples, respectively), GRP1 was mainly associated with SU1 and SU8 (together 66% of samples) and GRP2 was mainly associated with SU6 (62% of samples). Importantly, relative to both SU1 and SU8, SU6 is characterized by distinct physicochemical oceanographic conditions, including lower temperature, salinity, phosphate, and nitrate+nitrite, and higher chl-*a* (see Table 1 of Bowman et al. (2018)). To assess differences in phytoplankton accessory pigments associated with GRP1 and GRP2, two-tailed Welch's t-tests were performed. Relative to GRP1, GRP2 was associated with a significantly lower allo/chl-*a* via HPLC ratio and a significantly higher fuco/chl-*a* via HPLC ratio ($t = 7.0$, $p < 0.001$, df = 40.2 and $t = -7.6$, $p < 0.001$, df = 60.7, respectively; Figure 3.6). The phytoplankton pigment ratios were $\log_{10}$-transformed prior to analysis to ensure normality. A single fuco/chl-*a* ratio was excluded due to a fuco value of 0 mg m^{-3}.

3.5 Discussion

This study indicates that there is a low diversity of cryptophytes along the WAP. As with diatoms, cryptophytes are a key phytoplankton group in the region (Garibotti et al. 2003; Schofield et al. 2017). In particular, of the 94 cryptophyte ASVs identified in the DNA samples, just two (ASV1 and ASV2) contribute substantially to the cryptophyte community, together combining to essentially always comprise > 90% of cryptophyte reads (Supplementary Table 3.1). Furthermore, of the 25 cryptophyte taxa identified by phylogenetic placement of the cryptophyte ASVs, just two (TAX1 and TAX2) contribute substantially to the cryptophyte community, together combining to always comprise >

98% of the cryptophyte reads (Figure 3.3; Supplementary Table 3.1). Both TAX1 and TAX2, which consist of ASV1 (and 57 other ASVs) and ASV2, respectively, belong to the cryptophyte genus *Geminigera*. For comparison, WAP diatoms have a higher diversity than cryptophytes (Yajuan Lin unpublished data).

The primary WAP cryptophyte taxon is TAX1, which always comprises > 70% of the cryptophyte reads (average taxon percentage of 96%; Figure 3.3, Supplementary Table 3.1). This taxon closely matches a *G. cryophila* strain from Ace Lake, Antarctica (HQ111513). The DNA samples used for this study were collected over a broad temporal (five years of sampling) and spatial (along- and cross-shore sub-regions consistently sampled; Figure 3.1b) extent that sufficiently covered the WAP marine ecosystem (six of eight SUs were represented; Figure 3.2). This indicates that TAX1 is capable of dominating the WAP cryptophyte community over a wide range of oceanographic conditions. The secondary WAP cryptophyte taxon is TAX2 (average taxon percentage of 4%; Figure 3.3, Supplementary Table 3.1), which closely matches a *G. cryophila* strain from McMurdo Sound, Antarctica (CCMP2564).

While certainly intriguing, it is not unexpected that the primary WAP cryptophyte taxon closely matches a cryptophyte strain from Ace Lake. Located in the Vestfold Hills of East Antarctica < 200 m from the nearest marine inlet, Ace Lake is a meromictic (permanently stratified) saline (mixolimnion salinity ranges ~11 to 30) lake that only recently (~5,000 years ago) became fully separated from the ocean (Laybourn-Parry and Bell 2014). The fact that TAX1 closely matches the Ace Lake *G. cryophila* strain is consistent with observations from around Antarctica (including the WAP) that coastal marine cryptophytes display a tolerance for lower salinities (Moline et al. 2004; Mendes

et al. 2013; Schofield et al. 2017). Additionally, the Ace Lake *G. cryophila* strain has been observed to contribute substantially to the coastal phytoplankton communities of King George Island in the northern WAP (Luo et al. 2016). Interestingly, while both TAX1 and TAX2 belong to the cryptophyte genus *Geminigera*, the few previous WAP cryptophyte blooms observed via microscopy were identified as belonging either to the cryptophyte genera *Cryptomonas* or *Teleaulax* (Mascioni et al. 2019 and references therein). It should be noted that both the *Cryptomonas* and *Teleaulax* genera were represented in the DADA2-formatted Silva r132 reference database used to assign taxonomy to ASVs (Callahan 2018), and the Silva r132 *Cryptophyceae* reference database used for the phylogenetic placement of cryptophyte ASVs (Quast et al. 2013). This emphasizes the need for future studies pairing molecular and microscopy techniques to identify WAP cryptophytes, and a focus on adding regional sequences to reference databases.

Variability in WAP cryptophyte community composition is primarily associated with changes in the cryptophyte community percentage of the two major cryptophyte taxa. Specifically, a decrease in the TAX1 percentage coincides with an increase in the TAX2 percentage (Figure 3.3). Separating the DNA samples into two groups (GRP1 and GRP2) based on the TAX1 percentage (GRP1: TAX1 > 95%; GRP2: TAX1 < 95%) indicates that this shift in cryptophyte community composition is related to changes in oceanographic physicochemical conditions. In particular, relative to GRP1, GRP2 is primarily associated with SU6 rather than SU1 and SU8 (Figure 3.5). Therefore, the shift to a lower (higher) TAX1 (TAX2) percentage coincides with lower temperature, salinity, and macronutrients, and higher phytoplankton biomass. Additionally, relative to GRP1,

GRP2 is associated with a lower cryptophyte percentage (Figure 3.4 and 3.6a) and a higher diatom percentage (Figure 3.6b). Therefore, the shift to a lower (higher) TAX1 (TAX2) percentage also coincides with a shift in overall phytoplankton community composition from cryptophytes to diatoms. These results are consistent with previous observations that relative to cryptophyte assemblages, diatom assemblages along the WAP are associated with lower macronutrients and higher phytoplankton biomass (Brown et al. 2019), and that these two phytoplankton groups do not typically co-occur (Schofield et al. 2017). Ultimately, this study indicates that the primary WAP cryptophyte taxon contributes most substantially to the cryptophyte community during less productive conditions when cryptophytes are a larger percentage of the overall phytoplankton community. The primary taxon contributes less to the cryptophyte community (and is replaced by the secondary taxon) during more productive conditions when cryptophytes are a smaller percentage of the overall phytoplankton community (and have been replaced by diatoms).

The WAP marine ecosystem is structured by complex atmosphere-ice-ocean dynamics (Ducklow et al. 2013), and there is uncertainty in how the region will respond to continued global change (Henley et al. 2019). For example, although the SAM has recently trended positive (Marshall 2003), it is unclear how opposing effects of the ozone hole recovery and increased greenhouse gas concentrations will ultimately impact its phase and seasonality (Turner et al. 2014). Additionally, it has been observed that long-term trends have slowed in atmospheric warming (Turner et al. 2016) and sea ice decline (Schofield et al. 2018). However, these trends are still significant since the mid-20th century (Henley et al. 2019), and the trends in oceanic warming and glacial retreat show

no evidence of slowing (Cook et al. 2016). Therefore, it is generally predicted that the WAP will continue to warm and melt.

The WAP is currently characterized by a meridional climate gradient. Specifically, while the mid/southern WAP remains a dry polar system, the northern WAP has been altered such that it now represents a more maritime sub-polar system (Ducklow et al. 2013). In the north, warming, glacial retreat, and sea ice decline have driven bottom effects on the WAP marine ecosystem, resulting in declines in phytoplankton biomass and cell size, a community shift from diatoms to cryptophytes, and an increasingly microbially-dominated food web (Moline et al. 2004; Montes-Hugo et al. 2009; Sailley et al. 2013; Brown et al. 2019). It is predicted that these northern conditions will expand as the effects of climate change progress southward along the WAP (Henley et al. 2019). These changes to the WAP marine ecosystem could reinforce the substantial contribution of the primary cryptophyte taxon to the regional cryptophyte community, resulting in continued low regional cryptophyte diversity, given the association of this taxon with less productive conditions and the occurrence of cryptophytes. Future studies should focus on assessing WAP phytoplankton diversity at a high taxonomic resolution, with a particular emphasis on characterizing the ecology of these two major cryptophyte taxa in the context of regional environmental change.

3.6 Figures

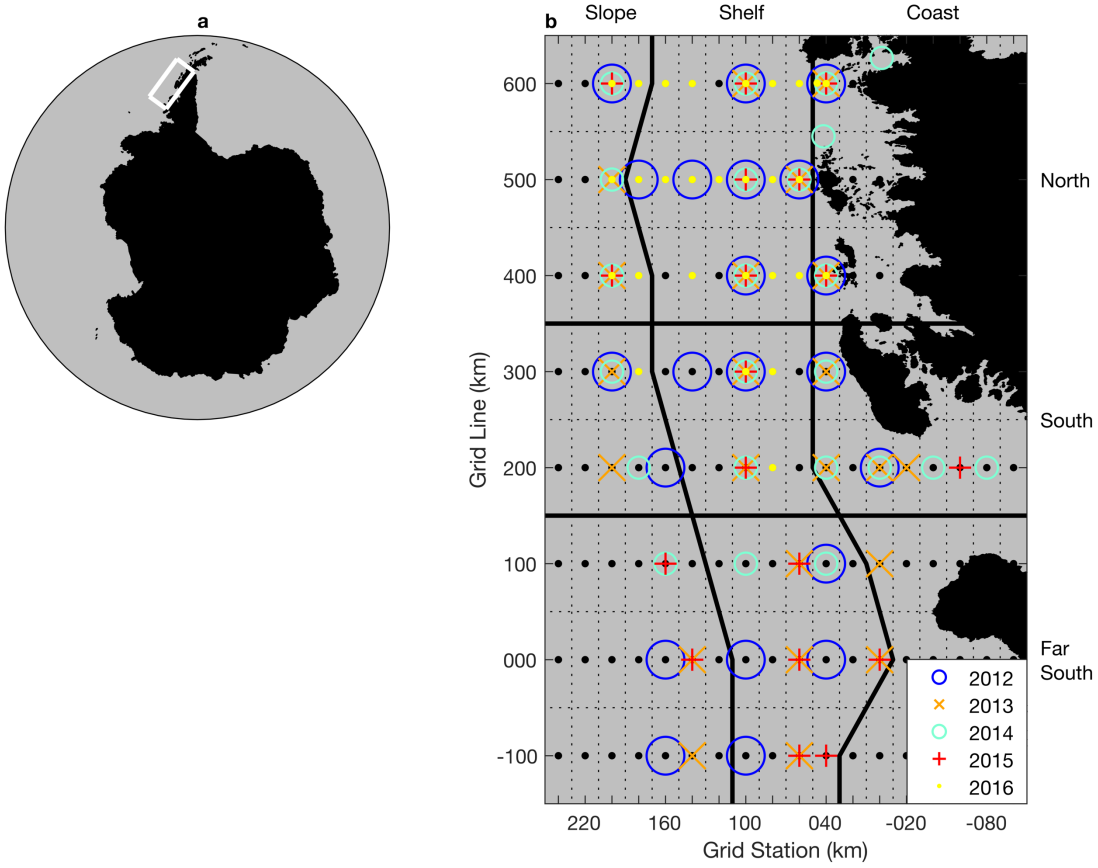

Figure 3.1. Map of the study area, including: **a** the Antarctic continent and **b** the Palmer LTER regional grid along the West Antarctic Peninsula (boxed region in **a**) with the locations of the DNA samples. The black dots and black dotted lines indicate the grid sampling stations. The black solid lines indicate along- and cross-shore sub-regions of the grid, which span the north, south, and far south, and coast, shelf, and slope.

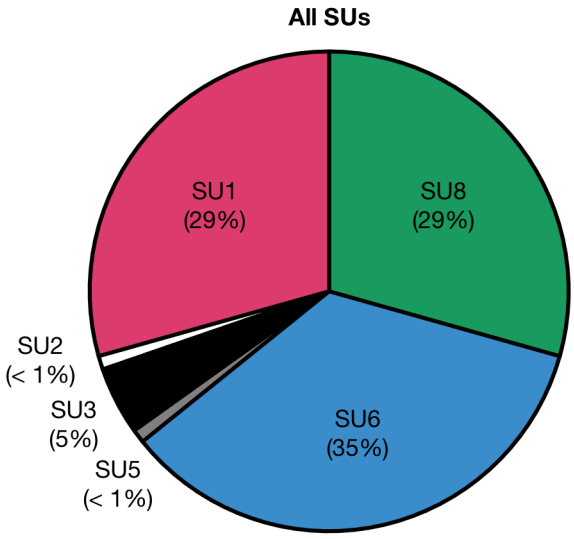

Figure 3.2. Seascape units (SUs) represented by the full DNA sample dataset; n = 109.

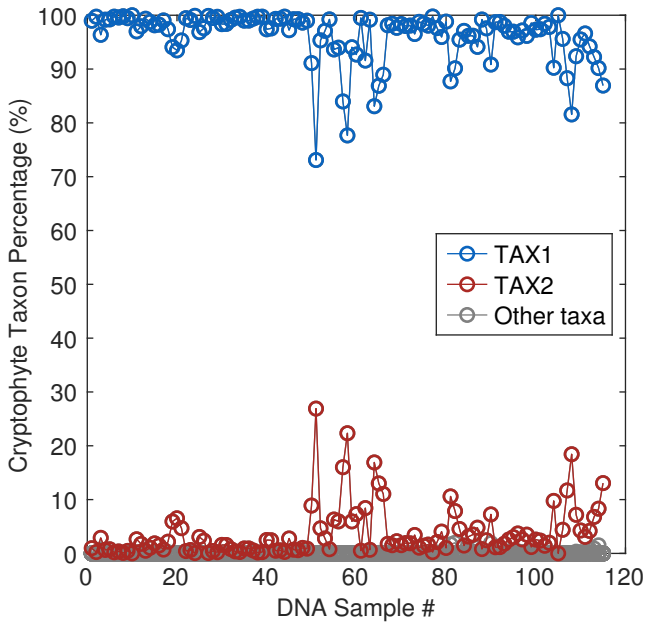

Figure 3.3. Percentage of the cryptophyte community of the two primary cryptophyte taxa (TAX1 and TAX2), and all other taxa, for each of the DNA samples.

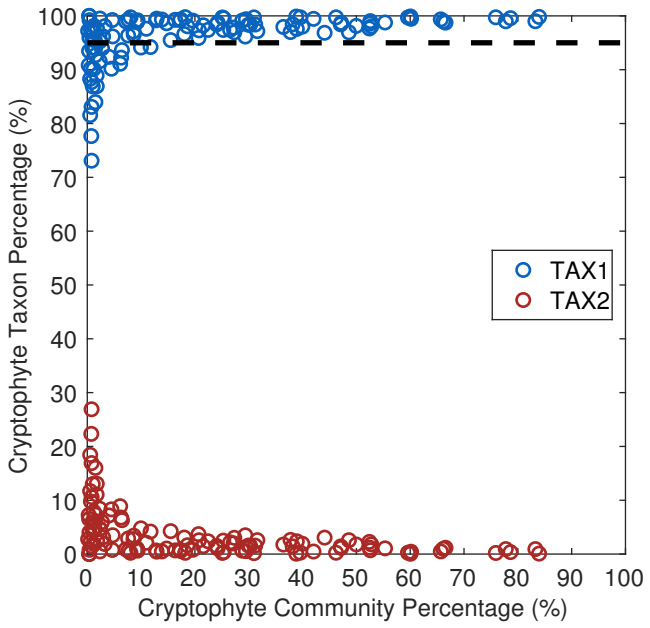

Figure 3.4. Percentage of the cryptophyte community of the two primary cryptophyte taxa (TAX1 and TAX2) plotted versus the cryptophyte percentage of the overall eukaryotic community. The black horizontal dashed line indicates a cryptophyte taxon percentage of 95%.

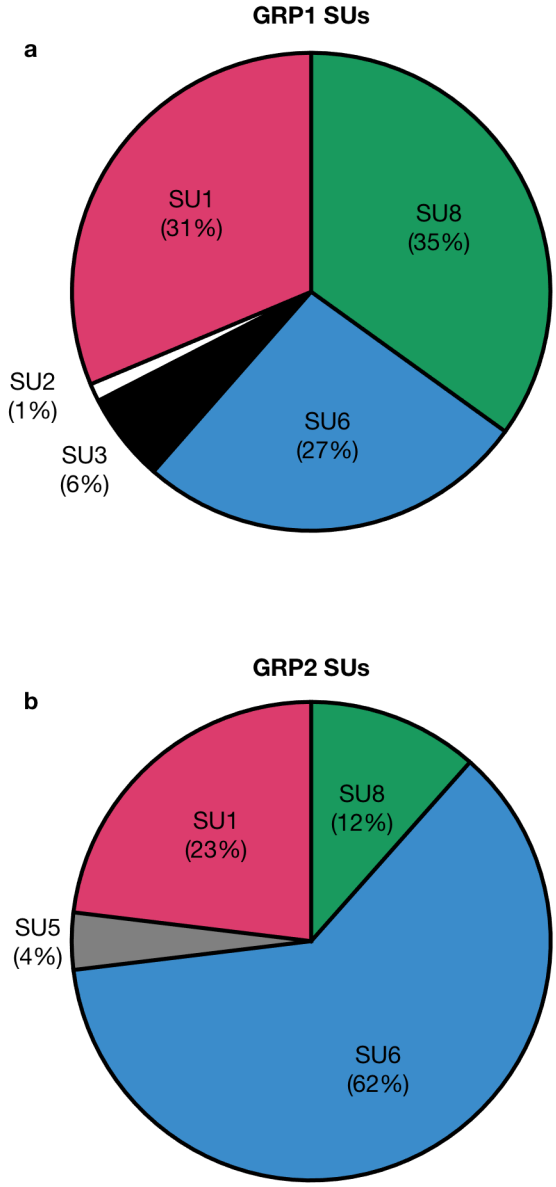

Figure 3.5. Seascape units (SUs) represented by DNA samples classified as either of the two groups (GRP1 and GRP2), which were defined based on the TAX1 percentage of the cryptophyte community: **a** GRP1 (TAX1 > 95%), $n = 83$; **b** GRP2 (TAX1 < 95%), $n = 26$.

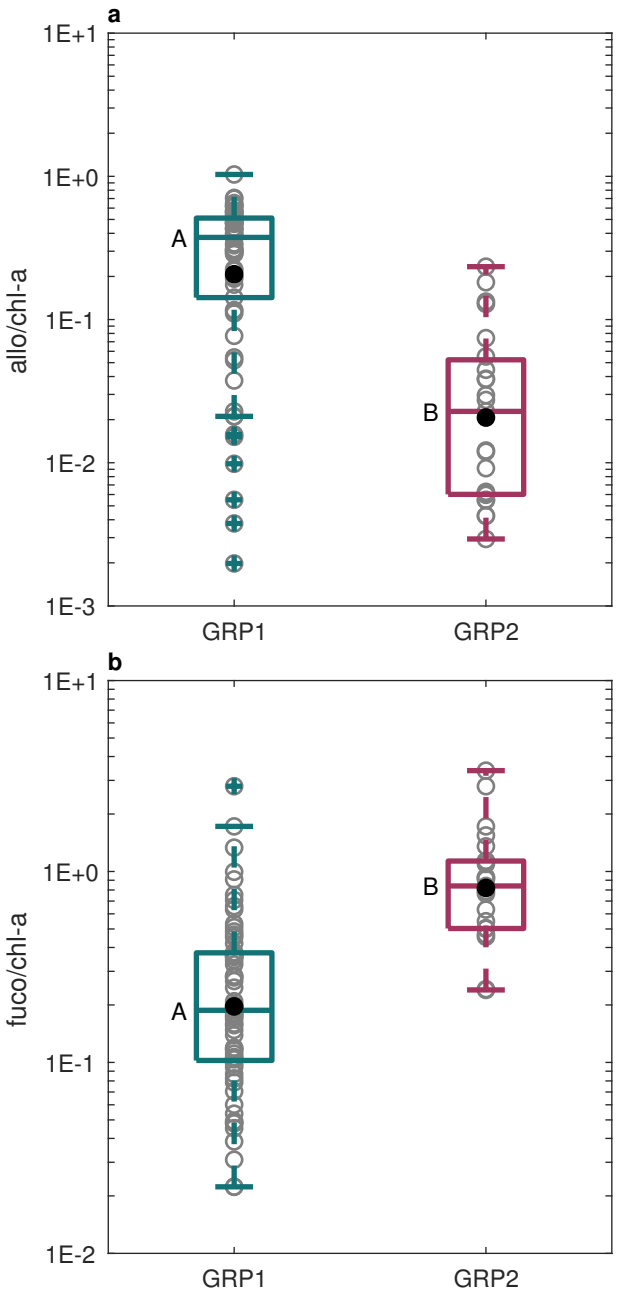

Figure 3.6. The ratio to chlorophyll-a (chl-*a*) via HPLC of: **a** alloxanthin (allo) and **b** fucoxanthin (fuco) for DNA samples classified as either of the two groups (GRP1 and GRP2), which were defined based on the TAX1 percentage of the cryptophyte community: **a** GRP1 (TAX1 > 95%); **b** GRP2 (TAX1 < 95%). The horizontal lines indicate the median and 25th and 75th percentiles, and the black circles indicate the mean. The gray circles indicate individual values. The whiskers extend to values not considered as outliers, with outliers indicated by colored pluses. The presence of a difference among groups was determined with Welch's t-tests, and the capital letters indicate statistical groupings at $\alpha = 0.05$.

3.7 Supplementary tables

Supplementary Table 3.1. Summary of cryptophyte ASVs and taxa. Edge # is the phylogenetic placement reference tree edges (points of placement) of the cryptophyte ASVs, and are interpreted as cryptophyte taxa. Edge #5196 and Edge #5226 correspond to the cryptophyte taxa TAX1 and TAX2, respectively (highlighted in gray). 18SASV_1 and 18SASV_58 correspond to the cryptophyte ASVs ASV1 and ASV2, respectively (in red font). The ASV and taxon % average is the average cryptophyte ASV and taxon percentage, respectively.

Edge #	ASV	ASV % Avg.	Taxon % Avg.
Edge_0055	18SASV_1469	0.00	0.00
Edge_0056	18SASV_1365	0.00	0.00
Edge_0057	18SASV_1765	0.00	0.00
Edge_0064	18SASV_1163	0.00	0.00
Edge_0173	18SASV_992	0.00	0.00
Edge_0221	18SASV_1862	0.00	0.00
Edge_2701	18SASV_1363	0.00	0.00
Edge_2912	18SASV_2191	0.00	0.00
Edge_3854	18SASV_1998	0.00	0.00
Edge_3855	18SASV_292	0.04	0.04
Edge_3855	18SASV_1006	0.00	0.04
Edge_3856	18SASV_432	0.01	0.01
Edge_3856	18SASV_1164	0.00	0.01
Edge_4381	18SASV_1946	0.00	0.00
Edge_4383	18SASV_2325	0.00	0.00
Edge_4386	18SASV_2115	0.00	0.00
Edge_4553	18SASV_1541	0.00	0.00
Edge_4587	18SASV_1804	0.00	0.00
Edge_5170	18SASV_2426	0.00	0.00
Edge_5193	18SASV_1377	0.00	0.00
Edge_5193	18SASV_913	0.00	0.00
Edge_5193	18SASV_934	0.00	0.00
Edge_5193	18SASV_1258	0.00	0.00
Edge_5193	18SASV_847	0.00	0.00
Edge_5194	18SASV_1740	0.00	0.00
Edge_5194	18SASV_2114	0.00	0.00
Edge_5195	18SASV_994	0.00	0.00
Edge_5196	18SASV_854	0.00	96.19
Edge_5196	18SASV_871	0.00	96.19
Edge_5196	18SASV_688	0.00	96.19
Edge_5196	18SASV_511	0.00	96.19
Edge_5196	18SASV_277	0.02	96.19

Edge #	ASV	ASV % Avg.	Taxon % Avg.
Edge_5196	18SASV_117	0.17	96.19
Edge_5196	18SASV_1059	0.00	96.19
Edge_5196	18SASV_75	0.43	96.19
Edge_5196	18SASV_1395	0.00	96.19
Edge_5196	18SASV_1638	0.00	96.19
Edge_5196	18SASV_754	0.00	96.19
Edge_5196	18SASV_92	0.58	96.19
Edge_5196	18SASV_189	0.07	96.19
Edge_5196	18SASV_156	0.11	96.19
Edge_5196	18SASV_1220	0.00	96.19
Edge_5196	18SASV_235	0.12	96.19
Edge_5196	18SASV_1181	0.00	96.19
Edge_5196	18SASV_116	0.33	96.19
Edge_5196	18SASV_1854	0.00	96.19
Edge_5196	18SASV_93	0.45	96.19
Edge_5196	18SASV_339	0.01	96.19
Edge_5196	18SASV_1152	0.00	96.19
Edge_5196	18SASV_1	91.34	96.19
Edge_5196	18SASV_1035	0.00	96.19
Edge_5196	18SASV_154	0.19	96.19
Edge_5196	18SASV_910	0.00	96.19
Edge_5196	18SASV_1211	0.00	96.19
Edge_5196	18SASV_1064	0.05	96.19
Edge_5196	18SASV_264	0.12	96.19
Edge_5196	18SASV_221	0.11	96.19
Edge_5196	18SASV_1186	0.00	96.19
Edge_5196	18SASV_993	0.00	96.19
Edge_5196	18SASV_1122	0.00	96.19
Edge_5196	18SASV_989	0.00	96.19
Edge_5196	18SASV_355	0.03	96.19
Edge_5196	18SASV_1001	0.00	96.19
Edge_5196	18SASV_519	0.00	96.19
Edge_5196	18SASV_957	0.00	96.19
Edge_5196	18SASV_443	0.01	96.19
Edge_5196	18SASV_118	0.24	96.19
Edge_5196	18SASV_680	0.00	96.19
Edge_5196	18SASV_232	0.05	96.19
Edge_5196	18SASV_575	0.03	96.19
Edge_5196	18SASV_183	0.10	96.19
Edge_5196	18SASV_1482	0.00	96.19
Edge_5196	18SASV_776	0.00	96.19
Edge_5196	18SASV_124	0.60	96.19
Edge_5196	18SASV_950	0.00	96.19
Edge_5196	18SASV_187	0.09	96.19

Edge #	ASV	ASV % Avg.	Taxon % Avg.
Edge_5196	18SASV_218	0.13	96.19
Edge_5196	18SASV_112	0.38	96.19
Edge_5196	18SASV_230	0.09	96.19
Edge_5196	18SASV_214	0.03	96.19
Edge_5196	18SASV_195	0.13	96.19
Edge_5196	18SASV_186	0.09	96.19
Edge_5196	18SASV_885	0.00	96.19
Edge_5196	18SASV_1054	0.00	96.19
Edge_5196	18SASV_213	0.05	96.19
Edge_5197	18SASV_1012	0.00	0.01
Edge_5197	18SASV_1328	0.00	0.01
Edge_5197	18SASV_1234	0.00	0.01
Edge_5197	18SASV_1223	0.01	0.01
Edge_5211	18SASV_1842	0.00	0.00
Edge_5224	18SASV_1027	0.00	0.14
Edge_5224	18SASV_1202	0.00	0.14
Edge_5224	18SASV_255	0.14	0.14
Edge_5226	18SASV_58	3.60	3.60

4 Meltwater chemistry of a receding West Antarctic Peninsula glacier

4.1 Abstract

The West Antarctic Peninsula (WAP) has experienced substantial environmental change, including rapid atmospheric and oceanic warming that has driven considerable glacial retreat. Although glacial meltwater discharge has increased along the WAP, there is little known about its chemistry, and how it might impact the coastal ocean. Here, as part of Palmer Long-Term Ecological Research program, we examine the chemical composition (trace metals, macronutrients, and stable oxygen isotopes of water, i.e. $\delta^{18}O$) and discharge dynamics of two WAP glacial meltwater streams originating from the Marr Glacier adjacent to Palmer Station on Anvers Island during the 2016-17 austral summer. Although there are substantial differences between the two streams, including their physical characteristics and discharge dynamics, there are common features in their chemistry. Both streams have a seasonal median $\delta^{18}O$ value of about -11.90‰, which provides an important new constraint for distinguishing and quantifying WAP meteoric water in regional isotopic endmember analyses. Additionally, with the exception of silicate and Ni, both streams have nearly equivalent or higher seasonal median macronutrient (phosphate and nitrate) and trace metal (especially Fe, Cu, Mn, and Zn) concentrations than the corresponding coastal seawater. This indicates that WAP glacial meltwater can be a source of these elements to the coastal ocean. There is a general pattern in both streams of a positive correlation between stream discharge and phosphate

and Fe concentration, and a negative correlation for other elements. This indicates a source of phosphate and Fe during periods of high glacial meltwater flow, while other elements are diluted. The high Cu in the glacial meltwater could have important implications for coastal phytoplankton dynamics.

4.2 Introduction

The West Antarctic Peninsula (WAP; Figure 4.1a) is a productive marine ecosystem within the Sea Ice Zone of the Southern Ocean (Ducklow et al. 2007). Here, meltwater from winter sea ice and glaciers stabilizes the surface ocean during spring and summer, promoting large coastal phytoplankton blooms, which supports krill populations and top predators such as penguins and whales (Friedlaender et al. 2006, Vernet et al. 2008, Saba et al. 2014, Steinberg et al. 2015). This region is also notable for the substantial environmental changes observed since the mid-20th century, which include rapid warming and melting. The WAP is the site of one the largest increases in winter atmospheric temperatures globally (Vaughan et al. 2003), large positive trends in oceanic temperatures (Meredith and King 2005, Martinson et al. 2008), and a reduction in the length of the sea ice season by three months (Stammerjohn et al. 2008a). Furthermore, the atmospheric and oceanic warming along the WAP has driven substantial glacial retreat (Cook et al. 2016). These environmental changes to the WAP are now impacting the marine food web across all trophic levels (Schofield et al. 2010, Henley et al. 2019).

It is expected that glacial runoff to the WAP coastal ocean will increase with continued warming and glacial retreat (Vaughan 2006). Recent studies in the region have distinguished and quantified meteoric water (glacial meltwater plus precipitation) and sea

ice melt using stable oxygen isotopes in water (i.e. $\delta^{18}O$) to assess changes in the oceanic freshwater budget (Meredith et al. 2010, Meredith et al. 2017). However, there has been relatively little focus on determining the chemical composition of glacial meltwater along the WAP, and this has been deemed a research priority (Hodson et al. 2010). This gap is especially relevant for trace metals and macronutrients that could impact coastal phytoplankton communities. Specifically, much of the Southern Ocean is considered to be iron-limited (Martin et al. 1990), and it has been hypothesized that with typically replete macronutrients (Kim et al. 2016), iron could control primary production in offshore waters along the WAP (Garibotti et al. 2003, Smith et al. 2008, Huang et al. 2012, Annett et al. 2017, Schofield et al. 2018, Sherrell et al. 2018). It has also been hypothesized that variability in WAP coastal phytoplankton community composition could be associated with a glacial meltwater constituent (e.g. a trace metal), in particular shifts between diatoms and cryptophytes, two primary regional phytoplankton groups with distinct roles in the WAP marine food web (Saba et al. 2014) and biogeochemistry (Brown et al. 2019). It has been demonstrated elsewhere that glacial meltwater can be a source of iron to coastal oceans (Hawkings et al. 2014), and therefore it is important to assess the chemical composition of WAP glacial meltwater, especially regarding iron and other bioactive elements.

There are limited measurements of the chemical composition of glacial runoff along the WAP, especially from the mid/southern WAP, which has been observed for thirty years by the Palmer Long-Term Ecological Research (LTER) program, and others (Henley et al. 2019). On islands off the northern WAP, there have been direct measurements of iron and other solutes in glacial runoff (Hodson 2006, Hodson et al.

2010, Hodson et al. 2017), direct measurements of iron in icebergs (Raiswell et al. 2008), and estimates of trace and rare earth elements in glacial meltwater based on coastal seawater concentrations sampled over a glacial meltwater-driven salinity gradient (Kim et al. 2015). Along the mid/southern WAP, there has primarily been a focus on assessing seawater trace metal concentrations (Annett et al. 2015, Annett et al. 2017, Bown et al. 2017, Sherrell et al. 2018), and just one observation of glacial meltwater iron and manganese has been reported (Annett et al. 2017). In this study, we assess the chemical composition (trace metals, macronutrients, and $\delta^{18}O$) and discharge dynamics of two glacial meltwater streams originating from the Marr Glacier on Anvers Island over an austral summer. This work was conducted as part of the Palmer LTER, and to the best of our knowledge, the glacial meltwater dataset presented here is the first of its kind for the mid/southern WAP.

4.3 Methods

4.3.1 Sampling sites

Two glacial meltwater streams, Stream 1 and 2, located north of Palmer Station on Anvers Island and flowing from the Marr Glacier into Arthur Harbor (Figure 4.1b; Supplementary Table 4.1) were sampled during the 2016-17 austral summer. Stream 1 is located further from Palmer Station (~900 m), is shorter (~50 m), more turbid (visibly discolored), and flows over finer glacial till at a steeper descent. Stream 2 is located closer to Palmer Station (~650 m), is longer (~200 m), less turbid (visibly clear), and flows over coarser glacial till at a shallower descent. Both streams were identified during the previous austral summer (2015-16), which suggests that they are perennial features.

For each stream, the sampling site was at the coastline. Samples were collected for both proximal coastal seawater and stream glacial meltwater. The coastal seawater was collected from shore, near the stream mouth. The glacial meltwater was collected just uphill from where the stream entered the ocean, as close to shore as possible (Figure 4.1; Supplementary Table 4.1). Stream sampling occurred from December 24, 2016 to March 9, 2017 (concurrent with the Palmer LTER field season), with both streams visited every 1 to 3 weeks, for a total of seven sampling events per stream. Sampling events for both streams occurred in the afternoon on either the same day, separated by at most two hours, or on different days, separated by at most one week (Table 4.1).

4.3.2 Sampling procedures

During each stream sampling event, the coastal seawater was sampled first. A trace metal clean (TMC; acid-cleaned with ultrapure hydrochloric acid (Optima grade, Fisher Scientific) and rinsed three times with high-purity deionized water) 1 L low-density polyethylene (LDPE) sampling bottle was lowered with a gloved (pre-rinsed, clean room nitrile) hand inverted into the surface ocean, reinverted, and allowed to fill from ~10 cm below the sea surface. In this way, sampling avoided the sea surface microlayer. Separate samples for filtered trace metal duplicates were then drawn from the TMC 1 L LDPE sampling bottle with a TMC 60 mL plastic syringe. These samples were filtered with a TMC 30 mm diameter, 0.45 μm pore size polyethersulfone syringe filter into TMC 60 mL LDPE bottles. Separate samples for macronutrients and for stable oxygen isotopes of water were also drawn from the TMC 1 L LDPE sampling bottle with the same TMC 60 mL plastic syringe. These samples were filtered with a TMC 30 mm

diameter, 0.45 μm pore size polyethersulfone syringe filter into a 15 mL polystyrene centrifuge tube, and a 50 mL glass serum bottle sealed with a stopper and aluminum crimp, respectively. Care was taken to gently homogenize the TMC 1 L LDPE sampling bottle between samples. The above steps were then repeated for the glacial meltwater, using a new TMC 1 L LDPE sampling bottle to sample the stream. At the conclusion of each stream sampling event, a discrete measurement of stream discharge (L s^{-1}) was made. This was performed for Stream 1 by determining the time required for the entire stream to fill a known volume, and for Stream 2 by determining the time required for a buoyant, 40 mm diameter plastic ball to travel a portion of the stream of known length and cross-sectional area. Each stream sampling event typically took 2.5 hours to complete (Table 4.1). At the end of the field season, three separate samples for glacial ice oxygen isotopes were collected on different days (Table 4.1). Briefly, following glacial calving events, pieces of glacial ice were collected from Arthur Harbor from a small vessel and stored in a clean plastic bag. Back in the lab, the glacial ice was allowed to melt at room temperature (taking care to prevent evaporation), and the meltwater was then poured directly into a 50 mL glass serum bottle sealed with a stopper and aluminum crimp. After all sampling events, the trace metal samples were stored in the dark chilled at +4°C, the macronutrient samples frozen at -80°C (later at -20°C), and the oxygen isotope samples in the dark at room temperature (later chilled at +4°C), until analysis. These conditions were maintained during shipment to analytical laboratories in the USA and UK.

4.3.3 Trace metals

The meltwater and coastal seawater filtered trace metal samples were analyzed for the determination of dissolved Fe, Zn, Ni, Cu, Cd, Pb, and Mn (all nM). Analyses were carried out at the Rutgers Inorganic Analytical Laboratory (RIAL) in the Rutgers University Department of Marine and Coastal Sciences (NJ, USA). In summer 2017 the meltwater and coastal seawater samples were acidified to pH < 2 with 2 mL L^{-1} and 1 mL L^{-1}, respectively, of concentrated ultrapure hydrochloric acid (Optima grade, Fisher Scientific) and stored in the dark chilled at +4°C for multiple months. Subsequently, the meltwater samples were analyzed by direct injection on an Element 1 sector-field inductively coupled plasma mass spectrometer (ICP-MS; Finnigan MAT), against acid-matrix matched external standard curves, with In used for normalizing sensitivity drift. The coastal seawater samples were analyzed by sector-field ICP-MS following procedures modified from Lagerström et al. (2013), as described by Sherrell et al. (2018). Briefly, 10 mL aliquots of the coastal seawater samples were extracted using a SeaFAST pico system (Elemental Scientific) after online buffering to a pH of ~6.5 with ammonium acetate and a 25-fold pre-concentration into 10% (v/v) ultrapure nitric acid (Optima grade, Fisher Scientific). These extracts were then run on the sector-field ICP-MS. Standardization of Fe, Zn, Ni, Cu, Cd, and Pb was performed with isotope dilution. Standardization of Mn was performed with external matrix-matched standards, extracted and pre-concentrated identically to the samples. Following Sherrell et al. (2018), for both the meltwater and coastal seawater samples, if sample duplicates were within 15% (difference about the mean) the mean is reported, otherwise the lower value is reported.

4.3.4 Macronutrients

The meltwater and coastal seawater macronutrient samples were analyzed for the determination of phosphate, nitrate+nitrite, and silicate (all μM). Analyses were carried out during spring 2017 at Lamont-Doherty Earth Observatory (Columbia University, NY, USA), according to the Joint Global Ocean Flux Study (JGOFS) protocols (Lorenzoni and Benway 2013). Samples were run on a AA3 HR AutoAnalyzer (SEAL Analytical), and followed the Seal Analytical methods (all Multitest MT 19) G-297-03 Rev. 4, G-172-96 Rev. 16, and G-177-96 Rev. 11 for phosphate, nitrate+nitrite (henceforth "nitrate"), and silicate, respectively.

4.3.5 Oxygen isotopes

The meltwater, coastal seawater, and glacial ice oxygen isotope samples were analyzed for the determination of the ratio of stable oxygen isotopes of water ($\delta^{18}O$, ‰). Analyses were carried out during fall 2017 at the Natural Environment Research Council (NERC) Isotope Geosciences Laboratory (British Geological Survey, Nottingham, UK), and followed the equilibration method for oxygen (Epstein and Mayeda 1953). Samples were run on an Isoprime mass spectrometer (Elementar). Isotope ratios are expressed relative to Vienna Standard Mean Ocean Water, with a precision of 0.04 ‰ or better based on duplicate analyses.

4.3.6 Continuous stream discharge

For both Stream 1 and 2, the discrete measurements of stream discharge were made near a submerged stream height (m) Levelogger (Solinst), which was coupled with

an adjacent atmospheric pressure (kPa) Barologger (Solinst) (Supplementary Table 4.1). These data loggers were deployed for the entire sampling season, secured within the stream bed topography, and recorded continuously every minute. During sampling events it was periodically discovered that the data loggers for Stream 1 had been dislodged by large waves generated by glacial calving events, which limited the analysis of their data (discussed below). The data loggers for both Stream 1 and 2 were routinely downloaded and redeployed. To increase the number of coincident measurements of discrete stream discharge and continuous stream height and atmospheric pressure, discrete measurements of stream discharge independent of full stream sampling events were made during the sampling season as time permitted (Table 4.1).

The continuous stream height and atmospheric pressure data were quality-controlled by removing any data collected within 5 minutes of periods when the data loggers were downloaded and redeployed. For Stream 1, data were also removed during periods subsequent to the data loggers being dislodged by large waves generated by glacial calving events, which were clearly apparent in the dataset. This resulted in ~40% of the Stream 1 data being removed. For both Stream 1 and 2, continuous stream height was converted to continuous stream pressure through division by 0.101972 m kPa^{-1} and then subtraction of continuous atmospheric pressure. Due to the large gaps in the Stream 1 data, it was only possible to correct the Stream 2 continuous stream pressure for magnitude offsets resulting from very small changes in the orientation of the data loggers during redeployment. This was performed by calculating a 5-minute average of the Stream 2 continuous stream pressure data immediately before/after redeployment, and removing the offset between these averages from data following the redeployment. The

Stream 1 and 2 uncorrected stream pressure, and the Stream 2 offset-corrected stream pressure, were then converted back to stream height through multiplication by 0.101972 m kPa^{-1}.

To compare the diurnal cycles (midnight to midnight) of Stream 1 and 2 continuous stream height (and thus stream discharge) independent of the difference in discharge magnitude between Stream 1 and 2, and without the confounding impacts of magnitude offsets in the Stream 1 data, the uncorrected stream height for both streams were integral-normalized. Specifically, for each diurnal cycle of the sampling season, the corresponding uncorrected stream height data was first temporally smoothed by averaging into 30-minute bins. Next, the temporal integral (i.e. area under of the curve) of the smoothed diurnal cycle was calculated. Each value of the smoothed diurnal cycle was then divided by the temporal integral. This normalization minimized the variability between individual diurnal cycles due to differences in magnitude, while preserving variability due to differences in shape. Only complete diurnal cycles (i.e. those with data for each 30-minute bin) were considered.

To convert the Stream 2 continuous stream height into continuous stream discharge, a matchup analysis with the discrete stream discharge was performed. Specifically, for each measurement of discrete stream discharge (including those not part of a stream sampling event), an adjacent 5-minute average of continuous offset-corrected stream height was calculated. With this matchup dataset, a power regression model was then constructed between the continuous offset-corrected stream height and discrete stream discharge (Supplementary Figure 4.1). This model was used to convert continuous

offset-corrected stream height (x) to continuous stream discharge (y): y = (0.001)x^(3.735).

4.4 Results

4.4.1 Stream discharge

The time series of Stream 1 and 2 discrete discharge indicate that both streams displayed a seasonal cycle in discharge, which was generally characterized by an increase then decrease from the beginning to the end of the field season (Figure 4.2). However, Stream 2 had substantially more discharge than Stream 1, with a seasonal median discharge value of ~13 L s^{-1} for Stream 2 vs. ~1 L s^{-1} for Stream 1 (Table 4.2 and 4.3). The seasonal cycle in Stream 2 discharge is also evident in the time series of Stream 2 continuous discharge (Figure 4.3), which additionally indicates the presence of substantial sub-seasonal variability, including periods of sustained elevated discharge that persisted for multiple days, and especially diurnal variability. Stream 1 and 2 both displayed a similar diurnal cycle in discharge, which was generally characterized by an increase in the late morning to a maximum in the late afternoon or early evening, followed by a decline throughout the night and subsequent morning (Figure 4.4). However, relative to Stream 2, the diurnal cycle in Stream 1 discharge was characterized by a larger amplitude, and an earlier and faster increase and decrease, which resulted in a maximum discharge ~2 hours earlier (16:00 vs 18:00 local, respectively).

4.4.2 Oxygen isotopes

The seasonal median $\delta^{18}O$ value for both Stream 1 and 2 glacial meltwater was approximately -11.90‰ (Table 4.2 and 4.3). This is lower than the seasonal median $\delta^{18}O$ coastal seawater values of -1.11‰ and -1.22‰ for Stream 1 and 2 (Table 4.4 and 4.5), respectively, and higher than the median $\delta^{18}O$ value of -12.98‰ for glacial ice collected in Arthur Harbor (Table 4.6). The time series of Stream 1 and 2 glacial meltwater $\delta^{18}O$ indicate that neither stream displayed a seasonal cycle in $\delta^{18}O$ similar to that observed for discharge. However, both Stream 1 and 2 displayed a seasonal increase in $\delta^{18}O$, from -12.03‰ and -11.96‰ at the beginning of the field season to -11.79‰ and -11.64‰ at the end, respectively (Figure 4.5).

4.4.3 Trace metals and macronutrients

The Stream 1 and 2 glacial meltwater and coastal seawater trace metal and macronutrient concentrations over the field season are summarized in Figure 4.6 and Table 4.2-4.5 (see also Supplementary Table 4.2-4.5 for more complete dataset). Regarding trace metals, for both Stream 1 and 2, in general the glacial meltwater concentrations were nearly equivalent to or substantially higher than the coastal seawater concentrations (with the exception of Stream 1 Ni, which was lower). This was especially apparent for Cu, Mn, Fe, and Zn, all of which had a seasonal median glacial meltwater concentration at least 10-fold greater than that for coastal seawater. For example, the seasonal median Fe glacial meltwater (coastal seawater) concentration for Stream 1 was 301 nM (17.1 nM), and for Stream 2 was 228 nM (12.5 nM). There were differences between the Stream 1 and 2 glacial meltwater trace metal concentrations. Specifically,

relative to Stream 1, the Stream 2 seasonal median glacial meltwater concentration was higher for Cu, Mn, Zn, Ni, and Cd, and lower for Pb. Regarding macronutrients, for both Stream 1 and 2, in general the glacial meltwater concentrations of phosphate and nitrate were nearly equivalent to the coastal seawater concentrations. In particular, the seasonal median phosphate and nitrate glacial meltwater (coastal seawater) concentration for Stream 1 was 0.620 and 4.87 μM (1.17 and 15.6 μM), and for Stream 2 was 0.730 and 22.4 μM (1.20 and 17.4 μM). Additionally, for both Stream 1 and 2, the glacial meltwater concentrations of silicate were much lower than the coastal seawater concentrations. Specifically, the seasonal median silicate glacial meltwater (coastal seawater) concentration for Stream 1 was 2.10 μM (54.0 μM), and for Stream 2 was 0.960 μM (50.9 μM).

The time series of many Stream 1 and 2 glacial meltwater trace metal and macronutrient concentrations displayed a seasonal cycle (either an increase then decrease or decrease then increase from the beginning to the end of the field season), similar to the time series of stream discharge (Figure 4.7). This was especially evident for many of the Stream 2 glacial meltwater elements. A seasonal cycle was not readily apparent in the Stream 1 or 2 coastal seawater trace metal or macronutrient concentrations (Figure 4.8). To assess the relationship between Stream 1 and 2 discharge and glacial meltwater trace metal and macronutrient concentrations, the Pearson correlation coefficient was calculated between discrete discharge and the concentration of each glacial meltwater element (Figure 4.9). The sign of the Stream 1 and 2 correlations were primarily negative, and generally identical between streams. However, relative to Stream 1, Stream 2 had a larger number of correlations that were significant ($p < 0.05$) or moderately

significant ($p < 0.10$). Specifically, for Stream 1, there was a non-significant negative correlation between discrete discharge and the concentration of glacial meltwater silicate, nitrate, Cu, Zn, Ni, Cd, and Pb, and a significant (or moderately significant) positive correlation with phosphate and Fe (there was a non-significant positive correlation with Mn). For Stream 2, there was a significant (or moderately significant) negative correlation between discrete discharge and the concentration of glacial meltwater silicate, nitrate, Cu, Mn, Zn, Ni, and Cd (there was a non-significant negative correlation with Pb), and a significant positive correlation with Fe (there was a non-significant positive correlation with phosphate).

4.5 Discussion

4.5.1 Stream variability

This study has captured variability in the physical characteristics and discharge dynamics of glacial meltwater streams along the WAP. Based on qualitative field observations, Stream 2 was less turbid than Stream 1, and flowed over coarser glacial till at a shallower descent. More quantitatively, Stream 2 was longer than Stream 1 (Figure 4.1), and had 10-fold more discharge (Figure 4.2, Table 4.2 and 4.3). Both streams displayed a seasonal cycle in discharge, characterized by an increase then decrease over the field season (Figure 4.2 and 4.3). Additionally, both streams displayed a prominent diurnal cycle in discharge, characterized an increase throughout the day to an evening maximum, followed by a decrease (Figure 4.4). However, the diurnal cycle of Stream 2 discharge was characterized by a later and slower increase/decrease throughout the day, and a later time of maximum daily discharge (Figure 4.4). These differences in the timing

of discharge dynamics between the two streams likely reflect the larger drainage area of Stream 2 (Figure 4.1).

4.5.2 Chemistry commonalities

Although there were differences in the physical characteristics and discharge dynamics of the two glacial meltwater streams examined in this study, there were common features in their chemical composition. Both streams had a seasonal median $\delta^{18}O$ value of about -11.90‰ (Table 4.2 and 4.3). This value provides an important new constraint for distinguishing and quantifying meteoric water (glacial meltwater plus precipitation) separately from sea ice melt along the WAP (especially in the Palmer Station area) when determining oceanic freshwater budgets by three-endmember mass balance. Briefly, this method was developed by Östlund and Hut (1984), and makes use of the fact that higher-latitude precipitation (and thus meteoric water) is isotopically lighter (i.e. has more negative $\delta^{18}O$ values) than sea ice, which is isotopically similar to its seawater source (Lehmann and Siegenthaler 1991). This analysis requires reliable mean $\delta^{18}O$ values for the meteoric water, sea ice, and seawater endmembers. For regional WAP calculations, a meteoric water endmember value of -16.00‰ is used (Meredith et al. 2017), which is a composite of values for regional ice cores and precipitation. For local Palmer Station calculations, a meteoric water endmember value of -12.00‰ has been proposed (M. Meredith unpublished data), which is an average of the International Atomic Energy Agency (IAEA) Global Network of Isotopes in Precipitation (GNIP) mean value of -10.50‰ for Vernadsky/Faraday Station precipitation, and the value of -13.00‰ reported by Potter and Paren (1985) for meteoric water on the northern end of

the George VI ice shelf (approximately 50 km and 600 km south of Palmer Station, respectively).

The glacial meltwater $\delta^{18}O$ value of -11.90‰ reported here provides directly-measured corroboration of the previously estimated endmember value for Palmer Station meteoric water, and insight into its seasonal variability. This glacial meltwater $\delta^{18}O$ value is higher than the median glacial ice $\delta^{18}O$ value of approximately -13.00‰ reported here (Table 4.6). Given the IAEA GNIP mean $\delta^{18}O$ value of -10.50‰ for Vernadsky/Faraday Station precipitation, this suggests that the glacial meltwater streams examined in this study contained a non-negligible local precipitation component. Furthermore, the seasonal increase in meltwater $\delta^{18}O$ (Figure 4.5, Table 4.2 and 4.3) suggests that this precipitation component increased over the field season, perhaps due to gradual infiltration of a sub-glacial reservoir. Regardless of the driver, the temporal variability in glacial meltwater $\delta^{18}O$ reported here for Palmer Station should be considered in long term studies of local and regional WAP oceanic freshwater budgets, and long-term monitoring of the variability in the meteoric water, sea ice, and seawater endmember $\delta^{18}O$ should be a priority.

Additionally, despite differences in the physical characteristics and discharge dynamics of the two glacial meltwater streams examined in this study, in general both streams have trace metal and macronutrient concentrations nearly equivalent to or greater than those of the coastal seawater (Figure 4.6, Table 4.2-4.5). Exceptions to this pattern include Stream 1 Ni, and silicate for both Stream 1 and 2. These results suggest that, excluding silicate, WAP glacial meltwater could be a source of these trace metals and macronutrients to the coastal ocean. Furthermore, there was a general pattern for both

streams of a positive correlation between discharge and glacial meltwater Fe and phosphate concentration, and a negative correlation for all other trace metal and macronutrient concentrations (Figure 4.9). This pattern is especially apparent for Stream 2. These results suggest that Fe and phosphate in these two WAP glacial meltwater streams are in a different physicochemical state than the other trace metals and macronutrients, and that during periods of high discharge, there is a source of Fe and phosphate, while the other elements are diluted.

4.5.3 Coastal seawater impacts

Previous studies along the WAP have hypothesized that Fe may limit primary production (Garibotti et al. 2003, Smith et al. 2008, Huang et al. 2012, Annett et al. 2017, Schofield et al. 2018, Sherrell et al. 2018), or that a glacial meltwater chemical constituent controls phytoplankton community composition, in particular the proportion of diatoms and cryptophytes (Schofield et al. 2017). In addition to high Fe concentrations, the two glacial meltwater streams examined in this study had very high Cu and low silicate concentrations relative to coastal seawater (Figure 4.6, Table 4.2-4.5). It has been observed that elevated Cu concentrations can be toxic to phytoplankton (Brand et al. 1986, Mann et al. 2002), with modes of toxicity including nutrient uptake disruption, enzyme interference, and diminished growth and photosynthetic rates (Mann et al. and references therein). Additionally, diatoms utilize silicate to build their frustules. Therefore, one explanation for the association of coastal cryptophytes with low salinities along the WAP (Moline et al. 2004, Schofield et al. 2017) could be high Cu

concentrations and low silicate concentrations driven by glacial meltwater plumes that disadvantages diatoms.

To further examine the potential impact of WAP glacial meltwater on the trace metal and macronutrient concentrations of regional coastal seawater, a two-endmember conservative mixing analysis was considered. The two endmembers used were the glacial meltwater streams examined in this study and Station E of the Palmer LTER program, a long-term offshore sampling site near Palmer Station (see Figure 1 of Schofield et al. 2017). The salinity and density of the glacial meltwater streams was assumed to be 0 and 1000 kg m^{-3}, and an average concentration for glacial meltwater Fe, Cu, and silicate of 265 nmol kg^{-1}, 1000 nmol kg^{-1}, and 1.53 μmol kg^{-1}, respectively, was determined by calculating the mean of the Stream 1 and 2 seasonal median values (Table 4.2 and 4.3). The long-term average and minimum austral summer surface salinity at Station E is ~33.5 and ~32.0, respectively. An average concentration for surface coastal seawater Fe and Cu of 1.65 nmol kg^{-1} and 1.91 nmol kg^{-1}, respectively, was determined by calculating the mean of Station E samples collected during the 2014-15, 2015-16, and 2016-17 austral summer (Sherrell et al. 2018, Sherrell unpublished data). A long-term austral summer average concentration for surface coastal seawater silicate of 55.0 μmol kg^{-1} was taken from Figure 6 of Ducklow et al. (2007). Considering a decrease in surface coastal seawater salinity from 33.5 to 32.0 due to mixing with glacial meltwater (approximately 0.95 and 0.05 fractions, respectively), the impact on surface coastal seawater Fe, Cu, and silicate concentrations was determined. These mixing dynamics would result in surface coastal seawater Fe, Cu, and silicate concentrations of 14.8 nmol kg^{-1} (800% increase), 51.8 nmol kg^{-1} (2600% increase), and 52.3 μmol kg^{-1} (5% decrease), respectively. These

calculations suggest that while WAP glacial meltwater could substantially increase regional coastal seawater Fe and Cu concentrations, it would have limited impact on silicate concentrations. It is unlikely that a 5% dilution of coastal seawater silicate would negatively impact coastal diatom populations. However, future studies should investigate the tolerance of coastal WAP diatom and cryptophyte species to these elevated Fe and Cu concentrations with laboratory and field experiments.

4.5.4 Global context

To contextualize the two WAP glacial meltwater streams examined in this study, their mean dissolved (< 0.45 μm) Fe concentration of 265 nM (Table 4.2 and 4.3) was compared to that of glacial sources documented elsewhere in the region, Antarctica, and the globe. In Marian Cove on King George Island along the northern WAP, Kim et al. (2015) estimated glacial meltwater dissolved (< 0.45 μm) Fe concentrations to be 27 nM by extrapolating coastal seawater concentrations to a salinity of 0. Directly south along the WAP on Livingston Island, Hodson et al. (2017) reported a mean glacial runoff dissolved (< 0.45 μm) Fe concentration of 1343 nM. They also reported a mean glacial runoff concentration of 501 nM for both Signy Island and South Georgia Island, located in the maritime Antarctic region of the southern Atlantic. Further south in the Atlantic in the Weddell Sea, and including samples collected from King George Island, Raiswell et al. (2008) presented a mean dissolved (< 0.20 μm) Fe concentration of 1 nM in icebergs. They also presented a mean glacial ice concentration of 2 nM for samples from Taylor Glacier and Canada Glacier, located in the McMurdo Dry Valleys on the Antarctic continent. Elsewhere in the McMurdo Dry Valleys, Green et al. (2005) observed a mean

glacial runoff dissolved (< 0.45 μm) Fe concentration of 335 nM for the glacial meltwater Onyx River.

Expanding to the full globe, there have been many observations in Greenland, in particular from the southwest portion of the Greenland Ice Sheet (GIS). Here, Statham et al. (2008) reported a mean glacial runoff dissolved (0.03 to 0.4 μm range) Fe concentration of 31 nM from Bristol Glacier and Bath Glacier. For glacial river sites of Russel Glacier, Wimpenny et al. (2010) presented a mean dissolved (< 0.20 μm) Fe concentration of 219 nM. Additionally, Bhatia et al. (2013) reported a mean dissolved (< 0.20 μm) Fe concentration of 3700 nM for glacial runoff sourced from multiple GIS outlet glaciers. Furthermore, Hawkings et al. (2014) observed a mean dissolved (0.02 to 0.45 μm range) Fe concentration of 700 nM for glacial meltwater from Leverett Glacier. Elsewhere worldwide, for bulk meltwaters sourced by Haut Glacier d'Arolla in Switzerland, Mitchell et al. (2001) reported a median dissolved (< 0.45 μm) Fe concentration of 6983 nM. Finally, Li et al. (2019) presented mean dissolved (< 0.45 μm) Fe concentrations of 942 nM, 818 nM, and 1559 nM for three glacial proglacial rivers draining Asian glaciers. The various glacial sources of dissolved Fe discussed here span four orders of magnitude in concentration (1s to 1000s of nM), and encompass the concentration of the two WAP glacial meltwater streams examined in this study (265 nM).

4.6 Conclusions

This study presents the chemical composition (trace metals, macronutrients, and $\delta^{18}O$) and discharge dynamics of two WAP glacial meltwater streams. Although these

two streams differ in their physical characteristics and discharge dynamics, they have a nearly identical $\delta^{18}O$ composition, which is valuable for calculating regional oceanic freshwater budgets. Additionally, with the exception of Ni and silicate, both streams have nearly identical or greater concentrations of trace metals and macronutrients relative to coastal seawater. This suggests that WAP glacial meltwater can be a source of these elements to the coastal ocean, and possibly impact coastal phytoplankton communities. The glacial meltwater dataset presented in this study is novel for the WAP. It is predicted that the region will continue to warm, resulting in further glacial retreat, and increased flux of glacial meltwater to the coastal ocean (Henley et al. 2019). Future studies should work to continue to this dataset at Palmer Station, and establish long-term measurements of glacial meltwater elsewhere along the WAP.

4.7 Tables

Table 4.1. Summary of all sampling events, including the respective sampling day, location, date, and corresponding times of the activities performed: coastal seawater (CSW), glacial meltwater (GMW), discrete stream discharge (SD), and glacial ice (GI). Stream sampling events (i.e. those events including CSW, GMW, and SD) are indicated (*).

Ev.	Day	Location	Date (Local)	Time (Local)	Activity
01*	01	Stream 2	2016-12-24	12:11, 13:19, 16:15	CSW, GMW, SD
02*	01	Stream 1	2016-12-24	17:15, 19:37, 20:27	SD, CSW, GMW
03*	02	Stream 1	2017-01-03	15:45, 16:45, 17:43	CSW, GMW, SD
04*	02	Stream 2	2017-01-03	18:21, 19:08, 20:00	CSW, GMW, SD
05	03	Stream 1	2017-01-04	18:50	SD
06	03	Stream 2	2017-01-04	19:32	SD
07*	04	Stream 1	2017-01-11	14:15, 15:09, 16:04	CSW, GMW, SD
08*	04	Stream 2	2017-01-11	17:09, 17:55, 19:05	CSW, GMW, SD
09	05	Stream 1	2017-01-20	14:20	SD
10	05	Stream 2	2017-01-20	15:00	SD
11*	06	Stream 1	2017-01-25	18:54, 19:40, 20:45	CSW, GMW, SD
12	07	Stream 1	2017-01-26	17:10	SD
13	07	Stream 2	2017-01-26	17:47	SD
14*	08	Stream 2	2017-01-28	10:59, 11:45, 12:30	CSW, GMW, SD
15*	09	Stream 1	2017-02-01	17:15, 18:07, 19:10	CSW, GMW, SD
16	09	Stream 2	2017-02-01	19:40	SD
17*	10	Stream 2	2017-02-05	16:55, 17:28, 18:10	CSW, GMW, SD
18	11	Stream 1	2017-02-12	17:55	SD
19	11	Stream 2	2017-02-12	18:40	SD
20*	12	Stream 1	2017-02-16	16:27, 17:13, 15:55	CSW, GMW, SD
21*	13	Stream 2	2017-02-22	15:56, 17:01, 17:40	CSW, GMW, SD
22	14	Stream 2	2017-03-05	14:35	SD
23*	15	Stream 1	2017-03-09	16:39, 17:39, 18:27	GMW, CSW, SD
24*	15	Stream 2	2017-03-09	19:23, 19:59, 21:00	CSW, GMW, SD
25	16	Arthur Harbor	2017-03-13		GI
26	17	Arthur Harbor	2017-03-29		GI
27	18	Arthur Harbor	2017-03-30		GI

Table 4.2. Stream 1 glacial meltwater macronutrient (μM) and trace metal concentrations (nM), $\delta^{18}O$ (‰), and discrete stream discharge (Dis.; L s^{-1}) for stream sampling events, and their seasonal median values.

Date (Local)	H4SiO4	NO3	PO4	Cu	Mn	Fe	Zn	Ni	Cd	Pb	$\delta^{18}O$	Dis.
2016-12-24	5.46	6.74	0.500	376	157	326	89.3	0.883	1.03	0.851	-12.03	0.101
2017-01-03	2.22	3.77	0.840	366	377	506	47.0	0.762	0.615	0.304	-12.09	1.68
2017-01-11	3.57	5.79	0.950	370	399	470	55.9	0.240	0.698	0.238	-11.91	1.55
2017-01-25	1.84	4.14	0.620	541	461	153	80.6	0.526	0.996	0.362	-11.74	0.704
2017-02-01	2.10	4.87	0.610	340	314	142	67.2	0.119	0.846	0.174	-11.85	0.620
2017-02-16	0.450	1.86	0.550	312	226	188	57.2	NA	0.756	0.475	-11.66	0.764
2017-03-09	1.47	23.0	0.800	671	884	301	138	1.49	1.75	0.444	-11.79	0.605
Median:	**2.10**	**4.87**	**0.620**	**370**	**377**	**301**	**67.2**	**0.644**	**0.846**	**0.362**	**-11.85**	**0.704**

Table 4.3. Stream 2 glacial meltwater macronutrient (μM) and trace metal concentrations (nM), $\delta^{18}O$ (‰), and discrete stream discharge (Dis.; L s^{-1}) for stream sampling events, and their seasonal median values.

Date (Local)	H4SiO4	NO3	PO4	Cu	Mn	Fe	Zn	Ni	Cd	Pb	$\delta^{18}O$	Dis.
2016-12-24	1.84	46.7	0.160	3670	2340	135	312	23.6	2.70	0.0719	-11.96	2.95
2017-01-03	1.11	21.9	0.340	1820	1210	228	169	11.7	1.37	0.0379	-12.00	12.8
2017-01-11	0.650	15.4	0.540	1400	1110	283	149	8.42	1.20	0.0672	-11.89	21.2
2017-01-28	0.820	14.1	0.880	1410	983	260	131	7.32	1.08	0.0322	-11.08	17.0
2017-02-05	0.840	22.4	1.19	1190	1020	233	130	6.89	1.15	0.0433	-11.88	24.7
2017-02-22	0.960	36.6	1.03	1630	1400	134	172	9.16	1.55	0.0568	-11.71	11.2
2017-03-09	1.52	63.2	0.730	2420	2330	107	261	14.8	2.14	0.0598	-11.64	8.17
Median:	**0.960**	**22.4**	**0.730**	**1630**	**1210**	**228**	**169**	**9.16**	**1.37**	**0.0568**	**-11.88**	**12.8**

Table 4.4. Stream 1 coastal seawater macronutrient (μM) and trace metal concentrations (nM) and $\delta^{18}O$ (‰), and their seasonal median values.

Date (Local)	H4SiO4	NO3	PO4	Cu	Mn	Fe	Zn	Ni	Cd	Pb	$\delta^{18}O$
2016-12-24	63.1	19.5	1.37	5.23	6.09	5.09	4.95	6.50	0.700	0.0280	-0.66
2017-01-03	28.2	7.52	0.890	160	182	52.0	17.3	4.26	0.472	0.148	-5.79
2017-01-11	54.0	15.6	1.17	35.8	27.6	21.8	6.25	6.16	0.313	0.149	-1.11
2017-01-25	57.6	12.2	0.900	4.41	6.39	6.69	5.42	6.28	0.540	0.0289	-0.68
2017-02-01	47.7	14.8	1.09	29.2	28.2	12.8	6.69	5.59	0.366	0.141	-2.57
2017-02-16	56.8	20.3	1.43	8.94	14.3	17.1	8.65	6.20	0.410	0.0653	-0.78
2017-03-09	47.1	19.9	1.40	24.4	29.1	18.3	6.14	6.04	0.462	0.158	-1.23
Median:	**54.0**	**15.6**	**1.17**	**24.4**	**27.6**	**17.1**	**6.25**	**6.16**	**0.462**	**0.141**	**-1.11**

Table 4.5. Stream 2 coastal seawater macronutrient (μM) and trace metal concentrations (nM) and $\delta^{18}O$ (‰), and their seasonal median values.

Date (Local)	H4SiO4	NO3	PO4	Cu	Mn	Fe	Zn	Ni	Cd	Pb	$\delta^{18}O$
2016-12-24	62.0	20.4	1.39	13.4	12.2	5.10	5.28	6.56	0.700	0.0300	-0.81
2017-01-03	36.3	13.5	0.640	453	335	36.1	47.6	7.87	0.562	0.0353	-4.25
2017-01-11	56.0	17.4	1.20	86.2	68.5	18.9	12.3	6.61	0.321	0.0642	-1.24
2017-01-28	55.8	13.8	0.990	14.0	17.3	12.5	5.14	6.14	0.471	0.0358	-0.90
2017-02-05	50.9	13.6	1.12	78.6	61.2	21.1	10.9	6.57	0.439	0.0568	-1.22
2017-02-22	50.9	19.2	1.36	20.7	23.0	11.8	5.42	6.36	0.386	0.0471	-1.06
2017-03-09	46.7	20.4	1.37	48.4	64.9	10.7	10.8	6.39	0.475	0.0493	-1.33
Median:	**50.9**	**17.4**	**1.20**	**48.4**	**61.2**	**12.5**	**10.8**	**6.56**	**0.471**	**0.0471**	**-1.22**

Table 4.6. Measurements of Stream 1 and 2 discrete stream discharge (Dis.; L s^{-1}) and Arthur Harbor glacial ice $\delta^{18}O$ for non-stream sampling events.

Date	**Location**	**$\delta^{18}O$**	**Dis.**
2017-01-04	Stream 1		0.924
2017-01-04	Stream 2		11.5
2017-01-20	Stream 1		0.817
2017-01-20	Stream 2		12.0
2017-01-26	Stream 1		1.68
2017-01-26	Stream 2		19.1
2017-02-01	Stream 2		18.2
2017-02-12	Stream 1		0.923
2017-02-12	Stream 2		23.1
2017-03-05	Stream 2		2.64
2017-03-13	Arthur Harbor	-12.62	
2017-03-29	Arthur Harbor	-12.98	
2017-03-30	Arthur Harbor	-13.05	

4.8 Figures

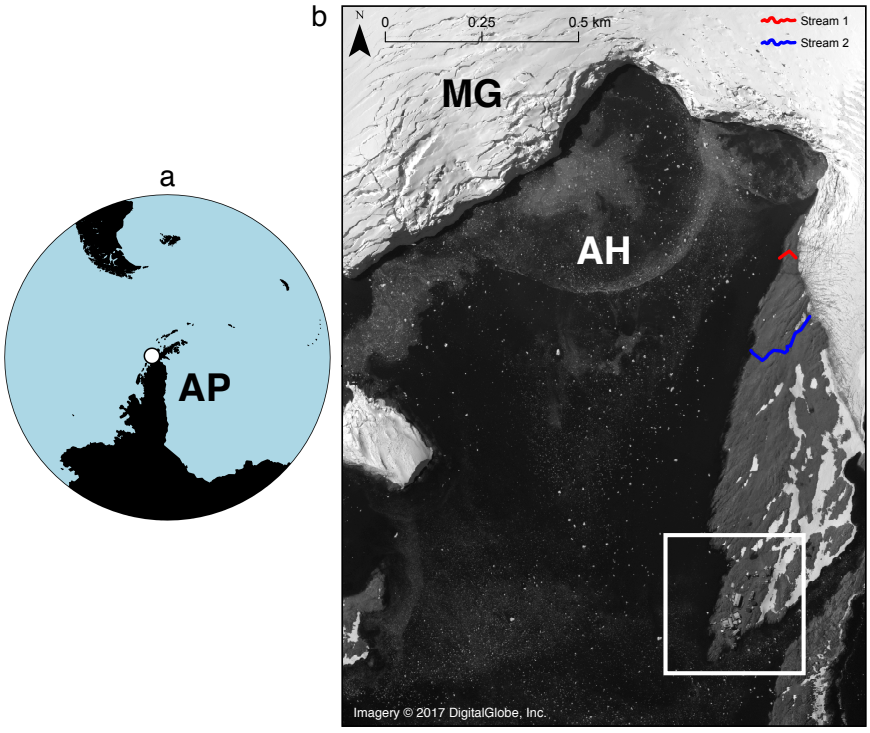

Figure 4.1. Map of the study area, including: **a** the Southern Ocean and Antarctic Peninsula (AP) and **b** Palmer Station and the surrounding area. In **a**, the white circle marks the area of Anvers Island on the West Antarctic Peninsula shown in **b**. In **b**, the red and blue lines indicate the two sampled glacial meltwater streams (Stream 1 and 2, respectively), located to the north of Palmer Station (indicated by the white box), and which flow from the Marr Glacier (MG) into Arthur Harbor (AH).

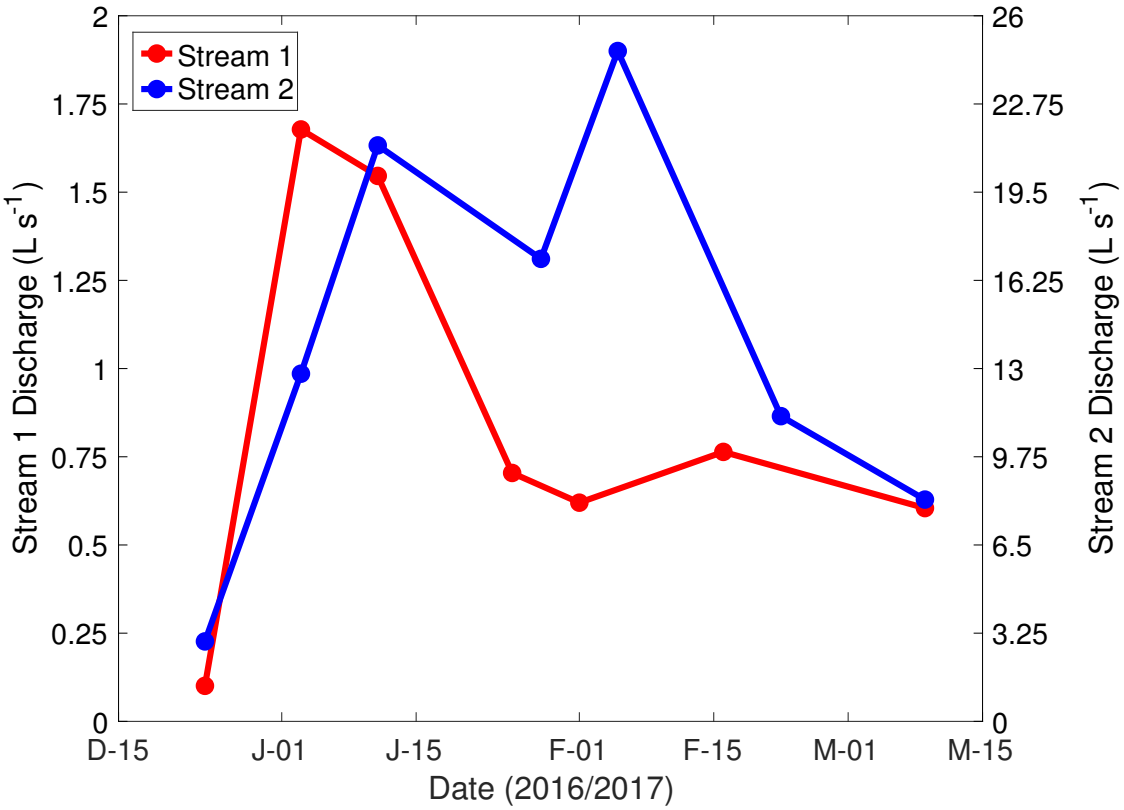

Figure 4.2. Time series of Stream 1 and 2 discrete stream discharge at the stream sampling events.

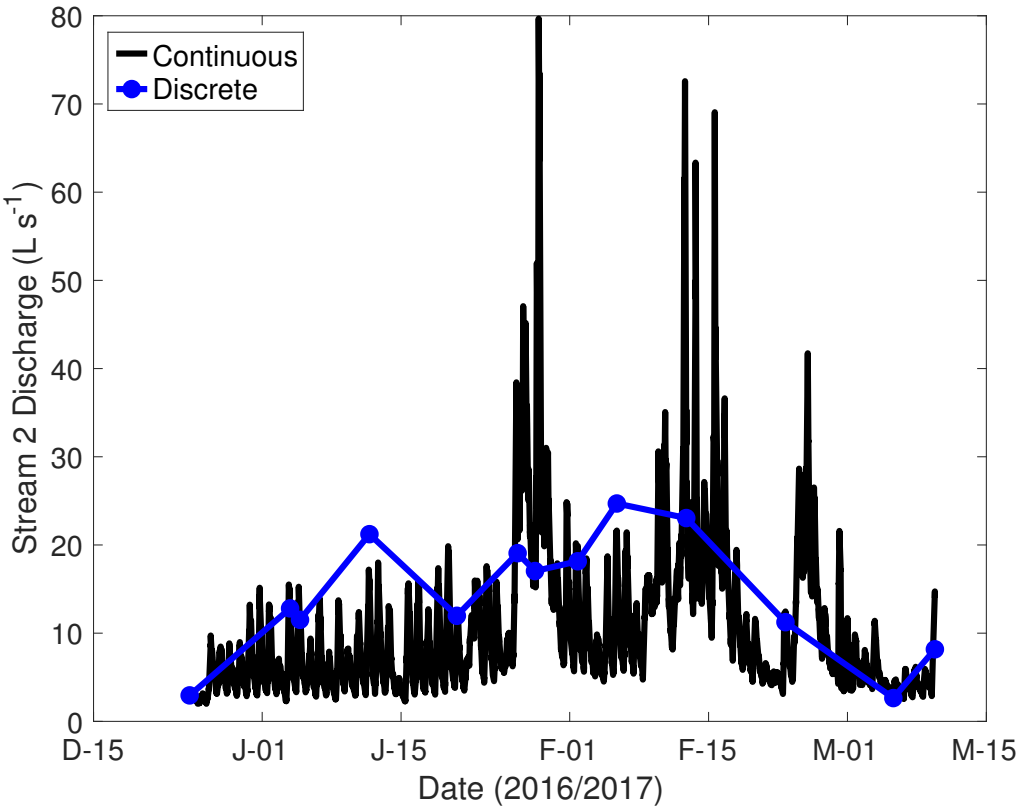

Figure 4.3. Time series of Stream 2 discrete and continuous stream discharge. Here, all discrete stream discharge measurements are included.

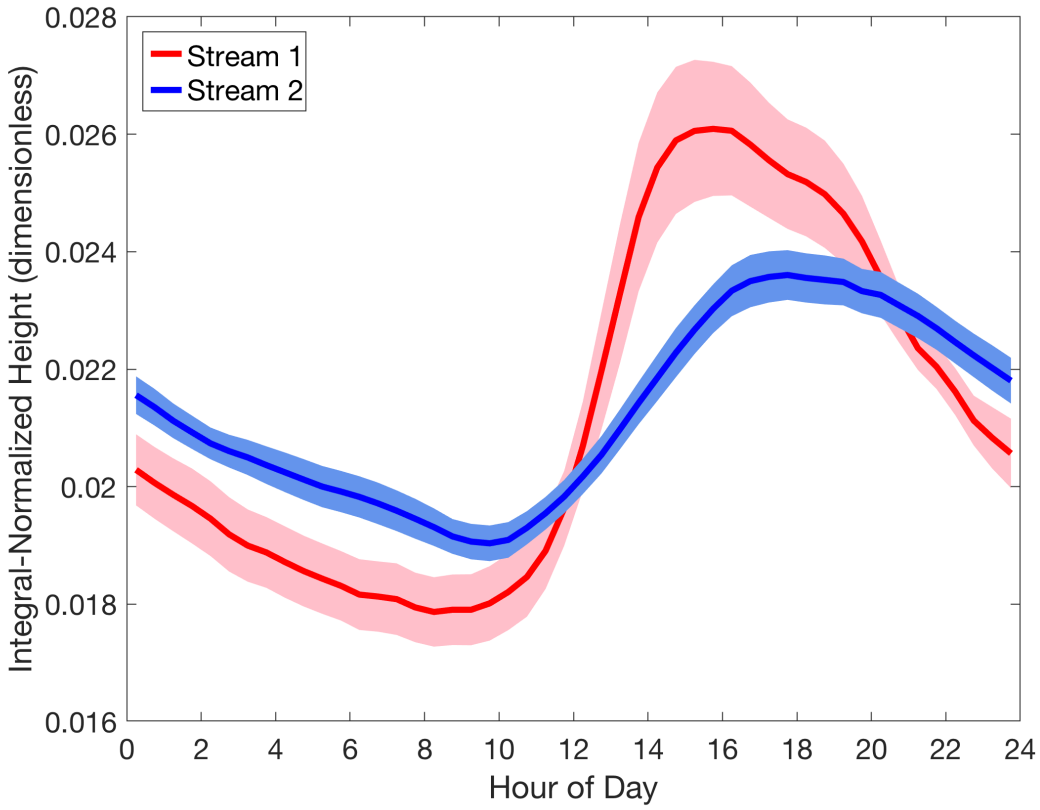

Figure 4.4. Average (± 2SE) diurnal cycle of Stream 1 and 2 integral-normalized stream height (temporally-averaged to 30 minute bins).

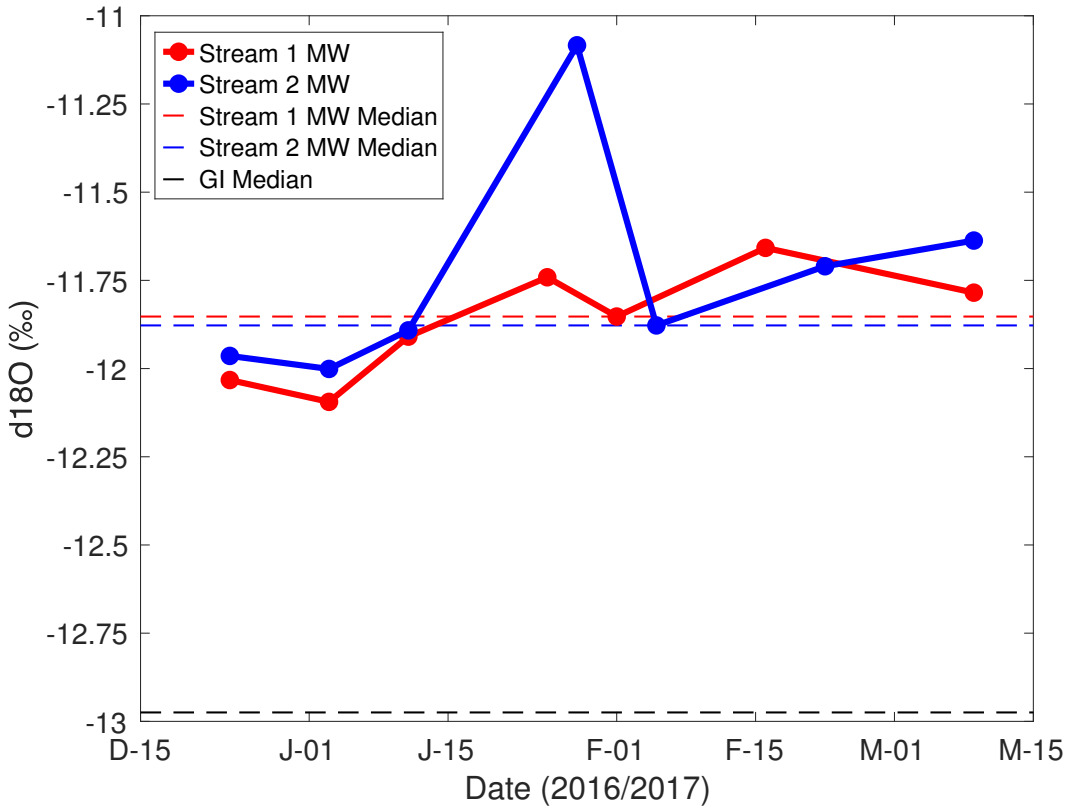

Figure 4.5. Time series of Stream 1 and 2 glacial meltwater (MW) $\delta^{18}O$ (solid lines). Also shown are the time series median values, and the Arthur Harbor glacial ice (GI) median value (horizontal dashed lines).

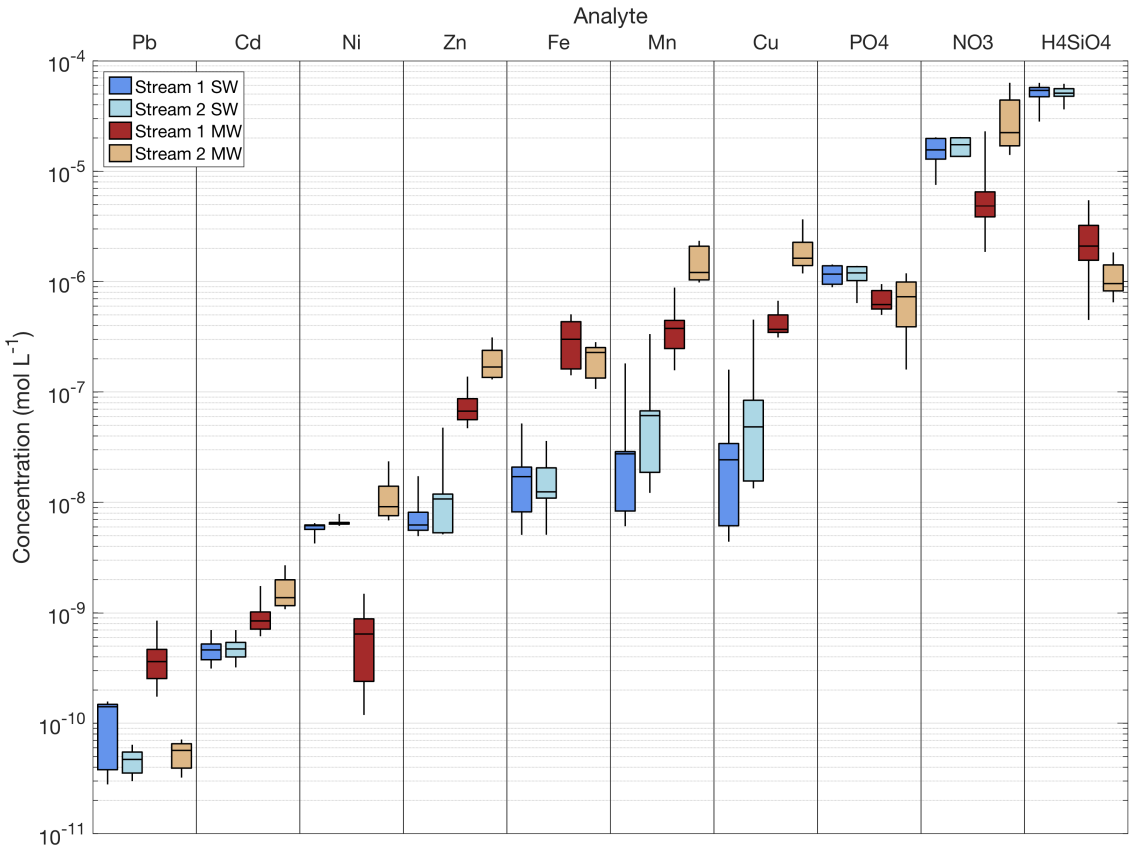

Figure 4.6. Boxplots of Stream 1 and 2 coastal seawater (SW) and glacial meltwater (MW) macronutrient and trace metal analyte concentrations. The horizontal lines of the boxes indicate the 25th, 50th, and 75th percentiles, respectively, and the vertical black solid lines extend from the minimum to the maximum value.

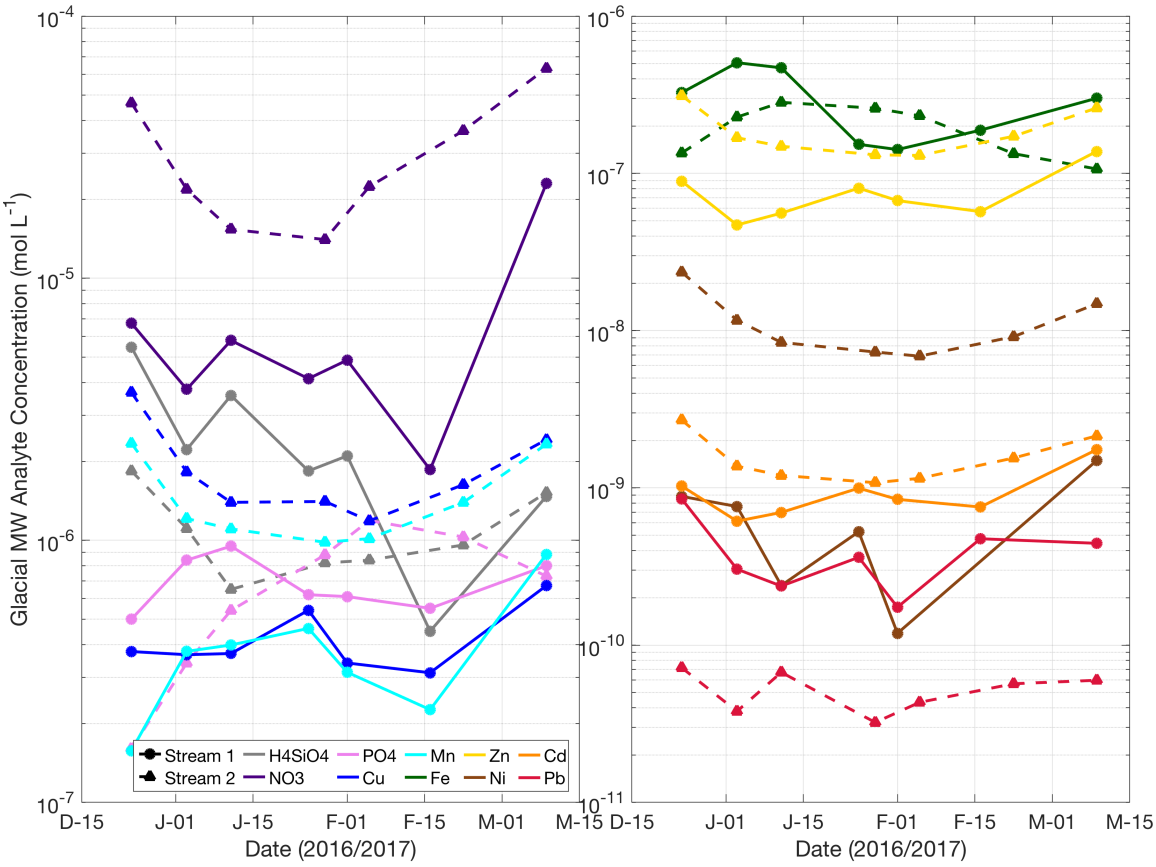

Figure 4.7. Time series of Stream 1 and 2 glacial meltwater (MW) macronutrient and trace metal analyte concentrations. Stream 1 (2) is indicated by the solid (dashed) lines and circles (triangles).

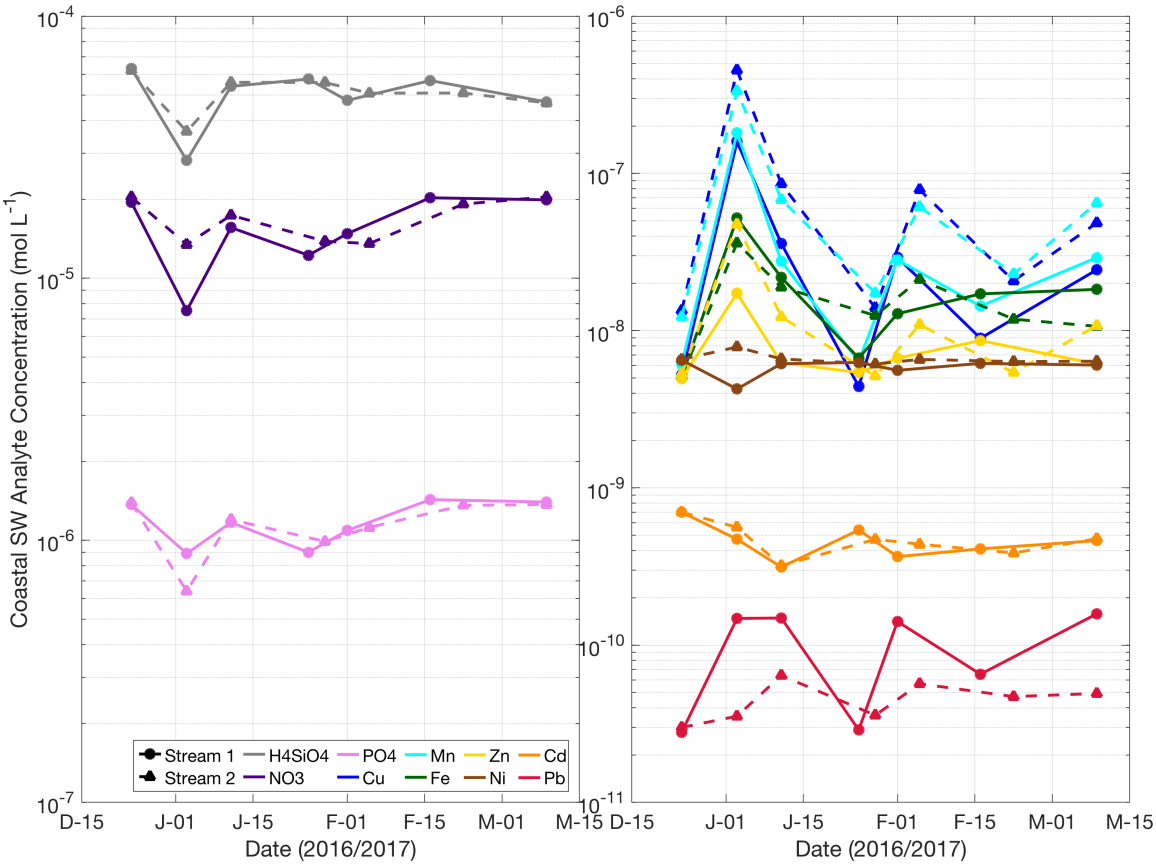

Figure 4.8. Time series of Stream 1 and 2 coastal seawater (SW) macronutrient and trace metal analyte concentrations. Stream 1 (2) is indicated by the solid (dashed) lines and circles (triangles).

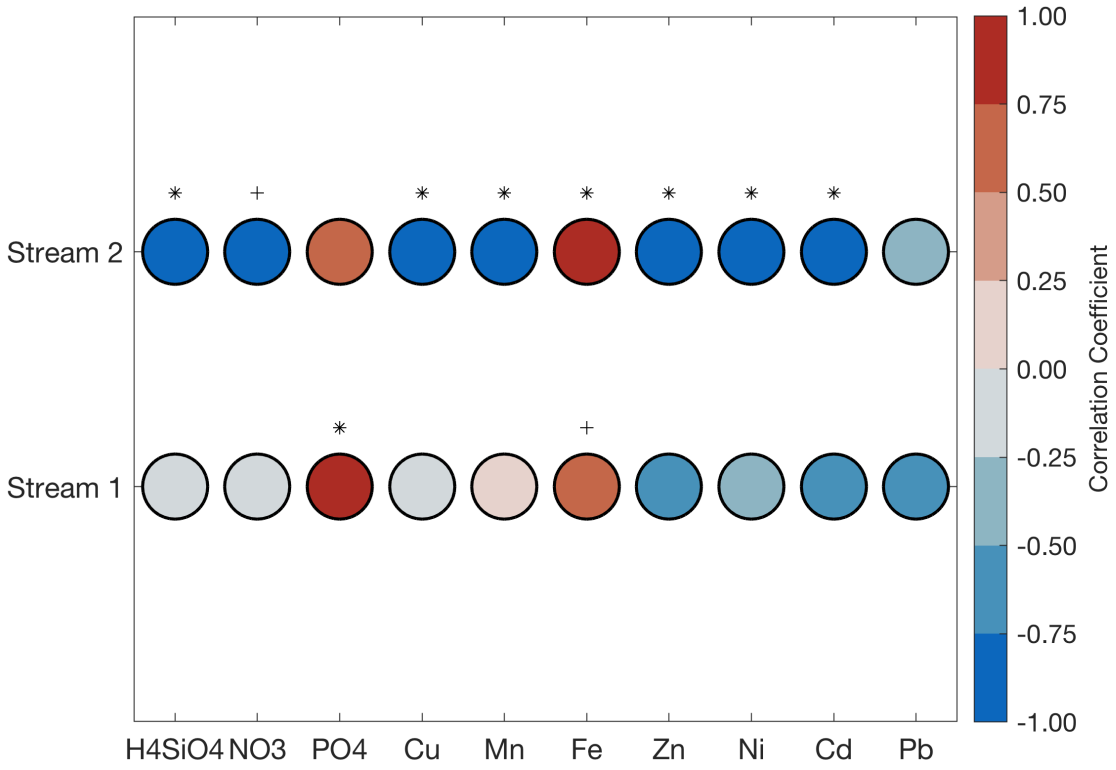

Figure 4.9. Pearson correlation coefficients between discrete stream discharge and glacial meltwater macronutrient and trace metal analyte concentrations for Stream 1 and 2. Correlations significant at $p < 0.05$ (*) or $p < 0.10$ (+) are indicated.

4.9 Supplementary tables

Supplementary Table 4.1. Stream 1 and 2 GPS way points. The terms “coast”, “mouth”, “logger”, and “flow” indicate the locations of the coastal seawater sample sites, glacial meltwater sample sites, stream height and atmospheric pressure data logger sites, and discrete stream discharge measurement sites, respectively. The terms “left turn” and “right turn” indicate the orientation of the stream when facing the Marr glacier.

Stream 1			Stream 2		
Way Point	**Lat/Lon**	**Note**	**Way Point**	**Lat/Lon**	**Note**
1	-64.7716500 N -64.0353333 E	Coast	1	-64.7719833 N -64.0404167 E	Coast
2	-64.7716833 N -64.0351833 E	Mouth, Logger, Flow	2	-64.7720500 N -64.0405000 E	Mouth
3	-64.7717833 N -64.0347667 E	Midway to glacier	3	-64.7723167 N -64.0406333 E	Left turn
4	-64.7719833 N -64.0349333 E	Glacier	4	-64.7723667 N -64.0404000 E	Logger
			5	-64.7723833 N -64.0401833 E	Flow
			6	-64.7724500 N -64.0398833 E	Right turn
			7	-64.7726000 N -64.0397500 E	Tower
			8	-64.7727000 N -64.0397500 E	Left turn
			9	-64.7727333 N -64.0395667 E	Left turn
			10	-64.7726833 N -64.0393833 E	Right turn
			11	-64.7727500 N -64.0392833 E	Left turn
			12	-64.7727167 N -64.0385667 E	Right turn
			13	-64.7728000 N -64.0382667 E	Near glacier
			14	-64.7728500 N -64.0374167 E	Glacier

Supplementary Table 4.2. Stream 1 and 2 coastal seawater trace metal concentration sample replicates (nmol kg^{-1}; for each sampling date/location, replicate A is listed, then replicate B), temperature (°C), salinity (ppt), and pH. Temperature and salinity were measured in the ocean (T and S). Salinity was also measured in the TMC 1 L LDPE sampling bottle, along with pH (S_b and pH_b). On 2017-01-03, the Stream 1 replicate A was measured twice.

Date (Local)	Location	Fe	Zn	Ni	Cu	Cd	Pb	Mn	T	S	S_b	pH_b
2016-12-24	Stream 1	5.032	4.831	6.425	4.953	0.683	0.027	5.959	1.00	33.30	33.00	7.00
2016-12-24	Stream 1	4.903	9.968	6.261	5.252	0.682	0.027	5.925				
2016-12-24	Stream 2	5.031	5.074	6.395	12.987	0.681	0.030	11.871	0.80	32.70	32.40	7.50
2016-12-24	Stream 2	4.923	5.235	6.412	13.187	0.684	0.029	11.960				
2017-01-03	Stream 1	51.076	15.917	4.172	152.800	0.439	0.144	176.502	5.20	20.00	18.50	7.50
2017-01-03	Stream 1	50.309	15.878	4.012	152.074	0.440	0.144	178.507				
2017-01-03	Stream 1	64.879	17.849	4.210	158.809	0.481	0.254	177.010				
2017-01-03	Stream 2	47.474	45.244	7.740	435.494	0.564	0.041	328.864	2.10	30.80	22.80	7.00
2017-01-03	Stream 2	35.218	47.592	7.620	447.585	0.533	0.034	325.029				
2017-01-11	Stream 1	21.521	6.161	6.114	35.067	0.305	0.142	26.881	1.90	31.80	31.90	7.00
2017-01-11	Stream 1	21.010	6.038	5.912	34.859	0.307	0.148	26.940				
2017-01-11	Stream 2	24.263	11.901	6.498	85.492	0.380	0.065	66.868	2.60	32.40	31.70	7.00
2017-01-11	Stream 2	18.474	12.002	6.395	82.622	0.313	0.060	66.697				
2017-01-25	Stream 1	7.752	5.654	6.032	4.479	0.536	0.030	6.262	2.00	33.50	33.40	7.50
2017-01-25	Stream 1	6.529	4.916	6.214	4.131	0.517	0.026	6.197				
2017-01-28	Stream 2	12.129	4.941	5.896	13.673	0.457	0.035	16.892	1.60	33.20	32.70	7.00
2017-01-28	Stream 2	12.218	5.095	6.075	13.555	0.462	0.035	16.952				
2017-02-01	Stream 1	12.962	6.522	5.561	28.157	0.354	0.139	27.394	2.30	29.50	28.20	7.50
2017-02-01	Stream 1	12.037	7.702	5.354	28.825	0.359	0.137	27.641				
2017-02-05	Stream 2	21.086	10.671	6.267	76.486	0.429	0.055	60.173	3.10	31.30		7.50
2017-02-05	Stream 2	20.157	10.623	6.542	76.936	0.427	0.055	59.231				
2017-02-16	Stream 1	17.383	8.435	6.046	8.905	0.394	0.065	14.465	2.20	33.30	33.50	7.50
2017-02-16	Stream 1	16.051	9.922	6.041	8.540	0.405	0.062	13.463				
2017-02-22	Stream 2	11.958	5.074	6.224	20.500	0.378	0.047	21.925	1.30	34.00	32.00	7.50

Date (Local)	Location	Fe	Zn	Ni	Cu	Cd	Pb	Mn	T	S	S_b	pH_b
2017-02-22	Stream 2	11.126	5.493	6.183	19.979	0.374	0.045	22.863				
2017-03-09	Stream 1	18.180	5.935	5.899	23.613	0.451	0.153	27.454	0.50	33.00		7.50
2017-03-09	Stream 1	17.531	6.053	5.887	23.916	0.451	0.155	29.357				
2017-03-09	Stream 2	10.433	10.079	6.043	48.521	0.464	0.048	62.968	-0.20	33.00		7.50
2017-03-09	Stream 2	10.367	10.915	6.431	45.878	0.463	0.048	63.719				

Supplementary Table 4.3. Stream 1 and 2 glacial meltwater trace metal concentration sample replicates (nM; for each sampling date/location, replicate A is listed, then replicate B), temperature (°C), salinity (ppt), and pH. Temperature and salinity were measured in the stream (T and S). Salinity was also measured in the TMC 1 L LDPE sampling bottle, along with pH (S_b and pH_b).

Date (Local)	Location	Fe	Zn	Ni	Cu	Cd	Pb	Mn	T	S	S_b	pH_b
2016-12-24	Stream 1	326.325	86.851	0.873	368.675	1.027	0.814	154.086	2.40	0.00	0.00	6.50
2016-12-24	Stream 1	394.081	91.692	0.893	383.977	1.027	0.888	160.883				
2016-12-24	Stream 2	133.810	312.527	22.927	3639.404	2.733	0.073	2311.741	4.10	0.00	0.00	6.00
2016-12-24	Stream 2	135.990	312.463	24.229	3693.749	2.667	0.070	2377.078				
2017-01-03	Stream 1	756.025	46.408	1.679	376.528	0.608	1.034	378.375	9.10	0.00	0.00	6.50
2017-01-03	Stream 1	506.116	47.656	0.762	355.594	0.621	0.304	375.579				
2017-01-03	Stream 2	226.259	164.588	11.383	1809.571	1.341	0.036	1198.839	5.30	0.00	0.00	6.50
2017-01-03	Stream 2	230.363	172.631	11.929	1839.711	1.407	0.040	1222.597				
2017-01-11	Stream 1	469.579	54.160	0.240	364.733	0.700	0.238	402.188	9.00	0.00	0.00	6.50
2017-01-11	Stream 1	820.972	57.670	0.497	374.959	0.696	1.136	395.017				
2017-01-11	Stream 2	283.118	151.561	8.053	1395.743	1.198	0.114	1102.033	7.00	0.00	0.00	6.50
2017-01-11	Stream 2	283.405	146.195	8.787	1396.537	1.205	0.067	1109.387				
2017-01-25	Stream 1	153.135	80.273	0.526	515.491	0.922	0.362	455.616	2.80	0.00	0.00	6.50
2017-01-25	Stream 1	719.689	81.023	0.981	566.174	1.071	2.023	466.810				
2017-01-28	Stream 2	264.563	173.399	7.493	1412.593	1.101	0.038	985.546	4.60	0.00	0.00	6.00
2017-01-28	Stream 2	254.901	131.354	7.138	1400.879	1.059	0.032	980.527				
2017-02-01	Stream 1	143.590	69.684	0.139	348.491	0.868	0.235	318.814	5.10	0.00	0.00	6.50
2017-02-01	Stream 1	140.137	64.678	0.119	332.264	0.824	0.174	308.633				
2017-02-05	Stream 2	226.312	130.128	6.782	1181.548	1.163	0.042	1015.602	7.80	0.00		6.50
2017-02-05	Stream 2	239.199	1195.038	6.989	1192.293	1.139	0.045	1014.626				
2017-02-16	Stream 1	187.198	56.381	-0.382	314.921	0.738	0.460	227.429	3.40	0.00		6.50
2017-02-16	Stream 1	189.575	57.984	-0.120	309.775	0.775	0.490	224.282				
2017-02-22	Stream 2	126.900	169.711	9.231	1626.024	1.525	0.581	1384.732	6.70	0.00	0.00	6.00
2017-02-22	Stream 2	140.411	175.021	9.090	1634.705	1.575	0.057	1405.643				
2017-03-09	Stream 1	1238.127	141.945	1.766	702.733	1.737	2.372	891.979	4.20	0.00		6.00

Date (Local)	Location	Fe	Zn	Ni	Cu	Cd	Pb	Mn	T	S	S_b	pH_b
2017-03-09	Stream 1	300.701	134.118	1.491	639.852	1.766	0.444	875.380				
2017-03-09	Stream 2	106.781	266.023	15.355	2441.601	2.109	0.060	2369.101	3.60	0.00		6.00
2017-03-09	Stream 2	173.554	255.488	14.322	2400.226	2.176	0.082	2283.612				

Supplementary Table 4.4. Stream 1 and 2 glacial meltwater additional trace metal concentration sample replicates (nM), cations (nM, except Ca in ppb), and anions (μM). For each sampling date/location, replicate A is listed, then replicate B.

Date (Local)	Location	Na	Mg	Al	Ca	V	Cr	Co	Sr	Ba	K	F	Cl	SO4
2016-12-24	Stream 1	64131.297	10881.314	706.368	1001.660	6.833	0.509	3.449	38.785	2.751	9122.232	0.577	40.145	34.745
2016-12-24	Stream 1	65648.759	11233.940	830.635	983.576	7.116	0.677	3.501	40.103	3.262	9523.796	0.543	39.807	35.172
2016-12-24	Stream 2	68899.166	20854.240	6423.613	1805.572	2.556	0.338	125.952	154.049	11.155	17489.503	1.050	70.729	84.472
2016-12-24	Stream 2	72960.588	21536.014	6580.607	1790.787	2.495	0.411	129.408	157.991	11.149	18048.760	1.067	71.302	83.952
2017-01-03	Stream 1	37158.028	5981.264	853.381	557.636	14.297	0.584	11.568	25.936	1.690	9296.290	0.730	7.528	23.375
2017-01-03	Stream 1	36832.492	5720.681	320.608	552.346	13.688	0.508	11.344	25.542	2.641	9221.048	0.423	7.538	23.519
2017-01-03	Stream 2	40497.557	10475.991	2731.609	913.000	5.714	0.316	62.739	76.540	5.479	10041.625	0.577	31.693	47.493
2017-01-03	Stream 2	41296.071	10651.737	2774.659	923.595	5.554	0.503	63.869	78.472	5.032	10566.263	0.662	32.083	47.739
2017-01-11	Stream 1	46700.327	6998.923	297.201	647.405	13.928	0.453	12.175	29.773	1.979	10584.855	0.662	11.741	27.765
2017-01-11	Stream 1	46146.480	7159.875	989.015	654.325	14.450	0.757	12.164	30.642	4.857	10555.971	0.832	33.282	28.060
2017-01-11	Stream 2	35246.938	8628.866	1954.071	764.499	10.298	0.427	53.681	62.679	6.238	9989.667	0.645	34.060	39.722
2017-01-11	Stream 2	35253.473	8519.235	1945.707	772.276	10.472	0.428	53.996	63.913	4.248	9860.595	0.798	39.498	39.896
2017-01-25	Stream 1	51231.252	7724.262	325.578	780.299	8.064	0.592	16.383	33.281	1.810	10148.950	0.628	8.191	31.304
2017-01-25	Stream 1	51895.904	8146.040	1319.798	792.733	9.795	0.874	16.805	33.665	3.102	10287.316	0.713	9.296	31.440
2017-01-28	Stream 2	35616.275	7021.220	2489.502	654.451	10.479	0.384	49.061	54.267	3.564	9072.794	0.560	32.395	35.829
2017-01-28	Stream 2	35465.164	6992.515	1929.324	647.978	10.139	0.451	48.256	52.663	3.350	9331.835	0.492	25.767	35.764
2017-02-01	Stream 1	43551.331	7224.137	209.082	656.095	9.483	0.430	7.806	29.287	2.305	9692.663	0.389	11.211	15.784
2017-02-01	Stream 1	42801.974	7032.911	179.850	664.919	9.177	0.526	7.706	29.344	1.484	9403.711	0.406	9.577	25.753
2017-02-05	Stream 2	29783.777	6966.267	1509.441	648.658	15.652	0.524	47.603	52.319	4.099	9422.889	0.611	27.181	30.525
2017-02-05	Stream 2	29590.027	6969.358	8107.163	652.932	15.997	0.446	47.894	51.932	4.699	9842.301	0.781	17.911	30.555
2017-02-16	Stream 1	30484.750	5044.254	333.905	455.386	7.888	0.485	5.216	19.798	1.665	6409.963	0.798	16.908	13.512
2017-02-16	Stream 1	30001.432	4912.042	327.097	468.694	7.624	0.499	5.209	20.283	2.357	6368.085	1.316	29.063	13.304
2017-02-22	Stream 2	36519.977	8723.016	2194.996	874.458	13.292	0.586	64.761	65.290	4.590	11457.589	0.696	14.588	40.856
2017-02-22	Stream 2	37185.814	8879.701	2236.838	849.239	13.376	0.490	65.745	65.850	4.459	11578.179	0.815	14.777	40.856
2017-03-09	Stream 1	80363.792	16830.236	1908.984	1548.247	10.213	1.073	34.412	69.432	4.752	15849.296	0.286	36.042	53.905
2017-03-09	Stream 1	79164.880	16030.597	370.396	1638.231	8.049	0.588	33.914	64.993	4.957	15421.000	0.320	36.886	54.075

Date (Local)	Location	Na	Mg	Al	Ca	V	Cr	Co	Sr	Ba	K	F	Cl	SO4
2017-03-09	Stream 2	59889.200	15343.651	3760.578	1431.882	8.581	0.359	108.685	108.184	7.856	17345.932	0.966	61.312	59.741
2017-03-09	Stream 2	58528.598	14945.260	3691.208	1457.324	8.519	0.486	105.441	105.540	8.482	17326.180	0.781	45.750	60.642

Supplementary Table 4.5. Station B and E trace metal and macronutrient concentration sample replicates (nM and μM; for each sampling date/location, replicate A is listed, then replicate B) and $\delta^{18}O$ (‰).

Date (Local)	Location	Fe	Zn	Ni	Cu	Cd	Pb	Mn	PO4	NO3	H4SiO4	$\delta^{18}O$
2017-01-13	Station B	6.818	2.210	6.124	6.066	0.251	0.042	7.919	1.340	20.070	59.590	-0.901
2017-01-13	Station B	6.982	2.148	6.097	5.114	0.249	0.039	7.294				
2017-02-14	Station E	3.061	2.705	6.203	1.891	0.359	0.014	2.863				
2017-02-14	Station E	3.203	2.728	6.176	1.951	0.354	0.015	2.922				
2017-02-16	Station E	1.960	2.926	6.229	1.785	0.349	0.013	2.730	1.480	22.000	55.640	-0.463
2017-02-16	Station E	1.873	2.916	6.155	1.744	0.347	0.013	2.768				

4.10 Supplementary figures

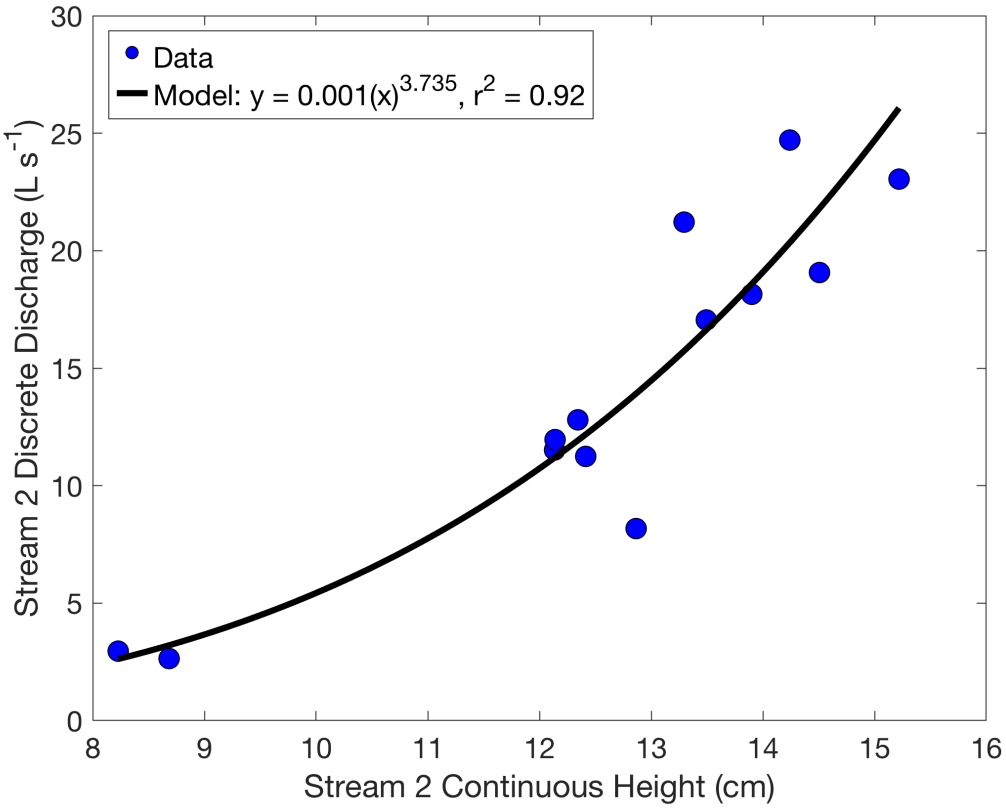

Supplementary Figure 4.1. Relationship between Stream 2 continuous stream height and discrete stream discharge. The power regression model was used to convert continuous stream height to continuous stream discharge. Here, all discrete stream discharge measurements are included.

5 Conclusions

In this dissertation, I have employed a suite of approaches to assess drivers of changes to phytoplankton dynamics along the WAP, and how these changes impact regional biogeochemistry, including oceanic CO_2 uptake. The methods I have used include: 1) the analysis of 25-year datasets of upper ocean physics, phytoplankton dynamics, and biogeochemistry, 2) DNA sequencing to assess phytoplankton diversity, and 3) geochemical characterization of glacial meltwater. Together, these diverse techniques allowed me to comprehensively study a complex polar marine ecosystem that is facing rapid environmental change.

In Chapter 2 (*Enhanced oceanic CO_2 uptake along the rapidly changing West Antarctic Peninsula*), I demonstrated that due to regional warming and melting, long-term changes in upper ocean stability and phytoplankton biomass and community composition have resulted in alterations to oceanic CO_2 uptake along the WAP. A key finding here is that diatoms and cryptophytes, the two major WAP phytoplankton groups, play distinct roles in regional biogeochemistry. Specifically, relative to diatoms, cryptophytes are associated with less oceanic CO_2 uptake. In Chapter 3 (*Low diversity of a key phytoplankton group along the West Antarctic Peninsula*), I demonstrated that there are just two primary WAP cryptophyte taxa. Although the primary taxon consistently dominates the cryptophyte community, shifts in the proportions of the primary and secondary taxa are associated with different sea surface temperature, salinity, macronutrients, and phytoplankton dynamics. In Chapter 4 (*Meltwater chemistry of a*

receding West Antarctic Peninsula glacier), I presented some of the first measurements of the chemical composition and discharge dynamics of WAP glacial meltwater. A key finding here is that regional glacial meltwater can have high concentrations of dissolved trace metals, including iron and copper, which could be critical for structuring coastal phytoplankton communities.

A major theme in this dissertation is the importance of long-term monitoring in ecological research, such as that conducted by the Palmer LTER. For example, in Chapter 2, I hypothesized that the increase in oceanic CO_2 uptake observed along the WAP might be a temporary response of the marine ecosystem to environmental change, and that continued regional warming and melting could ultimately negatively impact oceanic CO_2 uptake, resulting in a positive feedback. It will be important to maintain these long-term measurements of upper ocean physics, phytoplankton dynamics, and biogeochemistry to test this hypothesis in the future. Additionally, as demonstrated in Chapter 3, variability in WAP cryptophyte diversity is associated with physicochemical oceanographic variables that are predicted to be altered with continued environmental change, further justifying the need to extend these datasets. The results of Chapter 3 also indicate the need to incorporate genomic work into long-term ecological measurements along the WAP to better characterize the abundance, composition, and functioning of key taxa.

Finally, in Chapter 4, I identified glacial meltwater as potentially an important source of trace metals to the WAP coastal ocean. Future work should focus on the continuation of these measurements at Palmer Station, expanding them elsewhere, and incorporating additional sampling strategies to assess spatial (e.g. distance from glacier) and temporal (e.g. diurnal) variability. Future work should also focus on assessing the

impact of these glacial meltwater inputs (especially high dissolved iron and copper) on coastal phytoplankton communities along the WAP. This could be accomplished with field and laboratory trace metal manipulations that include representative phytoplankton taxa, including the two major cryptophyte taxa identified in Chapter 3. These experiments could also be modified to incorporate the changing physical conditions to the WAP marine ecosystem that are expected to occur due to continued regional warming and melting. In Appendix A, I summarized the preliminary results of a microcosm experiment examining the impact of WAP glacial meltwater on coastal phytoplankton community composition. To summarize, maintenance of the long-term datasets used in this study, and the incorporation of new time series and experiments, will be critical for building on the work described in this dissertation.

I leave the reader with a final thought on future research opportunities relevant to WAP phytoplankton dynamics and biogeochemistry. A substantial motivation for this dissertation is the observation that WAP cryptophytes are associated with lower salinities (Moline et al. 2004, Schofield et al. 2017), and the future implications for the regional food web and biogeochemistry due to a hypothesized shift from diatoms to cryptophytes resulting from continued sea ice and glacial melt. The irony is that at the conclusion of this dissertation, many questions remain unanswered, and still more were generated during the process (perhaps this should be expected given the long and winding nature of a PhD degree). Regardless, this topic is fertile for research opportunities.

In particular, a major open question is what are the environmental drivers that result in the WAP diatom-cryptophyte dichotomy. As discussed in Chapter 2, determining these drivers is important for predicting future regional food web and

biogeochemical dynamics. An often-overlooked fact is that the association between WAP cryptophytes and lower salinities has primarily been observed at coastal locations, especially near Palmer Station (Moline et al. 2004, Schofield et al. 2017). Interestingly, when this relationship is examined over the entire Palmer LTER regional sampling grid, the pattern is not as clear (Henley et al. 2019). One explanation for this difference between Palmer Station and the full region could be that there are many WAP cryptophyte species that thrive under different conditions. Indeed, this was one of the motivations for Chapter 3. However, in that chapter I demonstrated that there are only two major WAP cryptophyte taxa, and the primary taxon consistently dominates the cryptophyte community over a wide range of oceanographic conditions.

An additional complication is that at Palmer Station, it has been observed that diatoms can also occur at lower salinities, as well as higher ocean temperatures (Schofield et al. 2017). This would suggest that perhaps diatoms might be favored instead of cryptophytes in a warming and melting WAP. However, in Chapter 3, I demonstrated that over the entire Palmer LTER regional sampling grid, while cryptophytes are associated with SU1 and SU8, diatoms are associated with SU6, which is characterized by lower ocean temperature and salinity. Finally, further research is needed to understand the driver behind the association between cryptophytes and lower salinities at Palmer Station. In Chapter 4, I presented baseline measurements of trace metal and macronutrient concentrations in WAP glacial meltwater, and formulated a hypothesis that coastal diatoms might experience copper toxicity. As discussed above, these chemical measurements should be continued, and the copper toxicity hypothesis should be investigated. To summarize, it is clear that many important questions remain about the

environmental drivers of WAP phytoplankton dynamics, and how they will be altered as the region continues to warm and melt. Thank you for reading!

6 References

Atkinson, A., V. Siegel, E. Pakhomov, and P. Rothery. 2004. Long-term decline in krill stock and increase in salps within the Southern Ocean. Nature 432: 100–103.

Annett, A. L., J. N. Fitzsimmons, M. J. M. Séguret, M. Lagerström, M. P. Meredith, O. Schofield, and R. M. Sherrell. 2017. Controls on dissolved and particulate iron distributions in surface waters of the Western Antarctic Peninsula shelf. 196: 81–97. doi:10.1016/j.marchem.2017.06.004

Annett, A. L., M. Skiba, S. F. Henley, H. J. Venables, M. P. Meredith, P. J. Statham, and R. S. Ganeshram. 2015. Comparative roles of upwelling and glacial iron sources in Ryder Bay, coastal western Antarctic Peninsula. Mar. Chem. 176: 21–33. doi:10.1016/j.marchem.2015.06.017

Bakker, D. C., and others. 2016. A multi-decade record of high-quality fCO (2) data in version 3 of the Surface Ocean CO2 Atlas (SOCAT). Earth Syst. Sci. Data 8: 383–413. doi:10.5194/essd-8-383-2016

Barbera, P., A. M. Kozlov, L. Czech, B. Morel, D. Darriba, T. Flouri, and A. Stamatakis. 2018. EPA-ng: Massively parallel evolutionary placement of genetic sequences. Syst. Biol. 68: 365–369. doi:10.1093/sysbio/syy054

Bhatia, M. P., E. B. Kujawinski, S. B. Das, C. F. Breier, P. B. Henderson, and M. A. Charette. 2013. Greenland meltwater as a significant and potentially bioavailable source of iron to the ocean. Nat. Geosci. 6: 274–278. doi:10.1038/NGEO1746

Bowman, J. S., M. T. Kavanaugh, S. C. Doney, and H. W. Ducklow. 2018. Recurrent seascape units identify key ecological processes along the western Antarctic Peninsula. Glob. Change Biol. 24: 3065–78. doi:10.1111/gcb.14161

Bown, J., P. Laan, S. Ossebaar, K. Bakker, P. Rozema, and H. J. W. de Baar. 2017. Bioactive trace metal time series during austral summer in Ryder Bay, Western Antarctic Peninsula. Deep-Sea Res. Part II Top. Stud. Oceanogr. 139: 103–119. doi:10.1016/j.dsr2.2016.07.004

Brand, L. E., W. G. Sunda, and R. R. L. Guillard. 1986. Reduction of marine phytoplankton reproduction rates by copper and cadmium. J. Exp. Biol. 96: 225–250. doi:10.1016/0022-0981(86)90205-4

Brown, M. S., D. R. Munro, C. J. Feehan, C. Sweeney, H. W. Ducklow, and O. M. Schofield. 2019. Enhanced oceanic CO_2 uptake along the rapidly changing West Antarctic Peninsula. Nat. Clim. Change. 9: 678–683. doi:10.1038/s41558-019-0552-3

Buma, A. G. J., H. J. W. de Baar, R. F. Nolting, and A. J. van Bennekom. 1991. Metal enrichment experiments in the Weddell-Scotia Seas: Effects of iron and manganese on various plankton communities. Limnol. Oceanogr. 36: 1865–1878.

Callahan, B. J., P. J. McMurdie, M. J. Rosen, A. W. Han, A. J. Johnson, and S. P Holmes. 2016. DADA2: High-resolution sample inference from Illumina amplicon data. Nat. Methods. 13: 581–583. doi:10.1038/nmeth.3869

Callahan, B. J., P. J. McMurdie, and S. P. Holmes. 2017. Exact sequence variants should replace operational taxonomic units in marker-gene data analysis. ISME J. 11: 2639–2643. doi:10.1038/ismej.2017.119

Callahan, B. J. 2018. Silva taxonomic training data formatted for DADA2 (Silva version 132). Zenodo. doi:10.5281/zenodo.1172783

Carrillo, C. J., R. C. Smith, and D. M. Karl. 2004. Processes regulating oxygen and carbon dioxide in surface waters west of the Antarctic Peninsula. Mar. Chem. 84: 161–179.

Carvalho, F., J. Kohut, M. J. Oliver, R. M. Sherrell, and O. Schofield. 2016. Mixing and phytoplankton dynamics in a submarine canyon in the West Antarctic Peninsula. J. Geophys. Res.-Oceans 121: 5069–5083.

Carvalho, F., J. Kohut, M. J. Oliver, and O. Schofield. 2017. Defining the ecologically relevant mixed-layer depth for Antarctica's coastal seas. Geophys. Res. Lett. 44: 338–345

Cook, A. J., A. J. Fox., D. G. Vaughan, and J. G. Ferrigno. 2005. Retreating glacier fronts on the Antarctic Peninsula over the past half-century. Science 308: 541–544

Cook, A. J., P. R. Holland, M. P. Meredith, T. Murray, A. Luckman, and D. G. Vaughan. 2016. Ocean forcing of glacier retreat in the western Antarctic Peninsula. Science. 353: 283–286. doi:10.1126/science.aae0017

Dickson, A. G., and C. Goyet. 1994. Handbook of methods for the analysis of the various parameters of the carbon dioxide system in sea water. Version 2. ORNL/CDIAC-74, Oak Ridge National Laboratory, U.S. Department of Energy, Oak Ridge, Tennessee.

Dlugokencky, E. J., K. W. Thoning, P. M. Langand, and P. M Tans. 2017. NOAA Greenhouse Gas Reference from Atmospheric Carbon Dioxide Dry Air Mole Fractions from the NOAA ESRL Carbon Cycle Cooperative Global Air Sampling Network.

Ducklow, H. W., and others. 2007. Marine pelagic ecosystems: the West Antarctic Peninsula. Phil. Trans. R. Soc. B 362: 67–94. doi:10.1098/rstb.2006.1955

Ducklow, H. W., and others. 2013. West Antarctic Peninsula: An ice-dependent coastal marine ecosystem in transition. Oceanography 26: 190–203. doi:10.5670/oceanog.2013.62

Epstein, S., and T. Mayeda. 1953. Variation of O^{18} content of waters from natural sources. Geochim. Cosmochim. Ac. 4: 213–224. doi:10.1016/0016-7037(53)90051-9

Eveleth, R., N. Cassar, S. C. Doney, D. R. Munro, and C. Sweeney. 2017. Biological and physical controls on O_2/Ar, Ar and pCO_2 variability at the Western Antarctic Peninsula and in the Drake Passage. Deep-Sea Res. Pt. II. 139: 77–88.

Fay, A. R., G. A. McKinley, and N.S. Lovenduski. 2014. Southern Ocean carbon trends: Sensitivity to methods. Geophys. Res. Lett. 41: 6833–6840.

Fogt, R. L., and D. H. Bromwich. 2006. Decadal variability of the ENSO teleconnection to the high-latitude South Pacific governed by coupling with the southern annular mode. J. Clim. 19: 979–997.

Friedlaender, A. S., P. N. Halpin, S. S. Quian, G. L. Lawson, P. H. Wiebe, D. Thiele, and A. J. Read. 2006. Whale distribution in relation to prey abundance and oceanographic processes in shelf waters of the Western Antarctic Peninsula. Mar. Ecol. Prog. Ser. 317: 297–310

Garibotti, I. A., M. Vernet, M. E. Ferrario, R. C. Smith, R. M. Ross, and L. B. Quetin. 2003. Phytoplankton spatial distribution patterns along the western Antarctic Peninsula (Southern Ocean). Mar. Ecol. Prog. Ser. 261: 21–39. doi:10.3354/meps261021

Green, W. J., B. R. Stage, A. Preston, S. Wagers, J. Shacat, and S. Newell. 2005. Geochemical processes in the Onyx River, Wright Valley, Antarctica: major ions, nutrients, trace metals. Geochim. Cosmochim. Ac. 69: 839–850. doi:10.1016/j.gca.2004.08.001

Gruber, N., P. Landschützer, and N. S. Lovenduski. 2019. The variable Southern Ocean carbon sink. Annu. Rev. Mar. Sci. 11: 159–186. doi:10.1146/annurev-marine-121916-063407

Haberman, K. L., R. M. Ross, and L. B. Quetin. 2003. Diet of the Antarctic krill (*Euphausia superba* Dana): II. Selective grazing in mixed phytoplankton assemblages. J. Exp. Mar. Biol. Ecol. 283: 97–113. doi: 10.1016/S0022-0981(02)00467-7

Hall, A., and M. Visbeck. 2002. Synchronous variability in the Southern Hemisphere atmosphere, sea ice, and ocean resulting from the Annular Mode. J. Clim. 15: 3043–3057.

Hart, T. J. 1942. Phytoplankton periodicity in the Antarctic surface waters. Discovery Rep. 21: 261–356.

Hauri, C., S. C. Doney, T. Takahashi, M. Erickson, G. Jiang, and H. W. Ducklow. 2015. Two decades of inorganic carbon dynamics along the West Antarctic Peninsula. Biogeosciences 12: 6761–6779.

Hawkings, J. R., and others. 2014. Ice sheets as a significant source of highly reactive nanoparticulate iron to the oceans. Nat. Commun. 5: 3929. doi:10.1038/ncomms4929

Henley, S. F., and others. 2019. Variability and change in the west Antarctic Peninsula marine system: Research priorities and opportunities. Prog. Oceanogr. 173: 208–237. doi: 10.1016/j.pocean.2019.03.003

Hewes, C. D., E. Sakshaug, F. M. H. Reid, and O. Holm-Hansen. 1990. Microbial autotrophic and heterotrophic eucaryotes in Antarctic waters: Relationships between biomass and chlorophyll, adenosine triphosphate and particulate organic carbon. Mar. Ecol. Prog. Ser. 63: 27–35.

Hodson, A. 2006. Biogeochemistry of snowmelt in an Antarctic glacial ecosystem. Water Resour. Res. 42: W11406. doi:10.1029/2005WR004311

Hodson, A., and others. 2017. Climatically sensitive transfer of iron to maritime Antarctic ecosystems by surface runoff. Nat. Commun. 8: 14499. doi:10.1038/ncomms14499

Hodson, A., T. Heaton, H. Langford, K. Newsham. 2010. Chemical weathering and solute export by meltwater in a maritime Antarctic glacier basin. Biogeochemistry 98: 9–27. doi:10.1007/s10533-009-9372-2

Huang, K., H. Ducklow, M. Vernet, N. Cassar, and M. L. Bender. 2012. Export production and its regulating factors in the West Antarctica Peninsula region of the Southern Ocean. Glob. Biogeochem. Cycles 26: 1–13. doi:10.1029/2010GB004028.

Ito, R. G., V. M. Tavano, C. R. B Mendes, and C. A. Garcia. 2018. Sea-air CO_2 fluxes and pCO_2 variability in the Northern Antarctic Peninsula during three summer periods (2008-2010). Deep-Sea Res. Pt. II 149: 84–98.

Kim, H., S. C. Doney, R. A. Iannuzzi, M. P. Meredith, D. G. Martinson, and H. W. Ducklow. 2016. Climate forcing for dynamics of dissolved inorganic nutrients at Palmer Station, Antarctica: An interdecadal (1993–2013) analysis. J. Geophys. Res. Biogeosci. 121: 2369–2389. doi:10.1002/2015JG003311

Kim, I., G. Kim, and E. J. Choy. 2015. The significant inputs of trace elements and rare earth elements from melting glaciers in Antarctic coastal waters. Polar Res. 34: 24289. doi:10.3402/polar.v34.24289

Kozlowski, W. A., D. Deutschman, I. Garibotti, C. Trees, and M. Vernet. 2011. An evaluation of the application of CHEMTAX to Antarctic coastal pigment data. Deep-Sea Res. Part I Oceanogr. Res. Pap. 58: 350–364. doi:10.1016/j.dsr.2011.01.008

Lagerström, M. E., M. P. Field, M. Séguret, L. Fischer, S. Hann, and R. M. Sherrell. 2013. Automated on-line flow-injection ICP-MS determination of trace metals (Mn, Fe, Co, Ni, Cu and Zn) in open ocean seawater: Application to the GEOTRACES program. Mar. Chem. 155: 71–80. doi:10.1016/j.marchem.2013.06.001

Laybourn-Parry, J., and E. M. Bell. 2014. Ace Lake: Three decades of research on a meromictic, Antarctic lake. Polar Biol. 37: 1685–1699. doi:10.1007/s00300-014-1553-3

Legge, O. J., D. C. Bakker, M. P. Meredith, H. J. Venables, P. J. Brown, E. M. Jones, and M. T. Johnson. 2017. The seasonal cycle of carbonate system processes in Ryder Bay, West Antarctic Peninsula. Deep-Sea Res. Pt. II. 139: 167–180.

Lehmann, M., and U. Siegenthaler. 1991. Equilibrium oxygen- and hydrogen-isotope fractionation between ice and water. J. Glaciol. 37: 23–36. doi:10.3189/S0022143000042751

Lenton, A., and others. 2012. The observed evolution of oceanic pCO_2 and its drivers over the last two decades. Global Biogeochem. Cy. 26: GB2021.

Li, X., and others. 2019. Dissolved iron supply from Asian glaciers: local controls and a regional perspective. Global Biogeochem. Cy. 33: 1223–1237. doi:10.1029/2018GB006113.

Li, Z., N. Cassar, K. Huang, H. Ducklow, and O. Schofield. 2016. Interannual variability in net community production at the Western Antarctic Peninsula region (1997–2014). J. Geophys. Res.-Oceans 121: 4748–4762.

Lin, Y., N. Cassar, A. Marchetti, C. Moreno, H. Ducklow, and Z. Li. 2017. Specific eukaryotic plankton are good predictors of net community production in the Western Antarctic Peninsula. Sci. Rep. 7: 14845, doi: 10.1038/s41598-017-14109-1

Loeb, V., V. Siegel, O. Holm-Hansen, R. Hewitt, W. Fraser, W. Trivelpiece, and S. Trivelpiece. 1997. Effects of sea-ice extent and krill or salp dominance on the Antarctic food web. Nature 387: 897–900.

Lorbacher, K., D. Dommenget, P. P. Niiler, and A. Köhl. 2006. Ocean mixed layer depth: A subsurface proxy of ocean-atmosphere variability. J. Geophys. Res-Oceans 111.

Lorenzoni, L., and H. M. Benway [eds.]. 2013. Global intercomparability in a changing ocean: An international time-series methods workshop, November 28–30, 2012, (Bermuda Institute of Ocean Sciences, St. Georges, Bermuda). Ocean Carbon and Biogeochemistry (OCB) Program and International Ocean Carbon Coordination Project (IOCCP). doi:10.25607/OBP-12

Lovenduski, N. S., N. Gruber, S. C. Doney, and I. D. Lima. 2007. Enhanced CO_2 outgassing in the Southern Ocean from a positive phase of the Southern Annular Mode. Global Biogeochem. Cy. 21: GB2026.

Lovenduski, N. S., A. R. Fay, and G. A. McKinley. 2015. Southern Ocean CO_2 uptake: What can we learn from an ocean model? Global Biogeochem. Cy. 29: 416–426.

Lueker, T. J., A. G. Dickson, and C. D. Keeling. 2000. Ocean pCO_2 calculated from dissolved inorganic carbon, alkalinity, and equations for K_1 and K_2: Validation based on laboratory measurements of CO_2 in gas and seawater at equilibrium. Mar. Chem. 70: 105–119.

Luo, W., H. Li, S. Gao, Y. Yu, L. Lin, and Y. Zeng. 2016. Molecular diversity of microbial eukaryotes in sea water from Fildes Peninsula, King George Island, Antarctica. Polar Biol. 39: 605–616. doi: 10.1007/s00300-015-1815-8

Maksym, T., S. E. Stammerjohn, S. Ackley, and R. Massom. 2012. Antarctic Sea Ice - A Polar Opposite? Oceanography 25: 140–151.

Mann, E. L., N. Ahlgren, J. W. Moffett, and S. W. Chisolm. 2002. Copper toxicity and cyanobacteria ecology in the Sargasso Sea. Limnol. Oceanogr. 47: 976–988. doi: 10.4319/lo.2002.47.4.0976

Marshall, G. J. 2003. Trends in the Southern Annular Mode from observations and reanalyses. J. Clim. 16: 4134–4143. doi: 10.1175/1520-0442(2003)016<4134:TITSAM>2.0.CO;2

Martin, J. H., S. E. Fitzwater, and R. M. Gordon. 1990. Iron deficiency limits phytoplankton growth in Antarctic waters. Global Biogeochem. Cy. 4: 5–12. doi:10.1029/GB004i001p00005

Martinson, D. G. 2012. Antarctic circumpolar current's role in the Antarctic ice system: An overview. Palaeogeogr. Palaeoclimatol. Palaeoecol. 335:71–74.

Martinson, D. G., S. E. Stammerjohn, R. A. Iannuzzi, R. Smith, and M. Vernet. 2008. Western Antarctic Peninsula physical oceanography and spatio-temporal variability. Deep-Sea Res. Part II Top. Stud. Oceanogr. 55: 1964–1987. doi:10.1016/j.dsr2.2008.04.038

Mascioni, M., G. O. Almandoz, A. O. Cefarelli, A. Cusick, M. E. Ferrario, and M. Vernet. 2019. Phytoplankton composition and bloom formation in unexplored nearshore waters of the western Antarctic Peninsula. Polar Biol. 42: 1859–1872. doi: 10.1007/s00300-019-02564-7

Matsen, F. A., R. B. Kodner, and E. V. Armbrust. 2010. pplacer: Linear time maximum-likelihood and Bayesian phylogenetic placement of sequences onto a fixed reference tree. BMC Bioinformatics. 11: 538, doi:10.1186/1471-2105-11-538

McDougall, T.J., and P. M. Barker. 2011. Getting started with TEOS-10 and the Gibbs Seawater (GSW) Oceanographic Toolbox, 28pp., SCOR/IAPSO WG127, ISBN 978-0-646-55621-5.

McKinley, G. A., A. R. Fay, N. S. Lovenduski, and D. J. Pilcher. 2017. Natural variability and anthropogenic trends in the ocean carbon sink. Annu. Rev. Mar. Sci. 9: 125–150.

Mendes, C. R. B., V. M. Tavano, M. C. Leal, M. S. de Souza, V. Brotas, and C. A. E. Garcia. 2013. Shifts in the dominance between diatoms and cryptophytes during three late summers in the Bransfield Strait (Antarctic Peninsula). Polar Biol. 36: 537–547. doi:10.1007/s00300-012-1282-4

Meredith, M. P., and others. 2010. Changes in the freshwater composition of the upper ocean west of the Antarctic Peninsula during the first decade of the 21st century. Prog. Oceanogr. 87: 127–143. doi:10.1016/j.pocean.2010.09.019

Meredith, M. P., and others. 2017. Changing distributions of sea ice melt and meteoric water west of the Antarctic Peninsula. Deep-Sea Res. Part II Top. Stud. Oceanogr. 139: 40–57. doi:10.1016/j.dsr2.2016.04.019

Meredith, M., and others. 2019. Polar regions, p. 231–320. In: H-O Pörtner and others [eds.], IPCC special report on the ocean and cryosphere in a changing climate.

Meredith, M. P., and J. C. King. 2005. Rapid climate change in the ocean west of the Antarctic Peninsula during the second half of the 20th century. Geophys. Res. Lett. 32: L19604. doi:10.1029/2005GL024042

Mitchell, A., G. H. Brown, and R. Fuge. 2001. Minor and trace element export from a glacierized Alpine headwater catchment (Haut Glacier d'Arolla, Switzerland). Hydrol. Process. 15: 3499–3524. doi:10.1002/hyp.1041.

Moline, M. A., and B. B. Prézelin. 1996. Long-term monitoring and analyses of physical factors regulating variability in coastal Antarctic phytoplankton biomass, in situ productivity and taxonomic composition over subseasonal, seasonal and interannual time scales. Mar. Ecol. Prog. Ser. 143–160.

Moline, M., H. Claustre, T. K. Frazer, O. Schofield, and M. Vernet. 2004. Alteration of the food web along the Antarctic Peninsula in response to a regional warming trend. Glob. Chang. Biol. 10: 1973–1980. doi:10.1111/j.1365-2486.2004.00825.x

Montes-Hugo, M. A., and others. 2009. Recent changes in phytoplankton communities associated with rapid regional climate change along the Western Antarctic Peninsula. Science 323: 1470–1473. doi:10.1126/science.1164533

Munro, D. R., N. S. Lovenduski, T. Takahashi, B. B. Stephens, T. Newberger, and C. Sweeney. 2015. Recent evidence for a strengthening CO_2 sink in the Southern Ocean from carbonate system measurements in the Drake Passage (2002-2015). Geophys. Res. Lett. 42: 7623–7630.

Munro, D. R., and others. 2015. Estimates of net community production in the Southern Ocean determined from time series observations (2002–2011) of nutrients, dissolved inorganic carbon, and surface ocean pCO_2 in Drake Passage. Deep-Sea Res. Pt. II. 114: 49–63.

Nawrocki, E. P., and S. R. Eddy. 2013. Infernal 1.1: 100-fold faster RNA homology searches. Bioinformatics. 29: 2933–2935. doi:10.1093/bioinformatics/btt509

Östlund, H. G., and G. Hut. 1984. Arctic Ocean water mass balance from isotope data. J. Geophys. Res. 89: 6373–6381. doi:10.1029/JC089iC04p06373

Parsons, R. T., Y. Maita, and C. M. Lalli. 1984. A manual of chemical and biological methods for seawater analysis. Pergammon Press.

Quast, C., E. Pruesse, P. Yilmaz, J. Gerken, T. Schweer, P. Yarza, J. Peplies, and F. O. Glöckner. 2013. The SILVA ribosomal RNA gene database project: Improved data processing and web-based tools. Nucl. Acids Res. 41: D590–D596. doi:10.1093/nar/gks1219

Raiswell, R., L. G. Benning, M. Tranter, and S. Tulaczyk. 2008. Bioavailable iron in the Southern Ocean: the significance of the iceberg conveyor belt. Geochem. T. 9: 7. doi:10.1186/1467-4866-9-7

Raphael, M. N., and others. 2016. The Amundsen Sea low: variability, change, and impact on Antarctic climate. Bull. Amer. Meteor. Soc. 97: 111–121. doi:10.1175/BAMS-D-14-00018.1

Rognes, T., T. Flouri, B. Nichols, C. Quince, and F. Mahé. 2016. VSEARCH: A versatile open source tool for metagenomics. PeerJ. 4: e2584, doi:10.7717/peerj.2584

Rozema, P. D., T. Biggs, P. A. A. Sprong, A. G. J. Buma, H. J. Venables, C. Evans, M. P. Meredith, and H. Bolhuis. 2017. Summer microbial community composition governed by upper-ocean stratification and nutrient availability in northern Marguerite Bay, Antarctica. Deep Sea Res. Pt. II Top. Stud. Oceanogr. 139: 151–166. doi:10.1016/j.dsr2.2016.11.016

Saba, G. K., and others. 2014. Winter and spring controls on the summer food web of the coastal West Antarctic Peninsula. Nat. Commun. 5: 4318, doi:10.1038/ncomms5318

Sabine, C. L., and others. 2004. The oceanic sink for anthropogenic CO_2. Science 305: 367–371.

Sailley, S. F., H. W. Ducklow, H. V. Moeller, W. R. Fraser, O. M. Schofield, D. K. Steinberg, L. M. Garzio, and S. C. Doney. 2013. Carbon fluxes and pelagic ecosystem dynamics near two western Antarctic Peninsula Adélie penguin colonies: an inverse model approach. Mar. Ecol. Prog. Ser. 492: 253–272. doi: 10.3354/meps10534

Sarmiento, J. L., and N. Gruber. 2006. Ocean Biogeochemical Dynamics 118–119 (Princeton Univ. Press, Princeton)

Schofield, O., H. W. Ducklow, D. G. Martinson, M. P. Meredith, M. A. Moline, and W. R. Fraser. 2010. How do polar marine ecosystems respond to rapid climate change? Science 328: 1520–1523. doi:10.1126/science.1185779

Schofield, O., and others. 2017. Decadal variability in coastal phytoplankton community composition in a changing West Antarctic Peninsula. Deep-Sea Res. Part I Oceanogr. Res. Pap. 124: 42–54. doi:10.1016/j.dsr.2017.04.014

Schofield, O., and others. 2018. Changes in the upper ocean mixed layer and phytoplankton productivity along the West Antarctic Peninsula. Philos. Trans. R. Soc. A Math. Phys. Eng. Sci. 376: 20170173, doi:10.1098/rsta.2017.0173

Sherrell, R. M., A. L. Annett, J. N. Fitzsimmons, V. J. Roccanova, and M. P. Meredith. 2018. A ‘shallow bathtub ring’ of local sedimentary iron input maintains the Palmer Deep biological hotspot on the West Antarctic Peninsula shelf. Philos. Trans. R. Soc. A Math. Phys. Eng. Sci. 376: 20170171. doi:10.1098/rsta.2017.0171

Smith, R., D. G. Martinson, S. E. Stammerjohn, R. A. Iannuzzi, and K. Ireson. 2008. Bellingshausen and western Antarctic Peninsula region: Pigment biomass and sea-ice spatial/temporal distributions and interannual variabilty. Deep-Sea Res. Part II Top. Stud. Oceanogr. 55: 1949–1963. doi:10.1016/j.dsr2.2008.04.027

Stamatakis, A. 2014. RAxML version 8: A tool for phylogenetic analysis and post-analysis of large phylogenies. Bioinformatics. 30: 1312–1313. doi:10.1093/bioinformatics/btu033

Stammerjohn, S. E., D. G. Martinson, R. C. Smith, and R. A. Iannuzzi. 2008a. Sea ice in the western Antarctic Peninsula region: Spatio-temporal variability from ecological and climate change perspectives. Deep-Sea Res. Part II Top. Stud. Oceanogr. 55: 2041–2058. doi:10.1016/j.dsr2.2008.04.026

Stammerjohn, S. E., D. G. Martinson, R. C. Smith, X. Yuan, and D. Rind. 2008b. Trends in Antarctic annual sea ice retreat and advance and their relation to El Niño–Southern Oscillation and Southern Annular Mode variability. J. Geophys. Res.-Oceans 113: C03S90.

Statham, P. J., M. Skidmore, and M. Tranter. 2008. Inputs of glacially derived dissolved and colloidal iron to the coastal ocean and implications for primary productivity. Global Biogeochem. Cy. 22: GB3013. doi:10.1029/2007GB003106.

Steinberg, D. K., and others 2015. Long-term (1993–2013) changes in macrozooplankton off the Western Antarctic Peninsula. Deep-Sea Res. Part I Oceanogr. Res. Papers. 101: 54–70. doi:10.1016/j.dsr.2015.02.009

Stoeck, T., D. Bass, M. Nebel, R. Christen, M. D. M. Jones, H. W. Breiner, and T. A. Richards. 2010. Multiple marker parallel tag environmental DNA sequencing reveals a highly complex eukaryotic community in marine anoxic water. Mol. Ecol. 19: 21–31. doi:10.1111/j.1365-294X.2009.04480.x

Stoecker, D. K., P. J. Hansen, D. A. Caron, and A. Mitra. 2017. Mixotrophy in the marine plankton. Annu. Rev. Mar. Sci. 9: 311–335.

Sweeney, C. 2003. The annual cycle of surface water CO_2 and O_2 in the Ross Sea: A model for gas exchange on the continental shelves of Antarctica. Biogeochemistry of the Ross Sea, Antarct. Res. Ser. 78: 295–312.

Takahashi, T., and others. 2002. Global sea-air CO_2 flux based on climatological surface ocean pCO_2, and seasonal biological and temperature effects. Deep-Sea Res. Pt. II 49: 1601–1622.

Takahashi, T., and others. 2012. The changing carbon cycle in the Southern Ocean. Oceanography 25: 26–37.

Takahashi, T., and others. 2014. Climatological distributions of pH, pCO_2, total CO_2, alkalinity, and $CaCO_3$ saturation in the global surface ocean, and temporal changes at selected locations. Mar. Chem. 164: 95–125.

Takahashi, T., J. Olafsson, J. G. Goddard, D. W. Chipman, and S. C Sutherland. 1993. Seasonal variation of CO_2 and nutrients in the high-latitude surface oceans: A comparative study. Global Biogeochem. Cy. 7: 843–878.

Thompson, D. W., and S. Solomon. 2002. Interpretation of recent Southern Hemisphere climate change. Science 296: 895–899.

Thompson, D. W., S. Solomon, P. J. Kushner, M. H. England, K. M. Grise, and D. J. Karoly. 2011. Signatures of the Antarctic ozone hole in Southern Hemisphere surface climate change. Nat. Geosci. 4: 741–749.

Tortell, P. D., and others. 2014. Metabolic balance of coastal Antarctic waters revealed by autonomous pCO_2 and $\Delta O_2/Ar$ measurements. Geophys. Res. Lett. 41: 6803–6810.

Turner, J., and others. 2014. Antarctic climate change and the environment: An update. Polar Rec. 50: 237–259. doi:10.1017/S0032247413000296

Turner J., and others. 2016. Absence of 21st century warming on Antarctic Peninsula consistent with natural variability. 535: 411–415. doi:10.1038/nature18645

van Heuven, S., D. Pierrot, J. W. B. Rae, E. Lewis, and D. W. R Wallace. 2011. MATLAB Program Developed for CO_2 System Calculations. ORNL/CDIAC-105b. Oak Ridge National Laboratory, U.S. Department of Energy, Oak Ridge, Tennessee. doi: 10.3334/CDIAC/otg.CO2SYS_MATLAB_v1.1

Vaughan, D. G. 2006. Recent trends in melting conditions on the Antarctic Peninsula and their implications for ice-sheet mass balance and sea level. 38: 2041–2058. Arct. Antarct. Alp. Res. doi:10.1657/1523-0430(2006)038[0147:RTIMCO]2.0.CO;2

Vaughan, D. G., and others. 2003. Recent rapid regional climate warming on the Antarctic Peninsula. Climatic Change 60: 243–274. doi:10.1023/A:1026021217991

Vernet, M., D. Martinson, R. Iannuzzi, S. Stammerjohn, W. Kozlowski, K. Sines, R. Smith, and I. Garibotti. 2008. Primary production within the sea-ice zone west of the Antarctic Peninsula: I–Sea ice, summer mixed layer, and irradiance. Deep-Sea Res. Part II Top. Stud. Oceanogr. 55: 2068–2085. doi:10.1016/j.dsr2.2008.05.021

Waters, K. J., and R. C. Smith. 1992. Palmer LTER: A sampling grid for the Palmer LTER program. Antarct. J. US. 27: 236–239.

Wehrens, R., and J. Kruisselbrink. 2018. Flexible self-organizing maps in kohonen 3.0. J. Stat. Soft. 87: 1–18. doi:10.18637/jss.v087.i07

Williams, N. L., R. A. Feely, C. L. Sabine, A. G. Dickson, J. H. Swift, L. D. Talley, and J. L Russell. 2015. Quantifying anthropogenic carbon inventory changes in the Pacific sector of the Southern Ocean. Mar. Chem. 174: 147–160.

Wimpenny, J., R. H. James, K. W. Burton, A. Gannoun, F. Mokadem, and S. R. Gíslason. 2010. Glacial effects on weathering processes: new insights from the elemental and lithium isotopic composition of West Greenland rivers. Earth Planet. Sc. Lett. 290: 427–437. doi:10.1016/j.epsl.2009.12.042

Yager, P. L., D. W. Wallace, K. M. Johnson, W. O Smith Jr, P. J. Minnett, and J. W. Deming. 1995. The Northeast Water Polynya as an atmospheric CO_2 sink: A seasonal rectification hypothesis. J. Geophys. Res-Oceans 100: 4389–4398.

Yuan, X. 2004. ENSO-related impacts on Antarctic sea ice: a synthesis of phenomenon and mechanisms. Antarct. Sci. 16: 415–425.

7 Appendix A: Glacial meltwater microcosm experiment

7.1 Motivation

One hypothesis for the association between WAP cryptophytes and glacial meltwater is that there is a meltwater constituent (or lack thereof) that provides cryptophytes with an advantage, and/or diatoms with a disadvantage (Schofield et al. 2017). The focus of this appendix is to describe a microcosm experiment that was conducted at Palmer Station during the 2016-17 austral summer, where glacial meltwater was combined with coastal seawater to determine the impacts of glacial meltwater on phytoplankton community composition.

7.2 Completed methods

Two runs of the microcosm experiment (Experiment 1 and 2, respectively) were conducted at Palmer Station during the 2016-17 austral summer. The general experimental design consisted of three treatments (Figure 7.1), where whole seawater (WSW) was combined into microcosms with either 1) filtered seawater (FSW), 2) Milli-Q ultrapure water (Milli-Q), or 3) filtered glacial meltwater (FMW). The FSW and Milli-Q treatments were used for dilution and salinity controls, respectively. For all three treatments, the amount of treatment water added to the WSW was such that the final salinity of the Milli-Q and FMW treatment microcosms was 32.0 (assuming a Milli-Q and FMW salinity of 0; the salinity of the FSW treatment microcosms was not altered).

This salinity represents the lower boundary observed historically at the Palmer LTER coastal sampling sites at Palmer Station.

Glacial meltwater was collected in plastic collapsible carboys. Coastal seawater was collected by lowering 20 L polycarbonate carboys by hand from a small vessel into the surface ocean and allowing them to fill. Upon returning to the lab, the meltwater was placed in a darkened and chilled (+2°C) environmental room, and was filtered through a Pall AcroPak 200 (0.8/0.2 μm) Supor membrane capsule filter with Masterflex C-Flex ULTRA tubing into separate collapsible carboys. The FMW was then stored in the dark chilled until the beginning of the experiment. The seawater was also placed in the darkened and chilled environmental room. A portion of the seawater was filtered through a Pall AcroPak 200 (0.8/0.2 μm) Supor membrane capsule filter and Masterflex C-Flex ULTRA tubing into a collapsible carboy. The remaining seawater was screened through 350 μm nylon mesh to remove large zooplankton. The WSW and FSW were then stored in the dark chilled until the beginning of the experiment. In the morning of the first day of the experiments, the microcosms were constructed with the WSW, FSW, Milli-Q, and FMW. The microcosms were incubated in a large aquarium at Palmer Station (Figure 7.2), which was temperature-controlled with ambient coastal seawater continuously circulated through the aquarium. The microcosms were sampled immediately after construction, and then throughout the experiments.

Experiment 1 was conducted in mid-January, 2017. The experimental design consisted of four microcosms for each of the three treatments (12 total): one that was destructively sampled immediately after construction (T_0), and three replicates that were incubated and sampled with repetition after 1, 3, 4, 7, and 10 days (T_1, T_3, T_4, T_7, and T_{10},

respectively). On January 11 glacial meltwater was collected from Stream 2 (Figure 4.1) subsequent to the stream sampling (see Chapter 4). On January 13 seawater was collected at Station B, where the surface salinity was measured to be 33.0. On January 14 the experiment was started. The microcosms were constructed in 20 L polycarbonate carboys. Each microcosm consisted of 19.4 L of WSW and 0.6 L of treatment water (FSW, Milli-Q, or FMW). On each sampling day, in each of the microcosms, samples for macronutrients and duplicate samples for total chl-*a* were collected. On T_0, T_7, and T_{10}, duplicate samples for size-fractionated chl-*a* were collected.

Experiment 2 was conducted in mid-February, 2017. The experimental design consisted of nine microcosms for each of the three treatments (27 total): three replicates that were destructively sampled on T_0, T_4, T_7. On February 16 glacial meltwater was collected from Stream 1 (Figure 4.1) subsequent to the stream sampling (see Chapter 4), and seawater was collected at Station E, where the surface salinity was measured to be 33.8. On February 17 the experiment was started. The T_0, and T_4 and T_7 microcosms were constructed in 4 and 2 L polycarbonate bottles, respectively. The T_0 (T_4 and T_7) microcosms consisted of 3.9 L (2 L) of WSW and 218 mL (112 mL) of treatment water (FSW, Milli-Q, or FMW). On each sampling day, in each of the microcosms, a single sample for macronutrients and duplicate samples for total and size-fractionated chl-*a* were collected.

Macronutrient samples were collected by filtering seawater through a pre-combusted Whatman 25 mm, GF/F filter into a 15 mL plastic centrifuge tube. The centrifuge tubes were stored frozen at -80°C (later -20°C). Total and size-fractionated chl-*a* samples were collected by filtering seawater directly, or first through 47 mm, 20

μm Millipore nylon mesh filters, onto Whatman 25 mm, GF/F filters, which were placed in glass scintillation vials and frozen at -80°C. While on station, the chl-*a* filters were extracted in 90% acetone for > 24 hr at -20°C, and the filter extracts were measured with a Turner 10AU fluorometer. In spring 2017, the macronutrient samples were analyzed at Lamont-Doherty Earth Observatory (Columbia University, NY, USA). Samples were run on a AA3 HR AutoAnalyzer (SEAL Analytical) for phosphate, nitrate+nitrite, and silicate.

7.3 Preliminary results

In both Experiment 1 and 2, all three treatments experienced a phytoplankton bloom during the course of the experiment, as evidenced by a concurrent increase and decrease in total chl-*a* and macronutrients, respectively (Figure 7.3a,c and 7.4). Additionally, both experiments appeared to be nitrate-limited in all three treatments by T_7. Furthermore, in both experiments, in all three treatments, smaller cells (< 20 μm) initially dominated the phytoplankton community, and then decreased in proportion (Figure 7.3b,d). However, in Experiment 1, although all three treatments initially had the same proportion of smaller cells (~94%), by T_7 the FMW had a higher proportion (~72%) than that of the FSW and Milli-Q treatments, which were relatively the same (~53%). This pattern was also observed on T_{10} (FMW: ~76%; FSW, Milli-Q: ~55%). Indeed, on T_{10} there was a significant difference among treatments in size-fractionated chl-*a* < 20 μm (one-way ANOVA: $F_{2,8} = 10.8$, $p = 0.01$) and size-fractionated chl-*a* > 20 μm (one-way ANOVA: $F_{2,8} = 8.2$, $p = 0.02$). Post-hoc analysis with Tukey's HSD test indicated no difference in size-fractionated chl-*a* < 20 μm or > 20 μm among the Milli-Q and FSW

treatments. However, both of these treatments differed significantly from FMW for size-fractionated chl-*a* < 20 μm (FMW greater than FSW and Milli-Q) and > 20 μm (FMW less than FSW and Milli-Q) ($\alpha = 0.05$). By the end of Experiment 1, smaller cells were still the dominant component of the phytoplankton community in all three treatments (Figure 7.3b). In Experiment 2, the FMW treatment began with a pattern of a higher proportion (~81%) of smaller cells than that of the FSW and Milli-Q treatments, which were relatively the same (~66%). However, on T_0 there was no difference among treatments in size-fractionated chl-*a* < 20 μm (one-way ANOVA: $F_{2,8} = 0.4$, $p = 0.69$), or size-fractionated chl-*a* > 20 μm (one-way ANOVA: $F_{2,8} = 2.2$, p=0.19). There was a progression throughout the experiment where the proportion of smaller cells in all three treatments decreased, and converged to a common value (~6%). By the end of Experiment 2, smaller cells were a minor component of the phytoplankton community in all three treatments (Figure 7.3d).

7.4 Concluding remarks

In Experiment 1 there was higher proportion of smaller phytoplankton cells in the FMW treatment relative to the FSW and Milli-Q treatments, which were relatively the same (Figure 7.3b). These results are interesting, as they mirror the association between smaller cells (e.g. cryptophytes) and meltwater observed in the field (Moline et al. 2004, Schofield et al. 2017). The fact that a higher proportion of smaller cells was not observed in the Milli-Q treatment suggests that a dissolved meltwater constituent was the driver, as opposed to a change in salinity. This treatment effect was not observed in Experiment 2. However, a pattern in Experiment 2 of a relatively higher proportion of smaller cells in

the FMW treatment than in the FSW and Milli-Q treatments at T_0 suggests there was a small, immediate treatment effect (multiple hours passed between constructing and sampling the T_0 microcosms).

One explanation for the different responses observed in Experiment 1 and 2 could be that the starting WSW phytoplankton community composition differed between experiment runs. For example, Experiment 1 was run in mid-January, 2017 with WSW collected from Station B, and Experiment 2 was run in mid-February, 2017 with WSW collected from Station E. Another explanation for the different responses between Experiment 1 and 2 could be that the starting WSW, FSW, and FMW trace metal concentrations differed between experiment runs. For example, Experiment 1 was run with FMW collected from Stream 2, and Experiment 2 was run with FMW collected from Stream 1 (Figure 4.1). Additionally, the relative amount of FMW added to WSW was greater in Experiment 2 than Experiment 1, as the Experiment 2 WSW had a higher salinity (33.8 vs. 33.0). Future work should focus on repeating these experiments across a variety of seawater phytoplankton communities, glacial meltwater sources, and salinities.

7.5 Figures

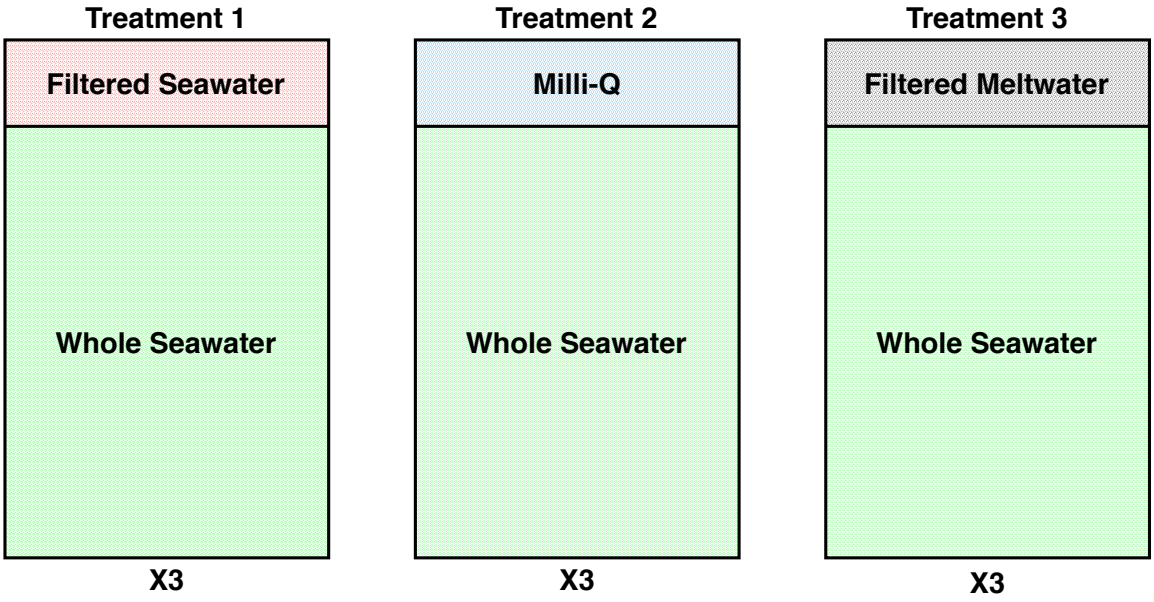

Figure 7.1. General experimental design of the glacial meltwater microcosm experiment showing the three different treatments added to whole seawater in triplicate: 1) filtered seawater, 2) Milli-Q ultrapure water, and 3) filtered glacial meltwater.

Figure 7.2. Image of the glacial meltwater microcosm experiment incubation aquarium located on the Palmer Station deck. The Marr Glacier can be seen in the background.

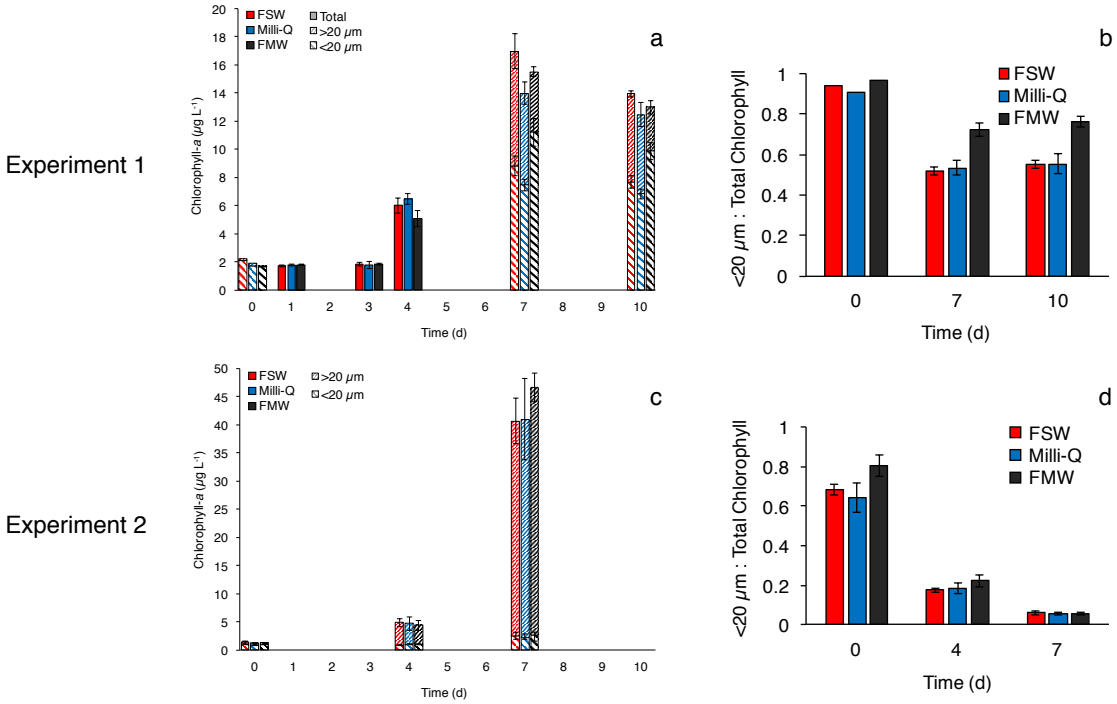

Figure 7.3. Glacial meltwater microcosm experiment chl-*a* concentrations: **a,c** total and size fractionated chl-*a* during Experiment 1 and 2, respectively, and **b,d** ratio of < 20 µm to total chl-*a* during Experiment 1 and 2, respectively.

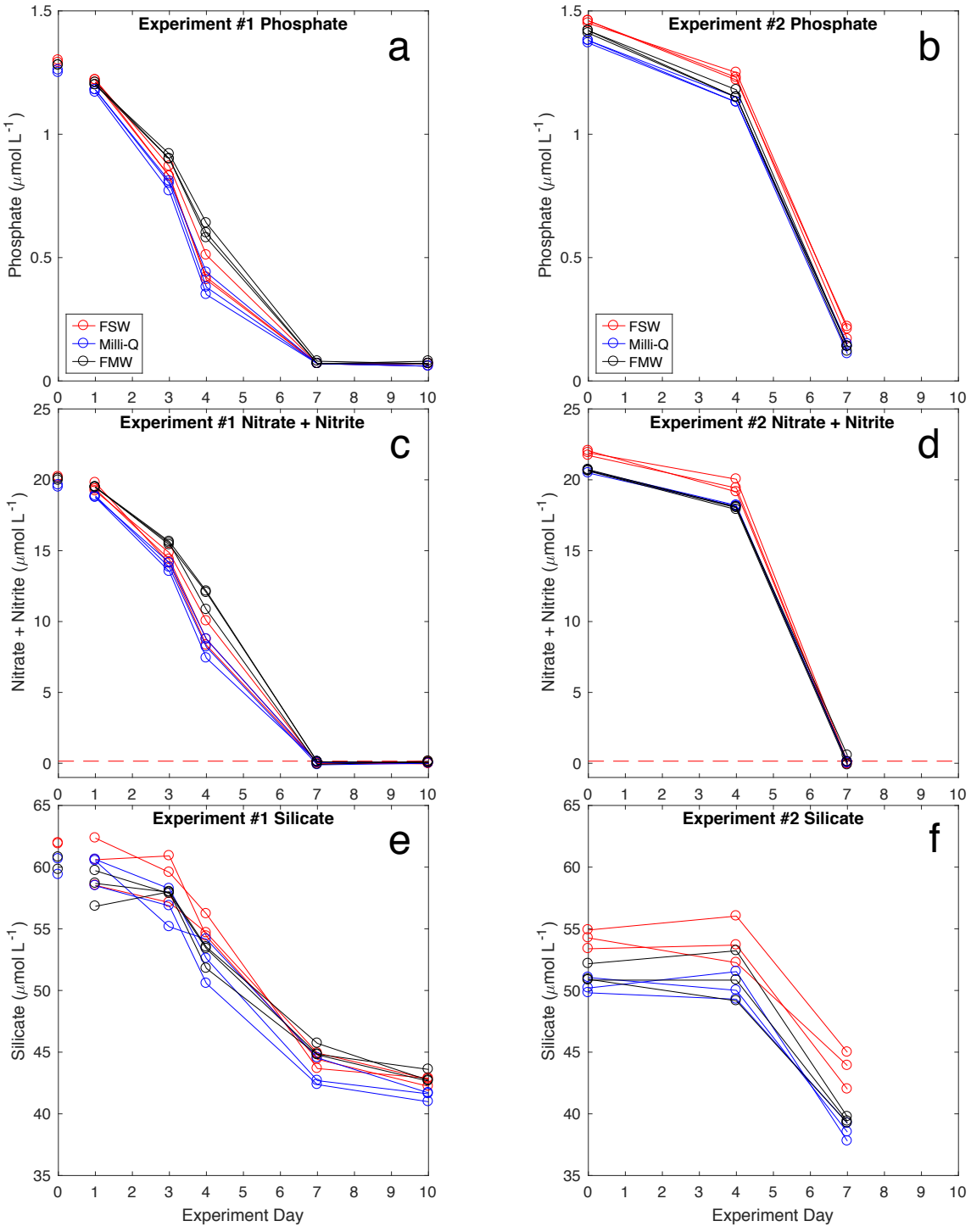

Figure 7.4. Glacial meltwater microcosm experiment macronutrient concentrations: **a,c,e** Experiment 1, and **b,d,f** Experiment 2. The horizontal red line indicates an estimate of the limit of detection.